ZEOLITE Y COMPOSITE WITH BAMBOO WOOD FOR NICKEL ION AND CARBON DIOXIDE ADSORPTION AND WITH COPPER FOR CATALYTIC ETHANOL STEAM REFORMING

PIMRAPUS TAWACHKULTANADILOK

A Thesis Submitted in Partial Fulfillment of the Requirements for the
Degree of Doctor of Philosophy in Chemistry
Suranaree University of Technology
Academic Year 2022

ซีโอไลต์วายคอมโพสิทกับไม้ไผ่สำหรับการดูดซับไอออนนิกเกิลและคาร์บอนไดออกไซด์ และกับทองแดงสำหรับการเร่งปฏิกิริยาเอทานอลสตีมรีฟอร์มมิ่ง

นางสาวพิมพ์รภัส ธวัชกุลธนดิลก

ZEOLITE Y COMPOSITE WITH BAMBOO WOOD FOR NICKEL ION AND CARBON DIOXIDE ADSORPTION AND WITH COPPER FOR CATALYTIC ETHANOL STEAM REFORMING

Suranaree University of Technology has approved this thesis submitted in partial fulfillment of the requirements for the Degree of Doctor of Philosophy.

Thesis Examining Committee

_____
(Asst. Prof. Dr. Sirinuch Loiha)
Chairperson
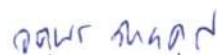
_____
(Prof. Dr. Jatuporn Wittayakun)
Member (Thesis advisor)

_____
(Assoc. Prof. Dr. Sanchai Prayoonpokarach)
Member (Thesis co-advisor)

_____
(Asst. Prof. Dr. Suwit Suthirakun)
Member

_____
(Dr. Yingyot Poo-arporn)
Member

_____
(Assoc. Prof. Dr. Chatchai Jothityangkoon)
Vice Rector for Academic Affairs
and Quality Assurance

_____
(Prof. Dr. Santi Maensiri)
Dean of Institute of Science

พิมพ์รภัส ธวัชกุลธนดิลก : ซีโอไลต์วายคอมโพสิทกับไม้ไผ่สำหรับการดูดซับไอออนนิกเกิล
และคาร์บอนไดออกไซด์ และกับทองแดงสำหรับการเร่งปฏิกิริยาเอทานอลสตีมรีฟอร์มมิ่ง
(ZEOLITE Y COMPOSITE WITH BAMBOO WOOD FOR NICKEL ION AND CARBON
DIOXIDE ADSORPTION AND WITH COPPER FOR CATALYTIC ETHANOL STEAM
REFORMING) อาจารย์ที่ปรึกษา : ศาสตราจารย์ ดร.จตุพร วิทยาคุณ, 97 หน้า

คำสำคัญ: ซีโอไลต์/ ซีโอไลต์วาย/ คอมโพสิท/ วัสดุดูดซับ/ซีโอไลต์ขนาดนาโนเมตร/ ซีโอไลต์ขนาด
ไมโครเมตร/ การดูดซับนิกเกิลไอออน/ การดูดซับแก๊สคาร์บอนไดออกไซด์/ ตัวเร่งปฏิกิริยาทองแดง/
ปฏิกิริยาเอทานอลสตีมรีฟอร์มมิ่ง/ การแปลงผันเอทานอล/ การผลิตไฮโดรเจน

วิทยานิพนธ์นี้มุ่งเน้นที่การเพิ่มประสิทธิภาพของซีโอไลต์วาย เพื่อเป็นวัสดุดูดซับโดยการผสม
ซีโอไลต์กับไม้ไผ่ และนำไปเป็นวัสดุรองรับตัวเร่งปฏิกิริยา โดยใช้ซีโอไลต์ในรูปต่าง ๆ เพื่อศึกษาการ
กระจายตัวของทองแดง (Cu)

งานนี้เริ่มต้นโดยกระจายซีโอไลต์วายบนไม้ไผ่เพื่อสร้างคอมโพสิทซีโอไลต์-คาร์บอน เพื่อให้ได้
ปริมาณซีโอไลต์บนเนื้อไม้จำนวนมาก จะมีการรีฟลักซ์ไม้ด้วยสารละลายกรดไฮโดรคลอริกก่อนที่จะ
ผสมกับเจลที่ใช้เตรียมซีโอไลต์วาย การสังเคราะห์คอมโพสิทใช้วิธีไฮโดรเทอร์มอล การปรับสภาพด้วย
กรดดังกล่าวจะเพิ่มปริมาณซีโอไลต์บนเนื้อไม้ไผ่และเพิ่มความบริสุทธิ์ของซีโอไลต์ในคอมโพสิท วัสดุ
คอมโพสิทซีโอไลต์-คาร์บอนที่ผ่านกระบวนการทางเคมี จะแสดงความสามารถในการดูดซับไอออน
นิกเกิล (Ni (II)) สูงสุด และมีข้อดี ได้แก่ การแยกวัสดุดูดซับและสารละลายออกจากกันได้ง่าย อย่างไร
ก็ตาม เนื่องจากขนาดอนุภาคไมโครเมตรของซีโอไลต์และพื้นที่ไม้ที่ยังเหลือมาก นำไปสู่การปรับปรุง
เปอร์เซ็นต์และขนาดอนุภาคของซีโอไลต์ เพื่อพัฒนาคอมโพสิทในงานต่อมา ซึ่งในส่วนนี้ได้ทำการ
ปรับเปลี่ยนปริมาณน้ำในขั้นตอนการเตรียมเจลคอมโพสิท ส่งผลให้ขนาดอนุภาคซีโอไลต์ในคอมโพสิท
ลดลงจาก 3-4 ไมโครเมตร เป็น 150-200 นาโนเมตร ซีโอไลต์วายคอมโพสิทขนาดนาโนนี้แสดงการ
กระจายตัวที่ดีขึ้นและความสามารถในการดูดซับแก๊สคาร์บอนไดออกไซด์ (CO_2) สูงเมื่อเทียบกับ
ซีโอไลต์วายแบบไม่มีไม้

นอกจากนี้ ยังมีการพัฒนาซีโอไลต์วายเป็นวัสดุรองรับสำหรับตัวเร่งปฏิกิริยาทองแดง
เพื่อตรวจสอบผลของความเป็นกรด-เบสของวัสดุรองรับต่อการกระจายตัวของโลหะและขั้นตอนการ
แปลงผันเอทานอล ด้วยการใช้ซีโอไลต์วายรูปแบบต่างๆ ได้แก่ โซเดียม (NaY), แอมโมเนียม (NH$_4$Y)
และโปรตอน (HY) ในงานนี้มีการเตรียมตัวเร่งปฏิกิริยาที่มีซีโอไลต์เป็นวัสดุรองรับตัวเร่งปฏิกิริยา
ทองแดงด้วยวิธีการเอิบชุ่มในการเตรียมตัวอย่างต่าง ๆ (CuO/NaY, CuO/NH$_4$Y, CuO/HY) ในงานนี้
มีการใช้ระบบ *operando* ซึ่งเป็นการดำเนินการร่วมกันระหว่าง ระบบทางสเปกโทรสโกปี TR-XAS
กับเทคนิคแก๊สโครมาโตกราฟี (GC) และแมสสเปกโทรเมทรี (MS) เพื่อให้ได้ข้อมูลเชิงลึกเกี่ยวกับการ
เปลี่ยนแปลงโครงสร้างของทองแดงในระหว่างการเร่งปฏิกิริยาเอทานอลสตีมรีฟอร์มมิ่ง (Ethanol
steam reforming, ESR) ผลลัพธ์บ่งชี้ว่า การรีดิวส์ทองแดงในรูปออกไซด์ไปเป็นโลหะทองแดงบน
ซีโอไลต์ NaY ทำได้ง่ายกว่าบนซีโอไลต์ NH$_4$Y และ HY เนื่องจากความแตกต่างของชนิดทองแดง
ออกไซด์และไอออนทองแดง (Cu (II)) การทดสอบการเร่งปฏิกิริยา ESR แสดงให้เห็นว่าตัวเร่ง

ปฏิกิริยา CuO/NaY แสดงเส้นทางสำหรับการผลิตไฮโดรเจนผ่าน ESR และเอทานอลดีไฮโดรจีเนชัน ในขณะที่ตัวเร่งปฏิกิริยา CuO/NH$_4$Y สนับสนุนการผลิตแก๊ส H$_2$ ผ่าน ESR และเอทิลีนสตีมรีฟอร์มมิง (Ethylene steam reforming) ในกรณีของตัวเร่งปฏิกิริยา CuO/HY นั้น แก๊ส H$_2$ เกิดจากเอทานอล ดีไฮโดรจีเนชันและเอทิลีนสตีมรีฟอร์มมิง นอกจากนี้ ชนิดของทองแดงในการทดสอบ ESR ยังแตกต่าง กันไปขึ้นอยู่กับรูปแบบของซีโอไลต์ที่ใช้เป็นวัสดุรองรับ ซึ่งอาจมีส่วนทำให้เกิดเส้นทางที่จำเพาะ สำหรับการแปลงผันเอทานอลที่แตกต่างกัน ตัวเร่งปฏิกิริยา CuO/NaY แสดงความจำเพาะสูงสุด สำหรับการผลิต H$_2$ จากปฏิกิริยา ESR โดยสรุป ซีโอไลต์ NaY เหมาะกับการใช้เป็นวัสดุรองรับสำหรับ ตัวเร่งปฏิกิริยาทองแดงในการเร่งปฏิกิริยา ESR

   การศึกษานี้แสดงให้เห็นถึงศักยภาพของวัสดุคอมโพสิตที่ผสมระหว่างซีโอไลต์วายและไม้ไผ่ ในการเป็นตัวดูดซับที่มีประสิทธิภาพ และเน้นย้ำถึงอิทธิพลของซีโอไลต์ในรูปต่าง ๆ ที่มีต่อคุณสมบัติ ของกรด-เบสและพฤติกรรมการเร่งปฏิกิริยาของตัวเร่งปฏิกิริยาทองแดงที่มีวัสดุรองรับเป็นซีโอไลต์ใน การศึกษาปฏิกิริยาเอทานอลสตีมรีฟอร์มมิง

สาขาวิชาเคมี   ลายมือชื่อนักศึกษา_____

ปีการศึกษา 2565   ลายมือชื่ออาจารย์ที่ปรึกษา_____

                     ลายมือชื่ออาจารย์ที่ปรึกษาร่วม_____

PIMRAPUS TAWACHKULTANADILOK : ZEOLITE Y COMPOSITE WITH BAMBOO WOOD FOR NICKEL ION AND CARBON DIOXIDE ADSORPTION AND WITH COPPER FOR CATALYTIC ETHANOL STEAM REFORMING.THESIS ADVISOR : PROF. JATUPORN WITTAYAKUN, Ph.D. 97 PP.

Keyword: Zeolite/ Zeolite Y/ Composite/ Adsorbent/ Nanosized zeolite/ Micron sized zeolite/ Ni ion adsorption/ CO_2 adsorption/ Cu catalyst/ Ethanol steam reforming/ Ethanol conversion/Hydrogen production

This thesis concentrates on improving zeolite Y's adsorption abilities by using a composite with bamboo wood and a zeolite-supporting catalyst in various forms for dispersing Cu.

In the initial study, zeolite Y is dispersed on bamboo wood to create a zeolite-carbon composite. To achieve a high zeolite loading on the bamboo wood, the wood undergoes reflux with an HCl solution before mixing with the zeolite Y gel. The composite is synthesized using the hydrothermal method. This acid pretreatment increases the loading of zeolite on the bamboo wood and enhances the purity of zeolite in the composite. The treated wood-zeolite composite exhibits the highest adsorption capacity for Ni (II) ions, and it offers the advantage, including easy separation between the adsorbent and adsorbate. However, due to the micrometer particle size of zeolite and more space of wood, percent and particle size of zeolite should be improved. To further develop the composite in a further work, water in the gels of the composite preparation is adjusted, resulting in a reduction of the zeolite particle size in the composite from 3-4 μm to 150-200 nm. This nano-sized zeolite Y composite exhibits improved dispersion and high CO_2 adsorption capacity compared to pure zeolite NaY.

Furthermore, zeolite Y is explored as a supporting material for Cu catalysts to investigate the effect of acid-base properties of the support on metal dispersion and the pathway of ethanol conversion. Various forms of zeolite Y, including Na^+ (NaY), NH_4^+ (NH_4Y), and H^+ (HY), are utilized to prepare Cu-based catalysts using the incipient wetness impregnation method (CuO/NaY, CuO/NH_4Y, CuO/HY). An *operando* time-resolved X-ray absorption spectroscopy (TR-XAS) setup in combination with gas chromatography (GC) and mass spectrometry (MS) techniques was employed to gain insights of the structural changes of copper during pretreatment and the ethanol steam reforming (ESR) process. The results indicate that Cu on zeolite NaY can be reduced to Cu metal more than Cu on zeolite NH_4Y and HY due to differences in copper oxide

species and Cu (II) ion. The catalytic testing of ESR demonstrates that CuO/NaY catalyst exhibits a selective pathway for producing hydrogen via ESR and ethanol dehydrogenation, while CuO/NH$_4$Y catalysts favor the production of H$_2$ through ESR and ethylene steam reforming. In the case of CuO/HY catalyst, H$_2$ is generated through ethanol dehydrogenation and ethylene steam reforming. Additionally, the form of copper species in ESR testing depends on the form of zeolite support. The form could contribute to different selective pathways for ethanol conversion. The Cu/NaY catalyst gives the highest selectivity for H$_2$ in the ESR reaction. Thus, zeolite NaY is recommended as a supporting material for copper catalysts in the catalytic activity of the ESR reaction.

This thesis demonstrates the potential of composite materials involving zeolite Y and bamboo wood as efficient adsorbents and highlights the influence of different forms of zeolite on the acid-base properties and catalytic behavior of Cu-supported catalysts in ethanol steam reforming reaction.
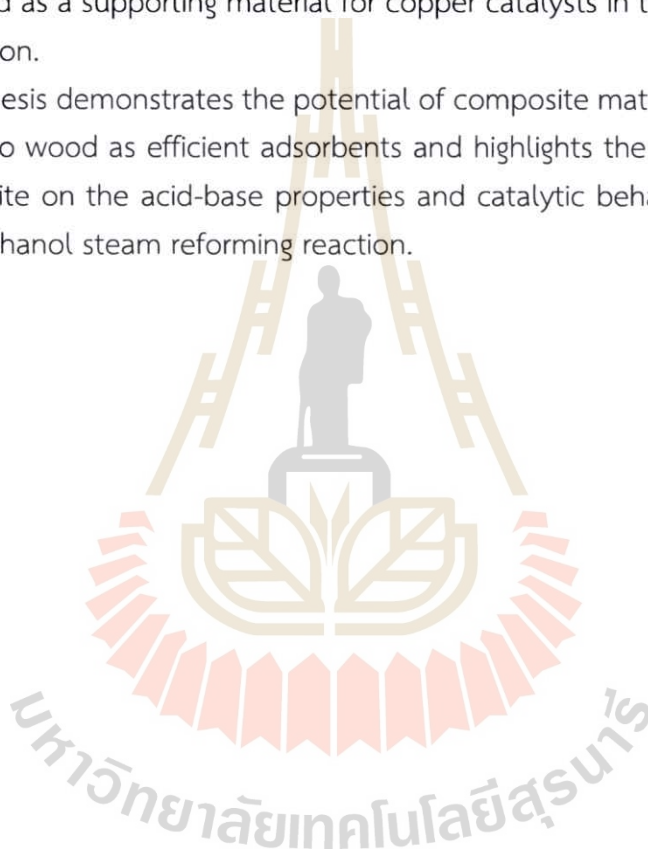
School of Chemistry

Academic Year 2022

Student's Signature_____

Advisor's Signature_____

Co-advisor's Signature_____

ACKNOWLEDGEMENTS

I would like to express my deep gratitude and appreciation to all those who contributed to and supported me during the completion of my academic subjects and thesis journey.

First and foremost, I extend my heartfelt thanks to my advisors, Prof. Dr. Jatuporn Wittayakun and Assoc. Prof. Dr. Sanchai Prayoonpokarach, for their invaluable guidance, expertise, patience, motivation, and unwavering support. Their dedication and commitment have played a pivotal role in shaping the direction and quality of my research. I also extend my utmost gratitude to the members of my thesis committee for their expertise, insights, and constructive feedback. Their contributions have been invaluable in shaping the direction and quality of my research.

I would like to express my gratitude to all the lecturers at School of Chemistry for their positive attitude and invaluable advice. I am also thankful to the staff at Center for Scientific and Technological Equipment for their assistance and suggestions regarding the use of instruments.

I am deeply indebted to Science Achievement Scholarship of Thailand (SAST) for providing the financial support that made my degree possible. Additionally, I would like to thank Suranaree University of Technology for their co-financial support for my research overseas.

Furthermore, I sincerely thank my advisor from my bachelor's school, Asst. Prof. Sirinuch Loiha, for her instrumental role, encouragement, and immense knowledge throughout my graduate course and research. I also express my gratitude to Dr. Yingyot Poo-arporn for the suggestions, devices, and access to X-ray techniques and MS instruments.

I extend my thanks to Assoc. Prof. Dr. Karin Föttinger from Institute of Materials Chemistry, Vienna University of Technology (TU Wien), Vienna, Austria, for providing me with research overseas experience and guiding me through my journey in European countries.

I am grateful to all my colleagues in JW and SP groups for their unwavering support in my research activities. I also acknowledge the support from School of Chemistry at Suranaree University of Technology, Technical Catalysis Laboratory at

Pimrapus Tawachkultanadilok

CONTENTS

CONTENTS (Continued)

CONTENTS (Continued)

LIST OF TABLES

LIST OF FIGURES

LIST OF FIGURES (Continued)

LIST OF SCHEMES

CHAPTER I

INTRODUCTION

1.1   Introduction

This thesis deals with the modification of zeolite Y for applications in adsorption and catalysis. This thesis is divided into four parts. Chapter II includes a brief literature review of the overall thesis, providing a comprehensive summary of relevant studies related to zeolite Y, the preparation of zeolite-carbon composites, and ethanol steam reforming using metal-based catalysts. Chapter III focuses on the crystallization of zeolite NaY on untreated and acid-treated bamboo wood. The wood-zeolite composite was utilized for Ni (II) ion adsorption. Chapter IV involves the preparation of nano-sized and micron-sized particles of zeolite Y on activated carbon from bamboo wood for CO_2 adsorption. Chapter V is about the preparation of copper-based catalysts on different forms of zeolite Y. The catalysts were tested in the conversion of ethanol to produce H_2 gas.

Zeolites have gained significant recognition and application in research and industry, primarily serving as catalysts, adsorbents, and ion exchangers (Flanigen, 1991). These materials are commercially available in powdered form or can be tailored to desired particle sizes and shapes, such as spheres or rods. However, utilizing zeolite powder, especially in liquid mediums, presents drawbacks, including difficulties in separation due to particle agglomeration and mass transfer limitations due to large sizes. One promising approach to overcome these issues involves dispersing zeolites on a suitable support material.

Plant fibers offer a promising avenue for zeolite dispersion. Valtchev et al. (1994) successfully coated zeolite A on sheets of vegetal fibers, varying the amount of lignin and cellulose content. Their study revealed that hydroxide ions in the aluminosilicate gel disrupt hydrogen bonds in cellulose, generating hydroxyl groups that promote zeolite nucleation. Moreover, lignin content hinders the crystallization of zeolite A on the fiber surface (Valtchev et al., 1994). Besides, Sano et al. (1992) suggested that OH groups in cellulose are favorable sites for zeolite crystallization. In a recent study, Krukkratoke et al. (2022) synthesized zeolite NaY within Lead tree wood by incorporating the wood into the zeolite gel before hydrothermal treatment. Acid-refluxed wood resulted in the formation of NaY, whereas untreated wood led to the

production of NaP. It is worth noting that composition and morphology play a vital role in determining the zeolite formation process. Therefore, the work in Chapter III aims to investigate zeolite synthesis in bamboo wood.

Bamboo wood has gained attention (Su et al., 2019) as a carbon material to prepare zeolite-carbon composite because it is abundant in regions of Asia including Thailand, inexpensive, porous, and fast-growing. The wood, prevalent in tropical and subtropical regions, possesses a cellular and porous structure. Its fibrous cellular arrangement encompasses large macropores, approximately 100 μm in vessels, between 10 to 50 μm in phloem, and triangular pores measuring about 5 μm (Chen et al., 2018). This unique morphology renders bamboo wood an ideal support material for zeolite dispersion. The work in Chapter III compares the percent and distribution of zeolite NaY inside untreated and acid-treated wood. The wood-zeolite composite is evaluated as an adsorbent for the removal of nickel ions from aqueous solutions.

In Chapter IV, the best synthesis condition of wood-zeolite composite from Chapter III was adapted to produce a smaller size of zeolite Y in treated wood-zeolite composite (RWZ). The composite was carbonized under an inert atmosphere, resulting in zeolite-activated carbon composite (Z-AC) which was used for CO_2 adsorption. The adsorption behavior of CO_2 gas on Z-AC. The behavior of nano-sized and micron-sized zeolite Y particles on the CO_2 adsorption capacity was compared. The composite materials were characterized to elucidate the adsorption and structural properties.

Chapter V studies the impact of the forms of zeolite Y on copper-based catalysts to produce H_2 gas from ethanol steam reforming (ESR). This interest is driven by the substantial hydrogen yield achievable through ESR and that ethanol, the primary feedstock for this process, is predominantly derived from renewable biomass sources. This characteristic aligns with the growing emphasis on sustainable energy solutions and the utilization of biomass resources (Llorca et al., 2002; Zhang et al., 2014). Researchers aim to harness hydrogen as a clean and efficient energy carrier because of the advantages of ESR, such as its high hydrogen yield and reliance on biomass-derived ethanol.

Extensive research efforts have been dedicated to exploring various catalytic systems for ESR. These investigations have focused on noble metal-based catalysts, such as rhodium (Rh), ruthenium (Ru), platinum (Pt), and palladium (Pd), as well as non-noble metal-based catalysts, including copper (Cu), nickel (Ni), and cobalt (Co) (Coronel et al., 2014; Rossetti et al., 2014; Li et al., 2016). Noble metal catalysts have demonstrated remarkable activity and stability in ESR reactions. However, their widespread application on a large scale is hindered by their high cost, primarily due to

their limited availability and the expense associated with their extraction and processing (Zhang et al., 2012; Palma et al., 2014). As a result, alternative catalysts, particularly those based on non-noble metals, have garnered significant interest.

Non-noble transition metals that are active for ERS include Co, Ni, and Cu (Lin et al., 2015; Haryanto et al., 2005; Inokawa et al., 2010). Besides, Cu is an active catalyst in the methanol steam reforming route due to selective to H_2, low CO yield as an undesired product for fuel cells and active at a low temperature of catalytic testing (Sá et al., 2010). Chapter V reports the preparation of Cu-based catalyst and the pathway of hydrogen production from ethanol conversion is investigated. Zeolite NaY was used as a catalyst support due to its high surface area, stability, well-defined porous structure, and affordable cost (D'Hondt et al., 2008; de Andrade et al., 2020; Khaleque et al., 2020). Zeolite Y could be prepared in sodium, ammonium and proton forms. Those forms have different acid-base properties and could result in different metal species and dispersion.

Chapter V aims to compare the forms of zeolite Y as the supports of copper catalysts for ethanol conversion to H_2 gas. The change of Cu catalyst during catalytic testing was followed by *operando* X-ray Absorption Spectroscopy (XAS) coupled with gas chromatography and mass spectrometry to elucidate structural properties and the selective pathway of H_2 formation. Understanding these aspects is contributed to the development of H_2 production from ethanol using copper-based zeolite catalysts.

1.2   Scope and limitation of the study

This thesis comprehensively explores the dispersion of zeolite NaY on wood, the adsorption behavior of CO_2 on zeolite-carbon composites, and the hydrogen production process from ethanol conversion using zeolite Y-supported copper catalysts.

In Chapter III, zeolite NaY was crystallized on both untreated and acid-treated bamboo wood according to the previously verified approach (Ginter, 2016; Lechert and Staelin, 2016). This section examined the synthesis process and characterization of the resulting wood-zeolite composite. Additionally, the composite's effectiveness in adsorbing Ni (II) ions was investigated.

Chapter IV explored the adsorption behavior of CO_2 gas on a zeolite-activated carbon composite. The zeolite-carbon composite was synthesized following the best condition of the previous part, and the prepared composite was activated under an inert atmosphere. The study specifically examined the adsorption properties of nano-sized and micron-sized particles of zeolite Y.

Chapter V dedicated to the preparation of copper-based catalysts using various forms of zeolite as a support. The catalysts were synthesized and characterized. Their performance in the conversion of ethanol to produce H_2 gas was evaluated by *Operando* XAS.

1.3   References

Chen, G., Luo, H., Yang, H., Zhang, T., and Li, S. (2018). Water effects on the deformation and fracture behaviors of the multi-scaled cellular fibrous bamboo. *Acta Biomaterialia, 65*, 203-215.

Coronel, L., Múnera, J. F., Tarditi, A. M., Moreno, M. S., and Cornaglia, L. M. (2014). Hydrogen production by ethanol steam reforming over Rh nanoparticles supported on lanthana/silica systems. *Applied Catalysis B: Environmental, 160*, 254-266.

D'Hondt, E., Van de Vyver, S., Sels, B. F., and Jacobs, P. A. (2008). Catalytic glycerol conversion into 1, 2-propanediol in absence of added hydrogen. *Chemical communications,* (45), 6011-6012.

de Andrade, T.S., Souza, M.M., and Manfro, R.L. (2020). Hydrogenolysis of glycerol to 1, 2-propanediol without external H_2 addition in alkaline medium using Ni-Cu catalysts supported on Y zeolite. *Renewable Energy, 160*, 919-930.

Flanigen, Edith M. (1991). Zeolites and molecular sieves an historical perspective. In *Studies in surface science and catalysis* (Vol. 58, pp. 13-34): Elsevier.

Ginter, D. (2016). Linde Type Y. In Svetlana Mintova (Ed.), *Verified syntheses of zeolitic materials* (third ed., pp. 221-223): The Synthesis Commission of the International Zeolite Association.

Haryanto, A., Fernando, S., Murali, N., and Adhikari, S. (2005). Current status of hydrogen production techniques by steam reforming of ethanol: a review. *Energy & Fuels, 19*(5), 2098-2106.

Inokawa, H., Nishimoto, S., Kameshima, Y., and Miyake, M. (2010). Difference in the catalytic activity of transition metals and their cations loaded in zeolite Y for ethanol steam reforming. *International journal of hydrogen energy, 35*(21), 11719-11724.

Khaleque, A., Alam, M. M., Hoque, M., Mondal, S., Haider, J. B., Xu, B., ..., and Moni, M. A. (2020). Zeolite synthesis from low-cost materials and environmental applications: A review. *Environmental Advances, 2*, 100019.

Krukkratoke, P., Keawkumay, C., Tayraukham, P., Prompiputtanapon, K., Khemthong, P., Prayoonpokarach, S., and Wittayakun, J. (2022). Strategic Synthesis to Disperse Zeolite NaY in Lead Tree Wood. *Crystals, 12*(4), 504.

Lechert, H., and Staelin, P. (2016). Linde Type X. In Svetlana Mintova (Ed.), *Verified syntheses of zeolitic materials* (third ed., pp. 215-217): The Synthesis Commission of the International Zeolite Association.

Li, D., Li, X., and Gong, J. (2016). Catalytic reforming of oxygenates: state of the art and future prospects. *Chemical reviews, 116*(19), 11529-11653.

Lin, J., Chen, L., Choong, C. K. S., Zhong, Z., and Huang, L. (2015). Molecular catalysis for the steam reforming of ethanol. *Science China Chemistry, 58*, 60-78.

Llorca, J., Homs, N., Sales, J., and de la Piscina, P. R. (2002). Efficient production of hydrogen over supported cobalt catalysts from ethanol steam reforming. *Journal of catalysis, 209*(2), 306-317.

Palma, V., Castaldo, F., Ciambelli, P., and Iaquaniello, G. (2014). CeO_2-supported Pt/Ni catalyst for the renewable and clean H_2 production via ethanol steam reforming. *Applied Catalysis B: Environmental, 145*, 73-84.

Sano, T., Kiyozumi, Y., Maeda, K., Toba, M., Niwa, S. I., and Mizukami, F. (1992). Materials chemistry communications. New preparation method for highly siliceous zeolite films. *Journal of Materials Chemistry, 2*(1), 141-142.

Su, M., Zhang, R., Li, H., Jin, X., Li, J., Yue, X., and Qin, D. (2019). In situ deposition of MOF199 onto hierarchical structures of bamboo and wood and their antibacterial properties. *RSC Advances, 9*(69), 40277-40285.

Valtchev, V., Mintova, S., Vulchev, I., and Lazarova, V. (1994). Influence of reactive radicals in cellulose fibres on the formation of zeolite coatings. *Journal of the Chemical Society, Chemical Communications*(18), 2087-2088.

Zhang, C., Li, S., Li, M., Wang, S., Ma, X., and Gong, J. (2012). Enhanced oxygen mobility and reactivity for ethanol steam reforming. *AIChE journal, 58*(2), 516-525.

Zhang, J., Zhong, Z., Cao, X. M., Hu, P., Sullivan, M. B., and Chen, L. (2014). Ethanol steam reforming on Rh catalysts: theoretical and experimental understanding. *ACS Catalysis, 4*(2), 448-456.

CHAPTER II
LITERATURE REVIEW

Literature review is divided into two parts: preparation of zeolite-carbon composite as an adsorbent and using zeolite Y-supported copper catalyst for hydrogen production from ethanol steam reforming.

2.1   Preparation of wood-zeolite composite

2.1.1   Background of zeolite NaY

Zeolite NaY belongs to faujasite (FAU) family with a framework containing double 6 rings (D6R) linked through sodalite cages (SOD) generating supercage (Baerlocher and McCusker, 2021). It has a window diameter of 7.4 Å. Extraframework cation sites locate at the following positions shown in Figure 1. Site I is visible in the hexagonal prism, while site I' is visible in the sodalite cage, facing site I. Site II is in the sodalite cage, facing position II, while site II' is at the center of the hexagonal window inside the supercage. Finally, site III is above a square window that is sandwiched between two other square windows, and it is on the square window's edge. Cations located at different sites would be expected to affect catalytic properties in different ways (Kaduk and Faber, 1995; Zhang et al., 2015).
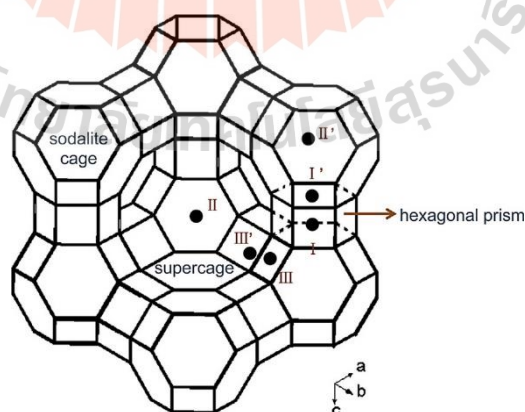
Figure 2.1 Framework structure of FAU zeolite. Reprinted (adapted) with permission from (Zhang et al., 2015). Copyright 2015 Applied Catalysis A: General.

Zeolite Y in sodium form (NaY) can be synthesized by a hydrothermal method (Mintova, 2016). In the first part of this work, zeolite Y is used as an adsorbent for the removal of Ni(II) ions.

2.1.2 Preparation of wood-zeolite composite as an adsorbent

The rapid advancement of industry and infrastructure necessitates the further utilization of water resources to meet human consumption needs, recognizing water as a vital and indispensable resource for life on Earth (Ibarrola Rivas et al., 2016). The significance of monitoring groundwater quality stems from the fact that a considerable portion of the global population relies on groundwater as a drinking water source (Liu et al., 2020; Wen et al., 2018). Water pollution poses a major concern, particularly due to toxic metals originating from mining activities and metal processing. Unlike organic pollutants that are biodegradable, these metals tend to accumulate in living organisms, thereby affecting both human health and environmental pollution. Sorption, which is a cost-effective and straightforward technique, is widely recognized for its effectiveness in removing metal ions from water (Krstić et al., 2018; Venkatesan et al., 2014). Prasad et al. (2018) emphasized the importance of an environmentally friendly, inexpensive, and efficient sorbent that can handle a broad range of pollutant concentrations.

Among the potential solutions for water treatment, zeolites stand out due to their environmentally friendly characteristics. Flanigen (1991) provides a comprehensive review of the history of zeolites and molecular sieves, highlighting their discovery, the development of synthetic zeolites, and their commercial applications as adsorbents and catalysts. Zeolites have attracted research attention for over 250 years, finding applications in various fields such as catalysis, medicine, veterinary medicine, agriculture, and different industries including food, textiles, and more recently, water treatment. Numerous studies have demonstrated the effectiveness of zeolites in water treatment (Krstić, 2021). R. M. Milton and D. W. Breck made a pivotal discovery in the late 1940s to early 1950s when they developed the commercially significant synthetic zeolites A, X, and Y. This breakthrough led to the introduction of these synthetic zeolites as a novel class of industrial adsorbents by the Union Carbide Corporation in 1954 (Krstić, 2021).

Of the three types of zeolites mentioned above, zeolite Y is a promising choice for cationic adsorption and gas separation due to its larger pore diameter compared to zeolite A and its lower water sensitivity compared to zeolite X (Boer et

al., 2023). Based on the abovementioned properties, zeolite Y was synthesized and improved for cationic and gas adsorption in this work.

Zeolite powder finds widespread application in various industries, including catalyst manufacturing, petrochemical refining, and gas separation. Its ample surface area and impressive adsorption capacity make it well-suited for a range of processes, including molecular sieving, ion exchange, and catalysis (Gleichmann et al., 2016). However, there are many problems associated with the powder form, including difficulties in separating it from aqueous media during the adsorption process and complications in handling and storage during transportation. As a result, shaped-zeolite materials are commonly formed and applied on an industrial scale to improve these issues (Gleichmann et al., 2016). Moreover, the production of zeolite beads involves a complicated process and requires a binder and hydraulic machine, leading to high costs and time consumption. Many researchers have attempted to reduce the steps and costs of shaped-zeolite materials by growing zeolite on supporting materials (Sano et al., 1992; Valtchev et al., 1994; Krukkratoke et al., 2022).

Sano et al. (1992) prepared zeolite membranes using the hydrothermal method. This material was made by embedding zeolite crystals in polymer or ceramic matrices or by the in-situ crystallization of zeolites on a porous substrate. They found that the hydroxyl groups contained in the cellulose provide unique sites for zeolite crystallization. Valtchev et al. (1994) synthesized zeolite A coated on cellulose fiber. They used various cellulose membranes including softwood CTMP fluff, softwood kraft pulp, and hardwood sulfate pulp which was subsequently bleached. The three types of wood had different lignin contents, approximately 28%, 6%, and 0.1%, respectively. After preparing the membrane, they found that the kraft pulp had two types of fibers. The first type was densely coated by zeolite crystal. This indicates that a higher lignin content resulted in lower crystallization of zeolite A on cellulose fiber. Recently, Krukkratoke et al. (2022) dispersed zeolite NaY on the pellet of lead tree wood and applied it as an adsorbent for nickel (Ni) ion adsorption. The results showed that approximately twenty percent of zeolite in the wood pellet could remove the cationic ions in an aqueous system. Additionally, the adsorbent is easy to separate from the adsorbate solution. However, lead tree wood as a carbon composite material resulted in more zeolite NaP formation than zeolite NaY due to obstructions in the wood and its wood structure. As a result, this work represents another kind of wood, bamboo tree wood, as a carbon source for wood-zeolite composite preparation.

Bamboo has gained attention (Su et al., 2019) for preparing wood-zeolite composites due to its properties, such as being fast-growing, inexpensive,

plentiful in Asia, and having a porous structure. Bamboo possesses a fibrous cellular structure characterized by significant macropores. These macropores have varying sizes within different parts of the bamboo. Bamboo vessels have macropores with a diameter of approximately 100 μm, while the phloem region consists of macropores ranging from 10 to 50 μm. Additionally, triangular pores measuring around 5 μm in size can be observed in bamboo. The uniqueness of wood-like hollow, strong, and round structure has attracted researchers to consider and study it, especially in the field of durability and quality enhancement of wood products. In this wrok, Long sheath bamboo (Thyrsostachys siamensis Gamble) was used. It is bright green when young and becomes dull green when grown up. The culm shape is generally cylindrical and smooth and characterized by nodes along its length. Culms arise from underground rhizomes, which can form dense clumps. The culm bamboo cells include parenchymatous cells. Thus, zeolite NaY inside Long sheath bamboo wood was synthesized via the hydrothermal method. The strong cell walls, high lignin content of around ~23% (Bai et al., 2013), and numerous starch pieces in bamboo wood obstructed the diffusion and crystallization of aluminosilicate gel into the wood. As a result, bamboo wood was treated before use as a solid support in wood-zeolite Y synthesis.

Shi et al. (2018) revealed that thermal acid treatment can break the ester bond of lignin, hemicellulose, and cellulose in biomass, leading to an increase in porosity. They reported that the amount of lignin was reduced by acid treatment and base. Also, both treatments can destroy cell walls and intercellular layers and dissolve the starch in the wood. Yu et al. (2016) studied the effect of HCl on starch-based wood adhesive. They indicated that the glycosidic bond and hydrogen bond between starch molecules were hydrolyzed with an increase in HCl concentration. It also increases hydroxyl groups. In our previous research, Krukkratoke et al. (2022) treated Lead tree wood by refluxing with an HCl solution. They found that refluxing with acid can hydrolyze lignocellulose and remove impurities from the wood, leading to a high crystallinity of zeolite NaY inside the wood. Based on this literature, to decrease the obstacles of high-purity zeolite Y inside bamboo wood, the wood was refluxed with an HCl solution following Krukkratoke et al. (2022). Refluxed and non-refluxed woods were compared and applied for Ni (II) ion adsorption in this research.

2.1.3 Ni (II) ion adsorption on zeolite composite materials

Nickel is widely used in various industrial processes, including mineral processing, electroplating, paint and battery production, as well as the manufacturing of sulfate and porcelain enamel (Akhtar et al., 2004; Farooq et al., 2010; Malamis and

Katsou, 2013). However, prolonged exposure to heavy metals like nickel can have severe health consequences. Nickel has been associated with health issues such as dermatitis, nausea, coughing, chronic bronchitis, gastrointestinal discomfort, reduced lung function, and an increased risk of lung cancer (Farooq et al., 2010; Kurniawan et al., 2006; Arief et al., 2008).

Adsorption and ion exchange are effective methods for removing heavy metals from wastewater, particularly when low-cost sorbents or ion exchangers are employed. These processes offer advantages in removing a wide range of heavy metals from the liquid phase, with typically rapid kinetics (Malamis and Katsou, 2013). Zeolites and zeolite composites have shown promise as adsorbents for removing cationic ions from water. The adsorption of Ni ions typically involves exchangeable cations in the zeolite cavities. These cations, such as sodium (Na^+), potassium (K^+), or calcium (Ca^{2+}), can be exchanged with Ni ions in the aqueous solution. The Ni ions could coordinate with oxygen in the zeolite lattice. The specific nature and availability of these active sites depend on the type of zeolite and its structural characteristics, including the Si/Al ratio and specific framework elements (Boyd et al., 1947; Biškup et al., 2014).

For instance, Hui et al. (2016) prepared zeolite 4A using recycled coal fly ash via the hydrothermal method and employed it as an adsorbent for metal ions. In their experiment, 0.5 grams of the adsorbent were added to 100 mL of a solution containing a mixture of Ni (II) ions ranging from 50 mg/L. The initial pH of the solution was set at 3, and the contact time between the adsorbent and the solution was 240 minutes. The adsorption capacity of this adsorbent was 8.96 mg/g. Table 2.1 shows that zeolite Clinotilolite exhibited a low adsorption capacity (1.61 mg/g) due to its low surface area and low Na ion concentration. Therefore, the type of zeolite significantly influences the adsorption capacity.

Table 2.1 Examples of Ni (II) ion adsorption on zeolite and zeolite-carbon composite.

Adsorbent	Adsorption capacity (q_e, mg·g^{-1})	Reference
Zeolite 4A	8.96	Hui et al. (2016)
Clinoptilolite	1.61	Argun et al. (2008)
Zeolite FAU-AC composite	70.32	Jha et al. (2008)
Zeolite Y-hollow fibers membrane	120.50	Muhamad et al. (2018)
Wood-zeolite NaP composite	3.75	Krukkratoke et al. (2022)

The properties of zeolites have been improved by incorporating them into composites with carbon materials, such as zeolite FAU-activated carbon composite, zeolite Y-hollow fiber composite, and wood-zeolite NaP composite, for the removal of cationic ions from water (Jha et al., 2008; Muhamad et al., 2018; Krukkratoke et al., 2022). Table 2.1 presents the high adsorption capacities of these composites when used as adsorbents. Therefore, in this thesis, the prepared composite was employed as an adsorbent and compared with the lead tree wood-zeolite composite from Krukkratoke's work.

2.1.4 CO_2 adsorption on zeolite-activated carbon composite

Global warming is primarily caused by human activities that release greenhouse gases into the Earth's atmosphere. These greenhouse gases act like a blanket, trapping heat and causing a rise in the planet's average temperature. The major greenhouse gas is carbon dioxide (CO_2), accounting for a significant 60% of all greenhouse gases (Yang et al., 2017; Chen et al., 2016; Wan et al., 2018). This substantial proportion can be attributed to its extensive release during industrial processes and fuel combustion. Currently, the concentration of CO_2 in our atmosphere exceeds 400 parts per million (ppm), far surpassing the pre-industrial era level of 300 ppm. Furthermore, CO_2 in natural gas reduces its heat value, creating a strong impetus to mitigate CO_2 concentration (Tseng et al., 2015; Oh, 2010). Carbon capture and storage (CCS) has emerged as a viable approach to curbing this greenhouse gas (Gunawan et al., 2018).

In the past, CO_2 capture involved the utilization of various ethanolamine solutions through a chemical absorption mechanism. However, this method incurred high operational costs due to significant absorbent losses and energy requirements (Tseng et al., 2015). As a result, an alternative solution based on adsorption by porous solids has garnered considerable interest due to its potential for energy efficiency and operational simplicity. The development of an effective CO_2 adsorbent necessitates meeting three critical criteria: high adsorption capacity for CO_2, favorable adsorption/desorption kinetics under operating conditions, and long-term durability across repeated adsorption/desorption cycles (Tseng et al., 2015; Gunawan et al., 2018).

Physisorption-based materials such as carbons, zeolites, ordered mesoporous materials, and silica are widely employed for CO_2 capture (Yu et al., 2012). Among these materials, zeolites and carbons have emerged as up-and-coming candidates. Zeolites, characterized by their alumina-silicate composition, exhibit a high degree of microporosity, allowing for facile adjustment of their pore surface based on

specific application requirements. Zeolite pores can exist in the form of micropores (<2 nm) or mesopores (2-50 nm), exhibiting a well-distributed pore structure. However, zeolites possess the drawback of having a lower surface area than carbon materials and are susceptible to CO_2 poisoning in the presence of moisture (Chung, 2010; Caglayan and Aksoylu, 2013).

On the other hand, carbon materials offer significantly high specific surface areas ranging from 300 to 1000 $m^2 \cdot g^{-1}$ or even higher, albeit with lower porosities compared to zeolites. Zeolites typically possess a cage-like pore structure with a molecular size of 0.5-1.2 nm. For instance, a highly porous zeolite can capture CO_2 in the range of 0.45–6.52 millimoles per gram ($mmol \cdot g^{-1}$) at room temperature, whereas high surface area carbon can achieve a CO_2 capture capacity of 21.29 mmol g^{-1} at room temperature (Gunawan et al., 2018). Leveraging the findings from these studies, the concept of combining both materials has emerged, aiming to synthesize a material that capitalizes on the advantages of both zeolites and carbons. By doing so, the limitations associated with each material can be mitigated, facilitating the realization of a hybrid material that exhibits high porosity and surface area, thereby maximizing the adsorption potential for CO_2. This material synthesis can be accomplished through the preparation of a zeolite-carbon composite, providing a promising avenue for further exploration and development in the field.

Ma et al. (2012) prepared zeolite X/carbon composite materials using the hydrothermal method. In this study, two sets of zeolite X/activated carbon composites were synthesized using a sequential procedure involving CO_2 activation of elutrilithe and pitch mixtures, followed by hydrothermal crystallization in an alkaline solution. Subsequently, a surface modification step was carried out using a diluted NH_4Cl solution. Before and after the surface modification, the CO_2 and N_2 adsorption capacities of these composites were evaluated under different pressures ranging up to 101 kPa at temperatures of 0 and 25℃, respectively. They found that the unmodified composites exhibited a greater CO_2 adsorption capacity and a more pronounced steepness in the CO_2 isotherm curve. In contrast, the modified composites displayed a lower adsorption capacity and a reduced slope in the CO_2 isotherm. It can be concluded that the activation of zeolite-activated carbon composites can perform in CO_2 adsorption.

Rostami et al. (2016) synthesized zeolite 13X-carbon composite for CO_2/N_2 adsorption study. The synthesis process to produce the composite material involved the hydrogel preparation step. Initially, powdery carbon was introduced into a sodium silicate solution, followed by a 15-minute primary mixing period.

Subsequently, a sodium aluminate solution was added drop by drop with vigorous mixing to ensure efficient dispersion of the carbon and achieve a homogeneous gel. Notably, for every 1000 grams of hydrogel, 8 grams of powdery carbon were utilized during the hydrogel preparation step in the synthesis of the zeolite-activated carbon composite. Moreover, the obtained composites were in powder form and unsuitable for study in a column system. As a result, the product in powder form was mixed with bentonite as a binder to build pellets of the composite. In the adsorption study, they compared the composite with parent zeolite X. Upon comparing the results obtained from SZX (solely zeolite X) and ACZC (zeolite X with approximately 7 wt% activated carbon) composites, it was observed that the addition of activated carbon to the zeolite structure led to slight improvements in the properties of the zeolite for gas adsorption applications. This finding suggests that incorporating an optimal amount of carbon into the zeolite structure can yield enhanced results and increased selectivity. Additionally, it is anticipated that this composite adsorbent may outperform conventional zeolite 13X in the separation of CO_2 and N_2 gases, particularly in the context of capturing carbon emissions from flue gas streams. This represents a significant aspect of carbon capture research and highlights the potential suitability of the composite adsorbent for addressing these concerns.

In similar materials, Gunawan et al. (2018) studied the behavior of CO_2 adsorption of zeolite Y-templated carbon. The primary objective of this study was to investigate the adsorption and desorption behavior of carbon dioxide (CO_2) on a micro-mesoporous zeolite-Y-templated carbon (ZTC) at different temperatures. The ZTC material was synthesized through a process involving sucrose impregnation, carbonization, and template removal. The gravimetric method was employed to assess the adsorption and desorption characteristics. The experimental results revealed that the CO_2 adsorption capacity on ZTC was 9.51 wt% at 30°C, 5.60 wt% at 40°C, and 3.47 wt% at 50°C. Furthermore, the desorption percentages reached 59.83%, 69.70%, and 77.5% at the respective temperatures. Analysis of the adsorption process indicated that at 30°C and 40°C, the adsorption behavior followed a pseudo-second-order kinetic model, while at 50°C, it adhered to intra-particle diffusion. Thermodynamic analyses suggested that the adsorption mechanism was primarily physisorption-based. Overall, this study sheds light on the adsorption and desorption properties of CO_2 on ZTC at different temperatures, providing valuable insights into the behavior and potential applications of this material for CO_2 capture. Zeolite Y on the template showed good adsorption capacity, but it was in powder form leading to unsuitability in some systems such as a column reactor. In addition, the preparation process of the zeolite-activated

carbon composite was still complicated and time-consuming (Ha et al., 2012 and Rostami et al., 2016). Thus, an alternative method to prepare the composite that was adapted from Krukkratoke et al. (2022) was introduced and investigated in this thesis for CO_2 adsorption study.

In the first part, the RWZ composite has the highest adsorption capacity in Ni (II) ion adsorption. However, the particle size of the zeolite Y in the composite is still large (3-4 μm), and the surface area of the carbon (bamboo wood) in the composite is low. As a result, adjusting the water volume or alkalinity in seed and feedstock gels to produce nanosize zeolite in the composite was done, and the composites were carbonized in an inert atmosphere at 700°C to obtain the zeolite-activated carbon composite for CO_2 adsorption study. Besides, the composite in this work was in pellet form after the activation process and did not require a binder.

In addition, Eskandari et al. (2016) prepared zeolite X with nano-size and micron size by the hydrothermal method for CO_2/CH_4 adsorption. They indicated that the decrease in particle size, specifically from micrometer to nanometer scale, led to a notable increase in carbon dioxide adsorption capacity on X zeolite nanoparticles. The adsorption capacity exhibited a significant improvement of approximately 28%, rising from 5.067 to 6.536 mmol/g when measured at a temperature of 15°C and a pressure of 20 bar. As a result, the particle size effect of zeolite Y in the composite on the adsorption capacity of CO_2 was compared.

From the literature, the carbon material of the composite should be activated. The process is time and energy-consuming in the carbonization and activation steps. Although the materials are rich in active sites, these samples were still powdered. As a result, the forming process is essential to use as an adsorbent on an industrial scale. For this purpose, the carbon should be activated to increase the active sites of the zeolite-carbon material, and the zeolite-carbon composite also took time in those processes. Consequently, a wood-zeolite composite is suggested in this research to solve these drawbacks. The wood prepared for this composite should have a large porous structure and a solid shape.

2.2   Modification of zeolite Y with copper for hydrogen production via ethanol steam reforming

2.2.1   Hydrogen production based on steam reforming of ethanol

The world's population is growing exponentially, and industrialization is advancing rapidly, leading to an increasing global demand for energy (Briefing, 2013; da Silva Veras et al., 2017). Currently, the majority of energy consumed worldwide

(84%) relies on traditional non-renewable fossil fuel sources, which contribute to accelerated greenhouse gas emissions (Gokarn et al., 2013; Martin and Diaz, 1991; Anil et al., 2022; Escalante et al., 2022). The average atmospheric CO_2 concentration reached 410.5 ppm in 2019 and continues to rise at a rate of approximately 2 ppm per year, raising concerns about the strong association between energy production and global warming (Anil et al., 2022). In response to this situation, efforts have been made to mitigate carbon emissions, and hydrogen energy has emerged as a promising clean and sustainable energy source. Hydrogen reactions only produce water as a byproduct (Ni et al., 2006; Chen et al., 2020), making large-scale hydrogen production a significant milestone in achieving net-zero emissions and ensuring environmental sustainability.

Fossil fuel reserves are limited and unevenly distributed worldwide, leading to price increases and supply disparities due to political instability among nations. These factors highlight the need to reduce reliance on fossil fuels and transition to renewable energy sources (Gordon et al., 2019). While renewable energy options such as solar, wind, biomass, and various forms of ocean and geothermal energy hold promise, they often have location-specific limitations, intermittent availability, and stability issues.

Hydrogen can be produced from a range of feedstocks, including methanol, ethanol, natural gas, diesel, gasoline, and other hydrogen-containing substances (Kalamaras and Efstathiou, 2013). However, despite their drawbacks and negative environmental impacts, fossil fuels currently remain the predominant feedstock for hydrogen production in various industries (Pareek et al., 2020; Rosen and Koohi-Fayegh, 2016). Extensive research has been conducted on hydrogen synthesis from methane and methanol using reforming processes, which have established industrial procedures (Chen et al., 2020). However, bioethanol derived from biomass conversion and fermentation offers advantages over methanol. Bioethanol has a higher specific energy content, is less toxic, has a higher hydrogen content, and is safer to handle (Nanda et al., 2017; Highfield et al., 1994). These factors make it an attractive feedstock for hydrogen generation, aligning with the goal of environmental sustainability (Hunt et al., 2022). Global ethanol production reached 120 billion liters in 2017 and is projected to increase by 14% over the next decade, as estimated by the International Energy Agency (Bajpai, 2020). Therefore, the investigation of ethanol steam reforming (ESR) can provide valuable insights into the process.

The primary pathway of the ethanol steam reforming (ESR) reaction involves three key reactions: ethanol dehydrogenation (Eq. (1)), acetaldehyde steam reforming (Eq. (2)), and the water gas shift reaction (Eq. (3)). The reaction pathway for

ethanol steam reforming is depicted in Figure 2.2, considering previous studies (Haryanto et al., 2005; Mattos et al., 2012; Zanchet et al., 2015; Sharma et al., 2017). At lower temperatures, ethanol dehydrogenation (Eq. (1)) is the dominant reaction, producing acetaldehyde and hydrogen. As the reaction temperature increases, ethanol conversion and the selectivities of hydrogen and CO_x compounds rise due to successive acetaldehyde steam reforming and the water gas shift reaction at higher temperatures. However, the ESR process is accompanied by various undesired side reactions, including ethanol dehydration (Eq. (4)), acetaldehyde decomposition (Eq. (7)), and coke formation. Of particular concern is the suppression of acetaldehyde decomposition, as it generates inactive methane and diminishes hydrogen selectivity. Research suggests that promoting the formation of adsorbed acetate species from acetaldehyde effectively enhances acetaldehyde steam reforming while curbing acetaldehyde decomposition into CH_4 (Sekine et al., 2014; Ogo et al., 2015). Furthermore, ESR can involve various coke formation reactions, such as ethylene decomposition (Eq. (6)), methane decomposition (Eq. (7)), and CO disproportionation (Boudouard reaction; Eq. (8)). Mitigating ethylene and methane formation while promoting the water gas shift reaction helps suppress coke deposition (Mattos et al., 2012; Zanchet et al., 2015; Sharma et al., 2017). Maintaining an optimal steam/ethanol molar ratio is crucial for coke control during ESR. Increasing this ratio has proven effective in suppressing coke formation (Mattos et al., 2012). However, excessive steam introduction should be avoided to prevent compromising energy efficiency and escalating heating costs (Ogo and Sekine, 2020).
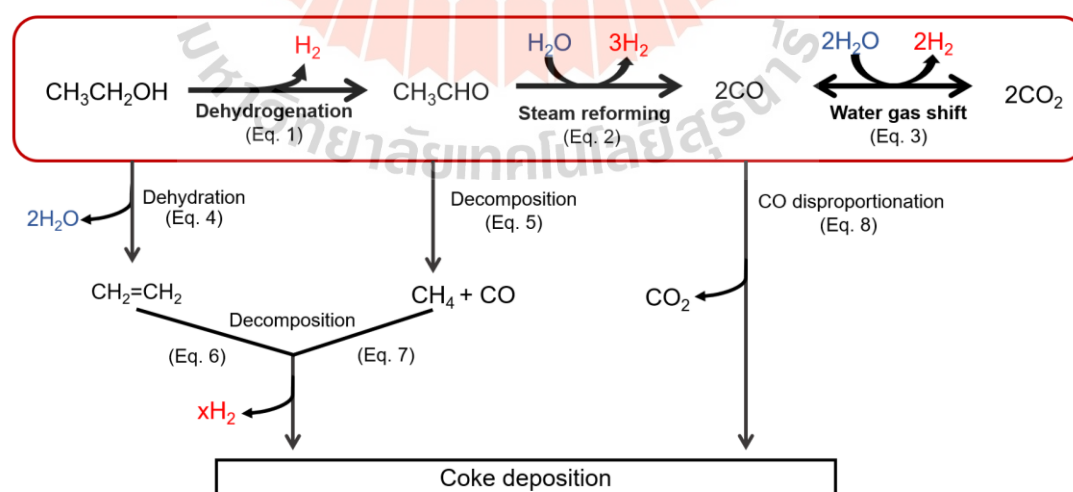
Figure 2.2 Reaction pathway of ethanol steam reforming via acetaldehyde steam reforming. Reprinted (adapted) with permission from (Ogo and Sekine, 2020). Copyright 2020 Fuel Processing Technology.

(Main reaction path)

Ethanol dehydrogenation:

$$C_2H_5OH(g) \rightarrow CH_3CHO(g) + H_2(g) \qquad \Delta H_r°_{298} = 68.9 \text{ kJ/mol} \qquad (1)$$

Acetaldehyde steam reforming:

$$CH_3CHO(g) + H_2O(g) \rightarrow 2CO(g) + 3H_2(g) \qquad \Delta H_r°_{298} = 186.8 \text{ kJ/mol} \qquad (2)$$

Water gas shift reaction:

$$CO(g) + H_2O(g) \rightarrow CO_2(g) + H_2(g) \qquad \Delta H_r°_{298} = 41.4 \text{ kJ/mol} \qquad (3)$$
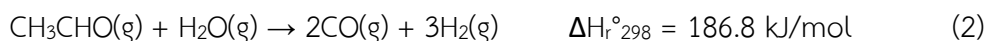
(Side reactions)

Ethanol dehydration:

$$C_2H_5OH(g) \rightarrow C_2H_4(g) + H_2O(g) \qquad \Delta H_r°_{298} = 45.5 \text{ kJ/mol} \qquad (4)$$

Acetaldehyde decomposition:

$$CH_3CHO(g) \rightarrow CH_4(g) + CO(g) \qquad \Delta H_r°_{298} = 19.3 \text{ kJ/mol} \qquad (5)$$

(Coke formation reactions)

Ethylene decomposition:

$$C_2H_4(g) \rightarrow 2C(s) + 2H_2(g) \qquad \Delta H_r°_{298} = 52.3 \text{ kJ/mol} \qquad (6)$$

Methane decomposition

$$CH_4(g) \rightarrow C(s) + 2H_2(g) \qquad \Delta H_r°_{298} = 74.9 \text{ kJ/mol} \qquad (7)$$

CO disproportionation (Boudouard reaction)

$$2CO(g) \rightarrow C(s) + CO_2(g) \qquad \Delta H_r°_{298} = 172.6 \text{ kJ/mol} \qquad (8)$$

In order to achieve a high hydrogen yield at a low cost, it is crucial to optimize various reaction parameters in a thriving hydrogen economy. These parameters include the reaction temperature, catalyst type (whether noble or non-noble metal), support type, flow rate, ethanol-to-steam ratio, oxygen input, and more (Ogo and Sekine, 2020). Additionally, a comprehensive understanding of the mechanisms underlying ethanol reforming requires the determination of the physicochemical properties of the catalyst. These properties include the BET surface area, crystallite size, dispersion, reducibility capacity, and the metal oxides' acidic and basic characteristics. By optimizing these parameters and investigating the catalyst's properties, we can better comprehend the ethanol reforming process and ultimately achieve the desired high hydrogen yield at a low cost. As a result, metal-based catalysts were improved and applied for the study of ethanol steam reforming to produce hydrogen.

2.2.2 Transition metal-based catalysts for catalytic study of ethanol steam reforming

The introduction of a catalyst plays a crucial role in ethanol steam reforming (ESR) by facilitating several important processes. Firstly, catalysts help lower

the required reaction temperature, thereby improving the overall efficiency of the process. They also enhance the conversion of both ethanol and water, leading to increased yields of hydrogen. Additionally, catalysts play a vital role in maximizing the selectivity of hydrogen production while minimizing the formation of unwanted intermediate products. This reduction in unwanted byproducts helps prevent carbon deposition, which, in turn, reduces catalyst deactivation. Numerous catalysts have been investigated for the ESR reaction, utilizing various combinations of active metals, supports, and promoters. The active metals used in ESR catalysts can be broadly categorized into two groups: noble metals and non-noble metals. Noble metals such as rhodium (Rh), ruthenium (Ru), palladium (Pd), and platinum (Pt) exhibit excellent catalytic performance. Among them, rhodium has been reported as the most effective active metal for ESR. However, the high cost and limited availability of noble metals make them less desirable for practical applications.

As an alternative, non-noble metals such as copper (Cu), cobalt (Co), and nickel (Ni) have gained significant attention as active metals for ESR. These non-noble metals are preferred due to their lower cost, higher availability, and comparable catalytic activities. They serve as effective catalysts in dissociating C-C bonds in ethanol, contributing to the overall efficiency of the ESR process (Hou et al., 2015). However, many publications on Co- and Ni-based catalysts investigate and elucidate the selective and catalytic performance (Ogo and Sekine, 2020). In contrast to copper, few reports showed the catalytic testing of Cu-based catalysts for the ESR reaction, but more research in methanol steam reforming (MSR) was found (Jones et al., 2009; Matsumura and Ishibe, 2009; Khanchi et al., 2022). Therefore, this work used copper metal as an active site to study the catalytic activity and selective pathway of hydrogen production from ethanol conversion.

One significant drawback of non-noble metal catalysts, such as those based on cobalt, is their rapid deactivation under reaction conditions. Deactivation can occur due to sintering and coke formation, but these issues can be mitigated by selecting an appropriate support material. The influence of the oxide support on catalyst activity in the ESR process has been studied for various materials, including Al_2O_3, SiO_2, ZrO_2, Nb_2O_5, MgO, and CeO_2 (Llorca et al., 2002; Benito et al., 2005;, Frusteri et al., 2006, Contreras et al., 2014; Grzybek et al., 2020; Riani et al., 2020).

In the literature, Khanchi et al. (2022) synthesized catalysts based on SiO_2, Al_2O_3, and SiO_2-Al_2O_3 with varying Si/Al ratios to investigate the influence of the support nature on catalyst performance in the methanol steam reforming process. The catalytic reaction was conducted in a quartz reactor under atmospheric conditions,

with a temperature range of 150°C to 300°C and a weight hourly space velocity (WHSV) of 1.8 h^{-1}. They found that the SiO$_2$-Al$_2$O$_3$-based catalysts exhibited superior performance in the steam reforming process compared to SiO$_2$ and Al$_2$O$_3$-based catalysts. At a temperature of 300°C, the yield percentages were 87.2% for Si/Al = 0.01, 82.4% for Si/Al = 0.05, 76.6% for Si/Al = 0.1, and 69.1% for Si/Al = 0.2. In contrast, the SiO$_2$-based catalyst yielded 59.3%, while the Al$_2$O$_3$-based catalyst produced 49.5%. Furthermore, the γ-Al$_2$O$_3$-based catalyst resulted in a relatively high amount of carbon monoxide (CO) production, with percentages of 6.8% at 150°C and 9.9% at 300°C. On the other hand, the SiO$_2$-Al$_2$O$_3$-based catalysts exhibited significantly lower CO production. Additionally, an increase in the Si/Al ratio in the SiO$_2$-Al$_2$O$_3$-based catalysts led to a decrease in catalyst reductivity. However, the high copper metal loading on the aluminosilicate framework like zeolite is well-known because of its properties. Therefore, a copper-based zeolite catalyst was prepared in this study.

Furthermore, the role of the support is to enhance the dispersion of the metallic active phase through metal-support interactions, thereby improving catalytic performance and reducing the formation of carbon species during the process. High surface area and a porous structure are crucial for ensuring the dispersion of metallic species and increasing their resistance to sintering (Llorca et al., 2002; Da Costa-Serra et al., 2010). Consequently, zeolites such as zeolite Y with a microporous system of channels and cages, known for their high thermal stability and surface area (typically around 400-800 m$^2 \cdot$g^{-1}), are attractive candidates for supporting the metal species (Campos-Skrobot et al., 2008; Chica and Sayas, 2009; Da Costa-Serra and Chica, 2011; Inokawa et al., 2011; Calles et al., 2020; Wang et al., 2020).

The utilization of Cu-zeolites for the ESR process was first reported in 2001 (Łaniecki, 2001), while research on catalytic steam reforming of ethanol using zeolites started appearing in the 1990s (García and Laborde, 1991, Haga et al., 1997; Trimm, 1999). The role of zeolites as supports gained attention again in the work of Campos-Skrobot et al. (2008), where a Rh catalyst supported on NaY zeolite achieved a 68% yield of H$_2$. Vizcaino et al. (2007) reported Cu-Ni-based catalysts supported on nanocrystalline ZSM-5 zeolites for ESR, with an optimal operating temperature identified at 600°C (Vizcaíno et al., 2007).

For example, Inokawa et al. (2010) prepared Ni and Co on zeolite NaY by impregnation and ion exchange methods. They found that the catalytic activity of zeolite Y, with a Si/Al ratio of 2.75, was examined for ethanol steam reforming at a temperature of 300°C. The unloaded Na-Y zeolite exhibited minimal catalytic activity. However, when the zeolite Y was loaded with nickel (Ni) through an incipient wetness

impregnation process, a fraction of the metal was encapsulated as Ni^{2+} ions. This Ni-loaded zeolite Y demonstrated the ability to produce H_2 through ethanol dehydrogenation and ethylene (C_2H_4) through ethanol dehydration. They concluded that cationic in zeolite structure significantly affects the ESR reaction, and a low or medium Si/Al ratio of zeolite can promote the hydrogen yield. In a separate study conducted by the same authors (Inokawa et al., 2010), the focus was on the type of catalysts used. The study explored how the control of basicity, achieved by exchanging alkaline cations within a zeolite (specifically, the exchange of sodium (Na^+) with potassium (K^+) and cesium (Cs^+) cations), influenced the characteristics of both the support material and the metal component. The results showed that this manipulation of basicity led to improvements in reducibility and catalytic activity, resulting in higher yields and selectivity of H_2. It was observed that the selectivity of hydrogen production was influenced by the size of the cation present (Ni/Na_Y < Ni/K_Y < Ni/Cs_Y). Furthermore, consistent with previous findings, the dehydrogenation reaction of ethanol (EtOH) was found to be accelerated by the basicity of the zeolite, while the ethanol dehydration reaction (EDHy) was inhibited. From the literature, zeolite is attractive to be a supporting material because of its large surface area, three-dimensional structure, and acido-basic properties.

From the above literature, we can imply that there are many forms of zeolite that have different surrounding cationic ions, including Na-form, NH_4-form, and H-form. The proton form (HY) is used as acid catalyst. However, a direct ion exchange from sodium ion to proton is not an option due to the instability in acid. As a result, an indirect strategy is employed. NaY is exchanged with ammonium ion (NH_4^+) followed by calination to decompose NH_4^+ to ammonia and protons (Kaduk and Faber, 1995). HY has a higher acidity than NaY, which plays a significant role in many reactions, like the cracking reaction and dehydration (Alam et al., 2018; Deng et al., 2016). From Inokawa's purpose, different forms of zeolite as a supporting material might show different H_2 selectivity and ethanol conversion. Thus, this research studied the cationic ion effect of the zeolite-supported Cu catalyst by varying zeolite forms, including Na-form, NH_4-form, and H-form.

2.3   References

Anil, S., Indraja, S., Singh, R., Appari, S., and Roy, B. (2022). A review on ethanol steam reforming for hydrogen production over Ni/Al2O3 and Ni/CeO$_2$ based catalyst powders. *International Journal of Hydrogen Energy*.

Argun, M. E. (2008). Use of clinoptilolite for the removal of nickel ions from water: kinetics and thermodynamics. *Journal of Hazardous Materials, 150*(3), 587-595.

Arief, V. O., Trilestari, K., Sunarso, J., Indraswati, N., and Ismadji, S. (2008). Recent progress on biosorption of heavy metals from liquids using low cost biosorbents: characterization, biosorption parameters and mechanism studies. *CLEAN–Soil, Air, Water, 36*(12), 937-962.

Baerlocher, C., and McCusker, L. B. (2021). Database of Zeolite Structures: http://www. iza-structure. org/databases. *Google Scholar There is no corresponding record for this reference*.

Bajpai, P. (2020). *Developments in bioethanol*: Springer Nature.

Benito, M., Sanz, J. L., Isabel, R., Padilla, R., Arjona, R., and Daza, L. (2005). Bio-ethanol steam reforming: Insights on the mechanism for hydrogen production. *Journal of Power Sources, 151*, 11-17.

Biškup, B., and Subotić, B. (2004). Kinetic analysis of the exchange processes between sodium ions from zeolite A and cadmium, copper and nickel ions from solutions. *Separation and Purification Technology, 37*(1), 17-31.

Boer, D. G., Langerak, J., and Pescarmona, P. P. (2023). Zeolites as Selective Adsorbents for CO$_2$ Separation. *ACS Applied Energy Materials, 6*(5), 2634-2656.

Boyd, G. E., Schubert, J., and Adamson, A. W. (1947). The exchange adsorption of ions from aqueous solutions by organic zeolites. I. Ion-exchange equilibria1. *Journal of the American Chemical Society, 69*(11), 2818-2829.

Briefing, U. S. (2013). International energy outlook 2013. *US Energy Information Administration, 506*, 507.

Caglayan, B. S., and Aksoylu, A. E. (2013). CO$_2$ adsorption on chemically modified activated carbon. *Journal of Hazardous Materials, 252*, 19-28.

Calles, J. A., Carrero, A., Vizcaíno, A. J., and Megía, P. J. (2020). Agglomerated Co–Cr/SBA-15 catalysts for hydrogen production through acetic acid steam reforming. *International Journal of Hydrogen Energy, 45*(32), 15941-15950.

Campos-Skrobot, F. C., Rizzo-Domingues, R. C., Fernandes-Machado, N. R., and Cantão, M. P. (2008). Novel zeolite-supported rhodium catalysts for ethanol steam reforming. *Journal of Power Sources, 183*(2), 713-716. Bajpai, Pratima. (2020). *Developments in bioethanol*: Springer Nature.

Chen, J., Yang, J., Hu, G., Hu, X., Li, Z., Shen, S., ..., and Fan, M. (2016). Enhanced CO_2 capture capacity of nitrogen-doped biomass-derived porous carbons. *ACS Sustainable Chemistry & Engineering, 4*(3), 1439-1445.

Chen, L., Qi, Z., Zhang, S., Su, J., and Somorjai, G. A. (2020). Catalytic hydrogen production from methane: A review on recent progress and prospect. *Catalysts, 10*(8), 858.

Chen, W. H., and Chen, C. Y. (2020). Water gas shift reaction for hydrogen production and carbon dioxide capture: A review. *Applied Energy, 258*, 114078.

Chica, A., and Sayas, S. (2009). Effective and stable bioethanol steam reforming catalyst based on Ni and Co supported on all-silica delaminated ITQ-2 zeolite. *Catalysis Today, 146*(1-2), 37-43.

Chung, K. H. (2010). High-pressure hydrogen storage on microporous zeolites with varying pore properties. *Energy, 35*(5), 2235-2241.

Contreras, J. L., Salmones, J., Colín-Luna, J. A., Nuño, L., Quintana, B., Córdova, I., ..., and Fuentes, G. A. (2014). Catalysts for H_2 production using the ethanol steam reforming (a review). *International Journal of Hydrogen Energy, 39*(33), 18835-18853.

Da Costa-Serra, J. F., and Chica, A. (2011). Bioethanol steam reforming on Co/ITQ-18 catalyst: Effect of the crystalline structure of the delaminated zeolite ITQ-18. *International Journal of Hydrogen Energy, 36*(6), 3862-3869.

Da Costa-Serra, J., Guil-Lopez, R., and Chica, A. (2010). Co/ZnO and Ni/ZnO catalysts for hydrogen production by bioethanol steam reforming. Influence of ZnO support morphology on the catalytic properties of Co and Ni active phases. *International Journal of Hydrogen Energy, 35*(13), 6709-6716.

da Silva Veras, T., Mozer, T. S., and da Silva César, A. (2017). Hydrogen: trends, production and characterization of the main process worldwide. *International Journal of Hydrogen Energy, 42*(4), 2018-2033.

Escalante, J., Chen, W. H., Tabatabaei, M., Hoang, A. T., Kwon, E. E., Lin, K. Y. A., and Saravanakumar, A. (2022). Pyrolysis of lignocellulosic, algal, plastic, and other biomass wastes for biofuel production and circular bioeconomy: A review of thermogravimetric analysis (TGA) approach. *Renewable and Sustainable Energy Reviews, 169*, 112914.

Farooq, U., Kozinski, J. A., Khan, M. A., and Athar, M. (2010). Biosorption of heavy metal ions using wheat based biosorbents–a review of the recent literature. *Bioresource Technology, 101*(14), 5043-5053.

Frusteri, F., Freni, S., Chiodo, V., Spadaro, L., Di Blasi, O., Bonura, G., and Cavallaro, S. (2004). Steam reforming of bio-ethanol on alkali-doped Ni/MgO catalysts: hydrogen production for MC fuel cell. *Applied Catalysis A: General, 270*(1-2), 1-7.

Gleichmann, K., Unger, B., and Brandt, A. (2016). *Industrial zeolite molecular sieves*: IntechOpen.

Gokarn, S., Sajjanhar, A., Sandhu, R., and Dubey, S. (2013). Energy 2030: Backgrounder. *brookings India*(1), 1-33.

Garzón Gordón, A. J., and Hierro Recio, L. Á. (2019). External Effects of the War in Ukraine: The Impact on the Price of Oil in the Short-term. *International Journal of Energy Economics and Policy, 9*(2), 267.

Grzybek, G., Greluk, M., Tarach, K., Pyra, K., Słowik, G., Rotko, M., and Góra-Marek, K. (2020). Bioethanol steam reforming over cobalt-containing USY and ZSM-5 commercial zeolite catalysts. *Frontiers in Materials, 7*, 597528.

Gunawan, T., Wijiyanti, R., and Widiastuti, N. (2018). Adsorption–desorption of CO_2 on zeolite-Y-templated carbon at various temperatures. *RSC Advances, 8*(72), 41594-41602.

Haga, F., Nakajima, T., Miya, H., and Mishima, S. (1997). Catalytic properties of supported cobalt catalysts for steam reforming of ethanol. *Catalysis Letters, 48*, 223-227.

Haryanto, A., Fernando, S., Murali, N., and Adhikari, S. (2005). Current status of hydrogen production techniques by steam reforming of ethanol: a review. *Energy & Fuels, 19*(5), 2098-2106.

Highfield, J., Geiger, F., Uenala, E., and Schucan, T. (1994). *Hydrogen Release by Steam-Reforming of Ethanol for Efficient & Clean Fuel Applications.* Paper presented at the Proceedings of the 10th World Hydrogen Energy Conference, Cocoa Beach, FL, USA.

Hou, T., Zhang, S., Chen, Y., Wang, D., and Cai, W. (2015). Hydrogen production from ethanol reforming: Catalysts and reaction mechanism. *Renewable and Sustainable Energy Reviews, 44*, 132-148.

Hui, K. S., Chao, C. Y. H., and Kot, S. C. (2005). Removal of mixed heavy metal ions in wastewater by zeolite 4A and residual products from recycled coal fly ash. *Journal of Hazardous Materials, 127*(1-3), 89-101.

Hunt, J. D., Nascimento, A., Nascimento, N., Vieira, L. W., and Romero, O. J. (2022). Possible pathways for oil and gas companies in a sustainable future: From the perspective of a hydrogen economy. *Renewable and Sustainable Energy Reviews, 160*, 112291.

Ibarrola Rivas, M. J., and Nonhebel, S. (2016). Assessing changes in availability of land and water for food (1960–2050) An analysis linking food demand and available resources. *Outlook on Agriculture, 45*(2), 124-131.

Inokawa, H., Nishimoto, S., Kameshima, Y., and Miyake, M. (2011). Promotion of H_2 production from ethanol steam reforming by zeolite basicity. *International Journal of Hydrogen Energy, 36*(23), 15195-15202.

Jha, V. K., Matsuda, M., and Miyake, M. (2008). Sorption properties of the activated carbon-zeolite composite prepared from coal fly ash for Ni^{2+}, Cu^{2+}, Cd^{2+} and Pb^{2+}. *Journal of Hazardous Materials, 160*(1), 148-153.

Johnsson, F., Kjärstad, J., and Rootzén, J. (2019). The threat to climate change mitigation posed by the abundance of fossil fuels. *Climate Policy, 19*(2), 258-274.

Jones, S. D., and Hagelin-Weaver, H. E. (2009). Steam reforming of methanol over CeO_2- and ZrO_2-promoted Cu-ZnO catalysts supported on nanoparticle Al_2O_3. *Applied Catalysis B: Environmental, 90*(1-2), 195-204.

Kaduk, J. A., and Faber, J. (1995). Crystal structure of zeolite Y as a function of ion exchange. *Rigaku J, 12*(2), 14-34.

Kalamaras, C. M., and Efstathiou, A. M. (2013). *Hydrogen production technologies: current state and future developments.* Paper presented at the Conference papers in science.

Khanchi, M., Mousavian, S. M. A., and Soltanali, S. (2022). Methanol steam reforming over Cu supported on SiO_2, amorphous SiO_2-Al_2O_3, and Al_2O_3 catalysts: Influence of support nature. *International Journal of Energy Research, 46*(3), 3057-3071.

Krstić, V. (2021). Role of zeolite adsorbent in water treatment. *In Handbook of Nanomaterials for Wastewater Treatment,* (pp. 417-481). Elsevier.

Krstić, V., Urošević, T. and Pešovski, B. (2018). A review on adsorbents for treatment of water and wastewaters containing copper ions. *Chemical Engineering Science, 192*, 273-287.

Kurniawan, T. A., Chan, G. Y., Lo, W. H., and Babel, S. (2006). Comparisons of low-cost adsorbents for treating wastewaters laden with heavy metals. *Science of the total Environment, 366*(2-3), 409-426.

Liu, W., Singh, R. P., Jothivel, S., and Fu, D. (2020). Evaluation of groundwater hardness removal using activated clinoptilolite. *Environmental Science and Pollution Research, 27*, 17541-17549.

Llorca, J., Homs, N., Sales, J., and de la Piscina, P. R. (2002). Efficient production of hydrogen over supported cobalt catalysts from ethanol steam reforming. *Journal of Catalysis, 209*(2), 306-317.

Ma, J., Si, C., Li, Y., and Li, R. (2012). (2012). CO_2 adsorption on zeolite X/activated carbon composites. *Adsorption, 18*, 503-510.

Malamis, S., and Katsou, E. (2013). A review on zinc and nickel adsorption on natural and modified zeolite, bentonite and vermiculite: examination of process parameters, kinetics and isotherms. *Journal of Hazardous Materials, 252*, 428-461.

Matsumura, Y., and Ishibe, H. (2009). Suppression of CO by-production in steam reforming of methanol by addition of zinc oxide to silica-supported copper catalyst. *Journal of Catalysis, 268*(2), 282-289.

Mattos, L. V., Jacobs, G., Davis, B. H., and Noronha, F. B. (2012). Production of hydrogen from ethanol: review of reaction mechanism and catalyst deactivation. *Chemical reviews, 112*(7), 4094-4123.

Mintova, S. (2016). *Verified syntheses of zeolitic materials*: Synthesis Commission of the International Zeolite Association.

Muhamad, N., Abdullah, N., Rahman, M. A., Abas, K. H., Aziz, A. A., Othman, M. H. D., ..., and Ismail, A. F. (2018). Removal of nickel from aqueous solution using supported zeolite-Y hollow fiber membranes. *Environmental Science and Pollution Research, 25*, 19054-19064.

Nanda, S., Rana, R., Zheng, Y., Kozinski, J. A., and Dalai, A. K. (2017). Insights on pathways for hydrogen generation from ethanol. *Sustainable Energy & Fuels, 1*(6), 1232-1245.

Ni, M., Leung, D. Y., Leung, M. K., and Sumathy, K. J. F. P. T. (2006). An overview of hydrogen production from biomass. *Fuel Processing Technology, 87*(5), 461-472.

Ogo, S., and Sekine, Y. (2020). Recent progress in ethanol steam reforming using non-noble transition metal catalysts: A review. *Fuel Processing Technology, 199*, 106238.

Ogo, S., Shimizu, T., Nakazawa, Y., Mukawa, K., Mukai, D., and Sekine, Y. (2015). Steam reforming of ethanol over K promoted Co catalyst. *Applied Catalysis A: General, 495*, 30-38.

Oh, T. H. (2010). Carbon capture and storage potential in coal-fired plant in Malaysia—A review. *Renewable and Sustainable Energy Reviews, 14*(9), 2697-2709.

Pareek, A., Dom, R., Gupta, J., Chandran, J., Adepu, V., and Borse, P. H. (2020). Insights into renewable hydrogen energy: Recent advances and prospects. *Materials Science for Energy Technologies, 3*, 319-327.

Prasad, M., Xu, H. Y., and Saxena, S. (2008). Multi-component sorption of Pb (II), Cu (II) and Zn (II) onto low-cost mineral adsorbent. *Journal of Hazardous materials, 154*(1-3), 221-229.

Riani, P., Garbarino, G., Cavattoni, T., and Busca, G. (2021). CO_2 hydrogenation and ethanol steam reforming over Co/SiO_2 catalysts: Deactivation and selectivity switches. *Catalysis Today, 365*, 122-131.

Rosen, M. A., and Koohi-Fayegh, S. (2016). The prospects for hydrogen as an energy carrier: an overview of hydrogen energy and hydrogen energy systems. *Energy, Ecology and Environment, 1*, 10-29.

Rostami, M., Mofarahi, M., Karimzadeh, R., and Abedi, D. (2016). Preparation and characterization of activated carbon–zeolite composite for gas adsorption separation of CO_2/N_2 system. *Journal of Chemical & Engineering Data, 61*(7), 2638-2646.

Sekine, Y., Nakazawa, Y., Oyama, K., Shimizu, T., and Ogo, S. (2014). Effect of small amount of Fe addition on ethanol steam reforming over Co/Al_2O_3 catalyst. *Applied Catalysis A: General, 472*, 113-122.

Sharma, Y. C., Kumar, A., Prasad, R., and Upadhyay, S. N. (2017). Ethanol steam reforming for hydrogen production: Latest and effective catalyst modification strategies to minimize carbonaceous deactivation. *Renewable and Sustainable Energy Reviews, 74*, 89-103.

Trimm, D. L. (1999). Catalysts for the control of coking during steam reforming. *Catalysis Today, 49*(1-3), 3-10.

Tseng, H. H., Zhuang, G. L., Lin, M. D., Chang, S. H., and Wey, M. Y. (2015). The influence of matrix structure and thermal annealing-hydrophobic layer on the performance and durability of carbon molecular sieving membrane during physical aging. *Journal of Membrane Science, 495*, 294-304.

Tseng, R. L., Wu, F. C., and Juang, R. S. (2015). Adsorption of CO_2 at atmospheric pressure on activated carbons prepared from melamine-modified phenol–formaldehyde resins. *Separation and Purification Technology, 140*, 53-60.

Venkatesan, G., Senthilnathan, U., and Rajam, S. (2014). Cadmium removal from aqueous solutions using hybrid eucalyptus wood based activated carbon: adsorption batch studies. *Clean Technologies and Environmental Policy, 16*, 195-200.

Vizcaíno, A. J., Carrero, A., and Calles, J. A. (2007). Hydrogen production by ethanol steam reforming over Cu–Ni supported catalysts. *International Journal of Hydrogen Energy, 32*(10-11), 1450-1461.

Wang, L., Rao, L., Xia, B., Wang, L., Yue, L., Liang, Y., ..., and Hu, X. (2018). Highly efficient CO_2 adsorption by nitrogen-doped porous carbons synthesized with low-temperature sodium amide activation. *Carbon, 130*, 31-40.

Wang, S., He, B., Tian, R., Wu, X., An, X., Liu, Y., ..., and Xie, X. (2020). Novel core-shell-like Ni-supported hierarchical beta zeolite catalysts on bioethanol steam reforming. *International Journal of Hydrogen Energy, 45*(33), 16409-16420.

Wen, J., Dong, H., and Zeng, G. (2018). Application of zeolite in removing salinity/sodicity from wastewater: A review of mechanisms, challenges and opportunities. *Journal of Cleaner Production, 197*, 1435-1446.

Yang, J., Yue, L., Lin, B., Wang, L., Zhao, Y., Lin, Y., ..., and Hu, X. (2017). CO_2 Adsorption of nitrogen-doped carbons prepared from nitric acid preoxidized petroleum coke. *Energy & Fuels, 31*(10), 11060-11068.

Yu, C. H., Huang, C. H., and Tan, C. S. (2012). A review of CO_2 capture by absorption and adsorption. *Aerosol and Air Quality Research, 12*(5), 745-769.

Zanchet, D., Santos, J. B. O., Damyanova, S., Gallo, J. M. R., and Bueno, J. M. C. (2015). Toward understanding metal-catalyzed ethanol reforming. *ACS Catalysis, 5*(6), 3841-3863.

Zhang, L., Pham, T. N., Faria, J., and Resasco, D. E. (2015). Improving the selectivity to C4 products in the aldol condensation of acetaldehyde in ethanol over faujasite zeolites. *Applied Catalysis A: General, 504*, 119-129.

CHAPTER III

SYNTHESIS OF WELL-DISPERSED ZEOLITE NAY IN BAMBOO WOOD

3.1 Abstract

Dispersing zeolite particles on supporting substrates has the capability to mitigate challenges related to particle aggregation and separation. This study showcases how bamboo wood can be employed as a substrate to aid in the crystallization process of zeolite NaY. Acid pretreatment of wood was performed to study the effect of chemical components on zeolite formation. The structure, particle distribution, and morphology of bare wood and their composites were extensively investigated by X-ray diffraction, X-ray tomography, scanning electron microscopy, thermogravimetric analysis, nitrogen sorption analysis, and X-ray photoelectron spectroscopy. The composite of NaY on acid-refluxed wood is effective as an adsorbent of Ni(II) ions in an aqueous solution, providing a similar capacity per weight of adsorbent to a pellet of NaY powder.

3.2 Introduction

Zeolites have been widely utilized in research and industry as catalysts, adsorbents and ion exchangers (Flanigen, 1991). Commercial zeolites are available in the form of powder or formulated to a desired particle size and shape, such as spheres or rods. Some of the disadvantages of using zeolite powder, especially in a liquid medium, include difficulties in separation and mass transfer limitation in agglomerated or large particles sizes. One approach to solve the issues is to disperse zeolite on a support.

Zeolite could be dispersed on plant fibers. Valtchev et al. (1994) coated zeolite A on sheets of vegetal fibers with different amount of lignin and cellulose (Valtchev et al., 1994). They suggested that hydroxide ions in the aluminosilicate gel break hydrogen bonds in cellulose, producing hydroxyl groups that are active for zeolite nucleation. Moreover, lignin content limits the crystallization of zeolite A on the fiber surface (Valtchev et al., 1994). Chemical treatment is, therefore, necessary to achieve the zeolite dispersion on the plant fibers.

Recently, Krukkratoke et al. (2022) synthesized zeolite NaY in Lead tree wood by mixing the wood with the zeolite gel before hydrothermal treatment. NaY was formed in the acid-refluxed wood, whereas NaP was produced in the untreated wood. The composition and morphology could influence the formation of zeolite. Thus, this work aims to investigate zeolite synthesis in bamboo wood with different compositions and structures from Lead tree wood.

Bamboo wood is abundant in tropical and subtropical countries. Bamboo cells are short and porous. The cellular fibrous structure of bamboo has large macropores ranging from around 100 μm from vessels, between 10 to 50 μm from phloem and about 5 μm triangular pores (Chen et al., 2018). Such morphology could make it a good support to disperse zeolite NaY.

The goal of this work is to prepare a composite consisting of zeolite NaY dispersed inside bamboo wood with and without acid treatment. The composites are investigated by X-ray tomographic microscopy (XTM), scanning electron microscopy (SEM), and X-ray photoelectron spectroscopy (XPS) to determine the porosity, zeolite distribution, and interactions between zeolite and bamboo wood. Finally, the wood-zeolite composite is utilized as an adsorbent to remove nickel ions from aqueous solutions.

3.3 Experimental

3.3.1 Pretreatment of bamboo wood

Bamboo culms were peeled, and the wood was cut into small cylindrical pellets with dimensions of 5 mm x 5 mm (diameter x height). The wood pellets were ultrasonically cleaned with DI water and dried at 90°C for 24 h to obtain bare wood (W). Subsequently, the pellets were treated with 67 ml of 3 M HCl solution at 90°C for 6 h, separated, washed, and dried at 90°C overnight to obtain acid-refluxed wood (RW).

3.3.2 Synthesis of wood-zeolite composite

The wood-zeolite composites were synthesized by adding a feed gel to a mixture of seed gel of zeolite NaY containing pellets of W or RW. The synthesis steps are summarized in Scheme 3.1. The composition of the seed and feed gels were modified from the literature (Ginter et al., 1992). The mixture of a seed gel and wood was prepared by immersing 1.00 g of wood (W or RW) in a solution consisting of 1.00 g of NaOH and 10.00 g of DI water for 24 h and adding 0.418 g of anhydrous $NaAlO_2$ under magnetic stirring. Then, 4.79 g of Na_2SiO_3 solution was slowly dropped (40 drops/min) into the mixture. The mixture was stirred for 30 min and aged for 24 h.

To prepare the feed gel, 2.78 g of $NaAlO_2$ were dissolved in a solution containing 0.035 g of NaOH and 22.3 g of DI water. Next, 30.19 g of Na_2SiO_3 silicate solution was slowly added to the sodium aluminate solution, stirring at a rate of 60 drops/min, for 30 min. The obtained feed gel was then added to the wood-containing seed gel and stirred continuously for 30 min. The resultant mixture was aged for 24 h at room temperature without stirring, and then heated at 90°C for 24 h. After cooling down, the solid products, including the wood-zeolite composite and zeolite powder, were separated, repeatedly washed with DI water using sonication until the pH of the washing water was approximately 8, and dried at 100°C overnight. The obtained pellets were named untreated wood-zeolite composite (WZ) and refluxed wood-zeolite composite (RWZ).
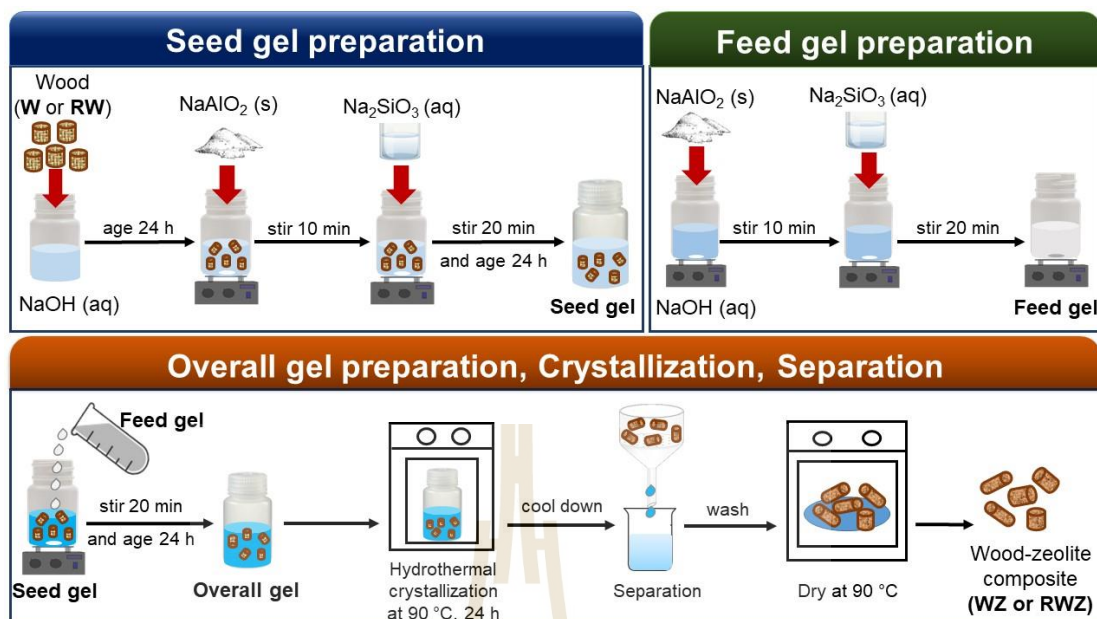
Scheme 3.1 Steps in the synthesis of wood-zeolite composites.

3.3.3 Characterization methods

Phases of bamboo wood and the wood-zeolite composite were studied by X-ray diffraction (XRD, Bruker D8 ADVANCE) with a Cu Kα radiation (λ = 1.5406 Å) operated at 40 kV of voltage and 30 mA of current with a step size of 0.02° and speed of 0.4 s/step. Three dimensional (3D) structure of samples was investigated by Synchrotron radiation X-ray tomographic microscopy (XTM) technique at Beamline 1.2W, Synchrotron Light Research Institute (SLRI). X-ray projections of the samples were collected for 180 degrees with 0.1 angular increments to form a dataset. Polychromatic X-rays were attenuated with 200 micron-thick aluminum foil, with a mean energy of about 10 keV, in order to minimize the artifacts. The X-ray projections were collected on the sCMOS camera with a pixel size of 1.44 micrometers. The data were pre-processed and reconstructed in three dimensions based on a filtered-back projection algorithm using Octopus Reconstruction software. To identify and classify the distribution of zeolite on untreated and refluxed woods and the porosity of both wood-zeolite composites, the Octopus Software was used by comparing each voxel to all the surrounding voxels. Finally, a 3D reconstructed image of the tomographic volumes of the composite was visualized using Drishti software (Desrues et al., 2010; Limaye, 2012).

The morphology of the samples was obtained by a field emission scanning electron microscope (FE-SEM, JEOL JSM 7800F). The wood pellet was spread on a layer of silver paint adhered to a metal stub and coated with gold under an argon

atmosphere. Elemental analysis was performed using energy-dispersive X-ray spectroscopy (EDS). The surface elements of the wood-zeolite composites were analyzed by X-ray photoelectron spectroscopy (XPS) on a PHI 5000 VersaProbe II XPS system (ULVAC-PHI, Japan) with Al Kα radiation as the excitation source. The binding energies were calibrated by using the C 1s peak (284.8 eV).

The thermal degradation of wood and wood-zeolite composite was determined by thermogravimetric analysis (TGA, Mettler Toledo model TGA/DSC1). About 5-20 mg of each sample in an alumina pan was heated to 800°C with 10°C/min under an air flow of 50 mL/min. Textural property of samples was determined by N_2-sorption at -196°C on a Belsorp mini II instrument. All samples were degassed at 70°C under a vacuum for 24 h. The surface area was calculated according to the Brunauer-Emmett-Teller (BET) method.

3.3.4 Adsorption experiment

The adsorption efficiency of the wood-zeolite composites was evaluated in Ni^{2+} solutions. To compare the adsorption capacity of wood-zeolite composite, zeolite NaY was synthesized with a similar condition, without wood addition. The zeolite pellet (diameter = 5 mm) was prepared by pressing the powder with 1-ton hydraulic pressure. In the adsorption study, 20 mL of 100 ppm Ni^{2+} solution with one pellet of an adsorbent was stirred for 3 h at room temperature in a PP bottle. Then the adsorbent was separated from the adsorbate. After that, the solution was diluted with DI water and the Ni^{2+} concentration was determined by flame atomic absorption spectrophotometry (PerkinElmer, PinAAcle 900F). The adsorption capacity of Ni^{2+} at equilibrium (q_e, mg/g) is calculated from equation (1).

$$q_e = \frac{(C_0 - C_e) \times V}{m} \tag{1}$$

where C_0 (mg/L) and C_e (mg/L) are the initial and equilibrium concentration, V (L) is the volume of the solution, and m (g) is the adsorbent weight.

3.4 Results and discussion

3.4.1 Physical properties of wood-zeolite composites

Figure 3.1 shows the XRD pattern of untreated wood-zeolite composite (WZ) and refluxed wood-zeolite composite (RWZ). The results confirm that the synthesis of the wood-zeolite composite was successful. NaY zeolite is mainly obtained comfirming by the observation of characteristic peaks of faujasite structure (symbol ♦) and a Si/Al ratio about 2, as determined by EDS (Table 3.1) (Ginter et al., 1992; Köroğlu

et al., 2002) Zeolite NaP also exists as a minor phase (symbol o) (Ree, 1993). Regarding the relative diffraction intensities of the two structures, zeolite NaY has a higher content in RWZ than in WZ. Depending on the wood's chemical structure, untreated wood may have a higher number of carboxylic acid and hydroxyl groups, as suggested by XPS spectra of C 1s and O 1s (shown in Table S1), which can trap Na^+ ions or water molecules from the initial gel composition (Rowell, 2021; Barman et al., 2020). This behavior has the potential to interfere with the suitable gel ratio during zeolite NaY formation and create zeolite NaP, which requires a higher Na^+ content (Pal et al., 2013). This result is consistent with the previous work that refluxed Lead tree wood yielded primarily zeolite NaY, whereas non-refluxed wood mainly produced zeolite NaP (Krukkratoke et al., 2022). Furthermore, the presence of broad peaks at 14.1° and 22.4° indicates that the cellulose structure maintained a strong base during the hydrothermal process (Jin et al., 2015).
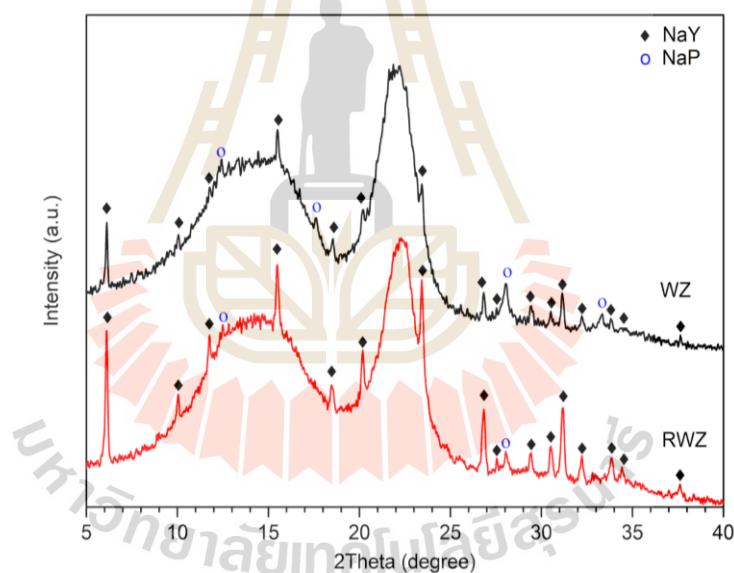
Figure 3.1 XRD patterns of untreated wood-zeolite composite (WZ) and refluxed wood-zeolite composite (RWZ).

Figure 3.2 shows photographs and SEM images of WZ. Figure 3.2a shows the outer part of the wood after hydrothermal treatment. The SEM image (Figure 3.2b) shows particles randomly distributed among the wood fibers, the majority of isolated particles. The image with a higher magnification of the framed area (Figure 3.2c) shows that the particles are polycrystals with a diameter of about 5 μm. Figure 3.3d shows the inner part picture of the dissected wood. The SEM images (Figures 3.2e-f) also show zeolite crystals of a similar size randomly adhering to the walls of the phloem and xylem. The number of zeolite crystals per wood area on the outer part is significantly more than on the inner part.
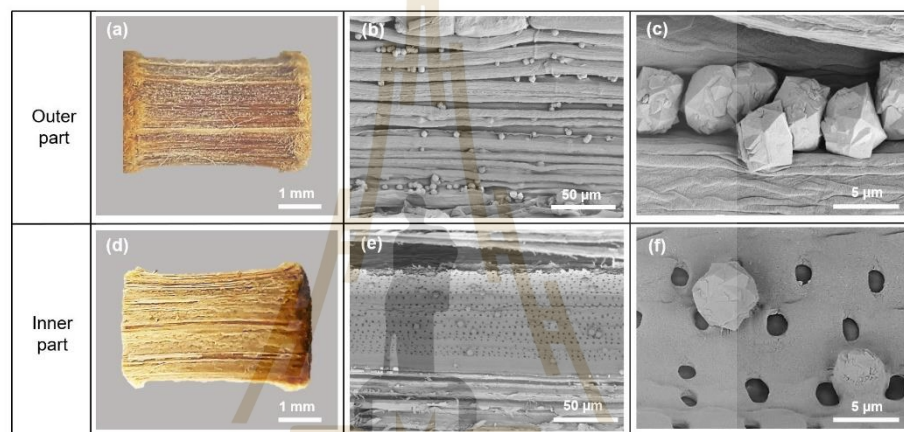
Figure 3.2 (a, d) photographs and (b, c, e, f) SEM images of untreated wood-zeolite composite (WZ) from outside and inside (dissected).

Figure 3.3 shows photographs and SEM images of RWZ from both the outer and inner parts. The SEM image of the outer part (Figure 3.3b-c) shows more zeolite crystals than that of WZ. Refluxing removes hemicellulose and lignin content (Shi et al., 2018), allowing the zeolite gel to interact better with the wood. The improved interaction could contribute to a higher number of crystals. The SEM images of the inner part (Figure 3.3e-f) show zeolite crystals of various sizes, which are smaller than the crystals on the outer part. The number of zeolite crystals on the outer part of RWZ is also significantly higher than on the inner part. Since the zeolite gel has a good interaction with the wood's outer part, zeolite formation is favorable on the outer part rather than the inner part.
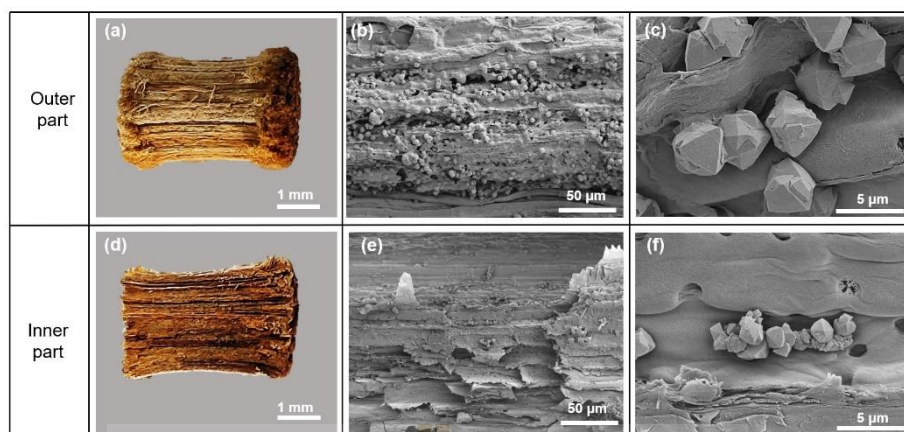
Figure 3.3 (a, d) photographs and (b, c, e, f) SEM images of refluxed wood-zeolite composite (RWZ) from outside and inside (dissected).

Basically, zeolite NaY only loses its absorbed water below 200°C (Ribeiro et al., 2020) while the thermal combustion of wood can be classified into three main parts consisting of hemicellulose (225–325°C), cellulose (305–375°C), and lignin (250-600°C) (Shafizadeh, 1985). Therefore, the calculation of zeolite contents was based on the TGA results of W and WR (Figure A.1), which showed that all hydrocarbon compounds are completely burnt out by combustion above 800°C (Barzegar et al., 2020). Figure 3.4a shows that both WZ and RWZ samples exhibit two primary weight loss steps due to the combustion of hemicellulose and cellulose, similar to the results found in various types of wood (Shen et al., 2009). The percentage of zeolite in WZ and RWZ is 5% and 20% by weight, respectively. This higher zeolite content in RWZ is consistent with previous findings by Valchev et al. (1994), who suggest that higher cellulose content in the wood could lead to higher zeolite content. The cellulose content in the RW substrate is higher than in the W substrate, as determined by the thermal decomposition range of 305-375°C and the oxidative carbon species from XPS results (Table A.2) (Shen et al., 2009; Yu et al., 2022). Furthermore, the 3D structures of WZ and RWZ from XTM suggest that the RWZ sample has a higher zeolite content, as indicated by the higher relative density area compared to WZ as shown in Figure A.2. Figure 3.4b displays the N_2 adsorption-desorption isotherms of the composites, which exhibit two types of isotherms. The first is isotherm type I, characteristic of microporous materials from zeolite NaY (Thommes et al., 2015). The second is isotherm type II, characteristic of macroporous materials from wood (Wang et al., 2019). Due to its higher zeolite content, RWZ exhibits higher nitrogen uptake at low relative pressure ($P/P_0 < 0.05$) compared to WZ. At a relative pressure close to 1, the adsorption isotherms of both composites become almost parallel to the y-axis and do not

plateau, indicating that adsorption has not yet reached saturation. This suggests that a certain amount of macropores is present in the wood substrates. The BET surface area per gram of composite for WZ and RWZ is 5 m^2/g and 45 m^2/g, respectively. Therefore, the surface area increases with zeolite content.
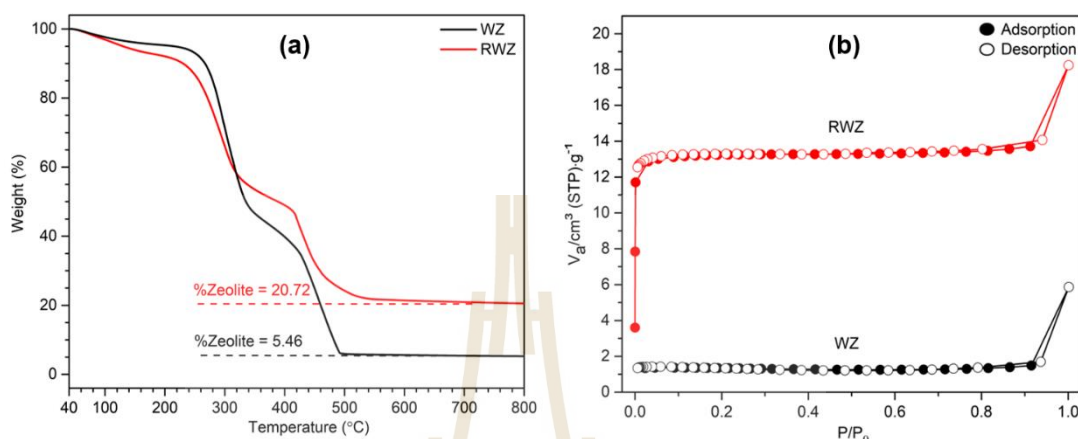

Figure 3.4 (a) TGA profiles and (b) N_2-isotherm of untreated wood-zeolite composite (WZ) and refluxed wood-zeolite composite (RWZ).

From all characterization techniques, wood-zeolite composites could be synthesized by mixing wood in the NaY synthesis gel. RWZ has a significantly higher number of zeolite NaY than that of WZ. The difference in zeolite phases and content would depend on the structural components of wood substrates.

3.4.2 Chemical properties of wood-zeolite composites

Figure 3.5a shows the XPS spectra in a wide-range scanning of RW and RWZ compared with synthesized zeolite (ZY). ZY shows peaks corresponding to the zeolite composition, including Si and Al. The peaks from RWZ have lower intensity while those from WZ are nearly invisible (Figure A.3), which is consistent with the zeolite fraction from the previous section. The chemical state of composites would be further elaborated from each binding energy.

C1s spectra and their relative peak-fitted area of RW and RWZ are shown in Figure 3.5b and Table 3.1 displays the peaks of C1s from RW and RWZ. The C1s spectra are deconvoluted into four peaks corresponding to $C1_{(C*-C/C*=C)}$, $C2_{(H-C*-O)}$, $C3_{(H-C*=O/O-C*-O)}$ and $C4_{(O=C*-O)}$ (Sun et al., 2020). The oxygenated carbon (C2, C3, and C4) species in RWZ are increased suggesting that the wood components are oxidized during the synthesis of wood-zeolite. This phenomenon is consistent with several studies that have reported a significant increase in the portion of oxygenated carbon in wood after treatment with alkali media (Razaina et al., 2016; Reale Batista and Drzal, 2021).

Furthermore, the binding energy of the carboxyl group (C4$_{(O=C*-O)}$) is significantly shifted to a lower value about 0.5 eV. A few reports suggest that carboxylate anion interacted with calcium or uranium ions drove the binding energy of C4$_{(O=C*-O)}$ to lower energy by electrostatic force (Falsafi et al., 2014; Velasco et al., 2019). Similar results were obtained for WZ compared to W (Figure A.4). The observed shift suggests that the carboxyl group of wood substrates in the composites may interact with sodium ions in this work. Consistent with the Na1s spectra, about 1072 eV corresponds to the R-COO-Na complex, which is displayed together with Na-O on the zeolite framework (1073 eV) (Yang et al., 2021; Ibrahim et al., 2023). Figure A.3 shows the O1s spectra, which display two oxygen species separately from 529.0 to 536.5 eV in wood (Sun et al., 2020; Razaina et al., 2016) and from 529.0 to 537.0 eV in zeolite (Merlen et al., 1990). However, due to the overlap, it is difficult to clearly evaluate each oxygen species in the composites.

Table 3.1 Si/Al ratio and peak-fitted C 1s of composites.

	WZ	RWZ
EDS		
Si/Al ratio*	2.08±0.06	2.13±0.13
XPS C1s		
C1$_{(C*-C/C*=C)}$	20.67	33.30
C2$_{(H-C*-O)}$	15.25	30.04
C3$_{(H-C*=O/O-C*-O)}$	46.83	24.93
C4$_{(O=C*-O)}$	17.25	11.73

*Note that the elemental analysis was determined by SEM-EDS by randomly selecting 9 areas on the zeolite particles.
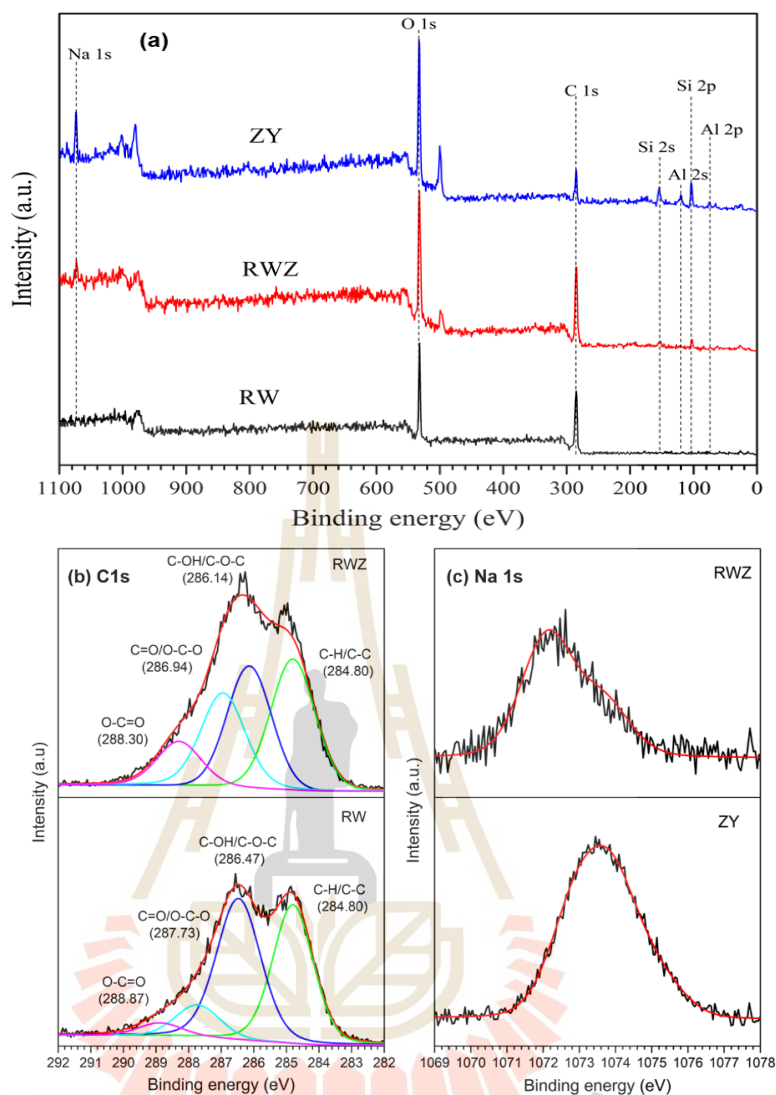
Figure 3.5 XPS spectra of full spectra (a), C1s (b), and Na 1s (c) of synthesized zeolite (ZY), treated wood (RW), and wood-zeolite composite (RWZ).

Zeolite is commonly used as a cation-exchange adsorbent due to the low Si/Al ratio that represents to rich Na ion surrounding on zeolite surface. According to the dominant properties of wood-zeolite composites mentioned above, it would be beneficial in terms of simple separation for metal ions removal, such as Ni (II) ion from an aqueous phase (Malamis and Katsou, 2013). As a result, Ni adsorption in the composites is further investigated in this work.

3.4.3 Adsorption study

Table 3.2 shows the values of Ni^{2+} adsorption capacity per gram of adsorbent including untreated (W) and refluxed wood (RW), untreated and refluxed wood-zeolite composites (WZ and RWZ), and zeolite pellets (ZY). W and RW did not adsorb, whereas WZ adsorbed with the capacity of about half of RWZ. The RWZ has a

higher capacity than ZY despite the different zeolite content. The adsorption on both WZ and RWZ has high deviation because each adsorption experiment was performed with only one wood pellet and each pellet probably has different zeolite content. The adsorption results confirm that the dispersion of zeolite NaY in refluxed wood significantly improves the adsorption of Ni^{2+}.

The amount of Ni removed is increased by incorporating zeolite in wood compared to bare wood. The Na ions in the zeolite composites could likely exchange with Ni ions. The adsorption capacities follow the order of W < RW < WZ < ZY < RWZ, corresponding to the number of zeolites and surface areas (Table 3.2). This result is related to the characteristics of the wood-zeolite composite and confirms our goal of achieving high zeolite content in bamboo wood through acid treatment. Additionally, the highest adsorption capacity was observed for the RWZ composite due to the good dispersion and high internal surface area of zeolite on treated wood, promoting mass transfer of guest species (Malamis and Katsou, 2013). In conclusion, the adsorption capacity increases with an increase in the amount of zeolite.

Table 3.2 Ni^{2+} adsorption capacity of wood, wood-zeolite composites and NaY.

Sample	Adsorption capacity, q_e ($mg_{Ni(II)}/g_{adsorbent}$)
Bare wood (W)	Not adsorbed
Refluxed wood (RW)	Not adsorbed
Wood-zeolite (WZ)	4.90 ± 1.22
Refluxed wood-zeolite (RWZ)	9.51 ± 1.79
NaY (ZY)	8.63 ± 0.88

3.5   Conclusions

Crystals of zeolite NaY were successfully dispersed onto bamboo wood by mixing the wood with zeolite gel and performing crystallization through hydrothermal methods. The zeolite crystals were found to be more dispersed on the outer part of the wood pellets as compared to the inner part. The zeolite content on acid-refluxed wood was significantly higher (20.72 wt%) than that on untreated wood (5.46 wt%). The size of zeolite crystals was around 5 μm and they were well-dispersed on the wood surface without much agglomeration. The interaction between zeolite and wood

occurred through the carboxyl group of wood substrate and sodium ions in zeolite NaY. In aqueous solutions, the zeolite-wood composite was found to be an effective adsorbent for Ni (II) ions. The adsorption capacity of the acid-treated wood composite was found to be double that of untreated wood and similar to that of a NaY pellet. The composite could be easily separated from the solution.

3.6   References

Barman, D. N., Haque, M. A., Hossain, M. M., Paul, S. K., and Yun, H. D. (2020). Deconstruction of pine wood (Pinus sylvestris) recalcitrant structure using alkali treatment for enhancing enzymatic saccharification evaluated by Congo red. *Waste and Biomass Valorization, 11*, 1755-1764.

Barzegar, R., Yozgatligil, A., Olgun, H., and Atimtay, A. T. (2020). TGA and kinetic study of different torrefaction conditions of wood biomass under air and oxy-fuel combustion atmospheres. *Journal of the Energy Institute, 93*(3), 889-898.

Chen, G., Luo, H., Yang, H., Zhang, T., and Li, S. (2018). Water effects on the deformation and fracture behaviors of the multi-scaled cellular fibrous bamboo. *Acta Biomaterialia, 65*, 203-215.

Desrues, J., Viggiani, G., and Besuelle, P. eds. (2010). *Advances in X-ray Tomography for Geomaterials* (Vol. 118): John Wiley and Sons.

Falsafi, A., Mitra, S. B., Oxman, J. D., Ton, T. T., and Bui, H. T. (2014). Mechanisms of setting reactions and interfacial behavior of a nano-filled resin-modified glass ionomer. *Dental Mterials, 30*(6), 632-643.

Flanigen, E. M. (1991). Zeolites and molecular sieves an historical perspective. In *Studies in Surface Science and Catalysis* (Vol. 58, pp. 13-34): Elsevier.

Ginter, D. M., Bell, A. T., Radke, C. J., Occelli, M. L., and Robson, H. E. (1992). Synthesis of Microporous Materials, Molecular Sieves. *Van Nostrand Reinhold, New York, 1*, 6.

brahim, A. H., Lyu, X., and ElDeeb, A. B. (2023). Synthesized Zeolite Based on Egyptian Boiler Ash Residue and Kaolin for the Effective Removal of Heavy Metal Ions from Industrial Wastewater. *Nanomaterials, 13*(6), 1091.

Jin, C., Li, J., Han, S., Wang, J., Yao, Q., and Sun, Q. (2015). Silver mirror reaction as an approach to construct a durable, robust superhydrophobic surface of bamboo timber with high conductivity. *Journal of Alloys and Compounds, 635*, 300-306.

Köroğlu, H. J., Sarıoğlan, A., Tatlıer, M., Erdem-Şenatalar, A., and Savaşçı, Ö. T. (2002). Effects of low-temperature gel aging on the synthesis of zeolite Y at different alkalinities. *Journal of Crystal Growth, 241*(4), 481-488.

Krukkratoke, P., Keawkumay, C., Tayraukham, P., Prompiputtanapon, K., Khemthong, P., Prayoonpokarach, S., and Wittayakun, J. (2022). Strategic Synthesis to Disperse Zeolite NaY in Lead Tree Wood. *Crystals, 12*(4), 504.

Limaye, A. (2012). *Drishti: a volume exploration and presentation tool.* Paper presented at the Developments in X-ray Tomography VIII.

Malamis, S., and Katsou, E. (2013). A review on zinc and nickel adsorption on natural and modified zeolite, bentonite and vermiculite: examination of process parameters, kinetics and isotherms. *Journal of hazardous materials, 252*, 428-461.

Merlen, E., Lynch, J., Bisiaux, M., and Raatz, F. (1990). Surface modifications during Y zeolite dealumination. *Surface and Interface Analysis, 16*(1‐12), 364-368.

Pal, P., Das, J. K., Das, N., and Bandyopadhyay, S. (2013). Synthesis of NaP zeolite at room temperature and short crystallization time by sonochemical method. *Ultrasonics Sonochemistry, 20*(1), 314-321.

Razaina, M. T., Ariawan, D., and Mohd Ishak, Z. A. (2016). *Surface Characterization of Alkali Treated Kenaf Fibers by XPS and AFM.* Paper presented at the Key Engineering Materials.

Reale Batista, M. D., and Drzal, L. T. (2021). Surface modification of bamboo fiber with sodium hydroxide and graphene oxide in epoxy composites. *Polymer Composites, 42*(3), 1135-1147.

Rees, L. V., and Chandrasekhar, S. (1993). Hydrothermal reaction of kaolinite in presence offluoride ions at pH< 10. *Zeolites, 13*(7), 534-541.

Ribeiro, S. P. D. S., Martins, R. C., Barbosa, G. M., Rocha, M. A. D. F., Landesmann, A., Nascimento, M. A. C., and Nascimento, R. S. V. (2020). Influence of the zeolite acidity on its synergistic action with a flame-retarding polymeric intumescent formulation. *Journal of Materials Science, 55*(2), 619-630.

Rowell, R. M. (2021). Understanding wood surface chemistry and approaches to modification: a review. *Polymers, 13*(15), 2558.

Shafizadeh, F. (1985). Pyrolytic reactions and products of biomass. *Fundamentals of Thermochemical Biomass Conversion*, 183-217.

Shen, D. K., Gu, S., Luo, K. H., Bridgwater, A. V., and Fang, M. X. (2009). Kinetic study on thermal decomposition of woods in oxidative environment. *Fuel, 88*(6), 1024-1030.

Shi, J., Lu, Y., Zhang, Y., Cai, L., and Shi, S. Q. (2018). Effect of thermal treatment with water, H_2SO_4 and NaOH aqueous solution on color, cell wall and chemical structure of poplar wood. *Scientific Reports, 8*(1), 17735.

Sun, H., Yang, Y., Han, Y., Tian, M., Li, B., Han, L., ..., and He, Y. (2020). X-ray photoelectron spectroscopy analysis of wood degradation in old architecture. *BioResources, 15*(3), 6332-6343.

Thommes, M., Kaneko, K., Neimark, A. V., Olivier, J. P., Rodriguez-Reinoso, F., Rouquerol, J., and Sing, K. S. (2015). Physisorption of gases, with special reference to the evaluation of surface area and pore size distribution (IUPAC Technical Report). *Pure and Applied Chemistry, 87*(9-10), 1051-1069.

Valtchev, V., Mintova, S., Vulchev, I., and Lazarova, V. (1994). Influence of reactive radicals in cellulose fibres on the formation of zeolite coatings. *Journal of the Chemical Society, Chemical Communications*(18), 2087-2088.

Velasco, C. A., Artyushkova, K., Ali, A. M. S., Osburn, C. L., Gonzalez-Estrella, J., Lezama-Pacheco, J. S., ..., and Cerrato, J. M. (2019). Organic functional group chemistry in mineralized deposits containing U (IV) and U (VI) from the Jackpile Mine in New Mexico. *Environmental science & technology, 53*(10), 5758-5767.

Wang, Q., Chang, S., Tan, Y., and Hu, J. (2019). Mesopore structure in Camellia Oleifera shell. *Protoplasma, 256*, 1145-1151.

CHAPTER IV

FACILE PREPARATION OF MICRON- AND NANO-SIZED NAY ON BAMBOO WOOD FOR CO_2 ADSORPTION

4.1   Abstract

Nano-scale zeolite powders offer numerous advantages, such as more guest species capacity and large surface area. However, their handling presents challenges due to safety concerns and the high cost of synthesis templates. A previous study successfully synthesized a composite of zeolite dispersed on porous carbon substrates like bamboo wood to address these issues, but the particle size of zeolite NaY remained in the micron scale. This study aimed to reduce the particle size to the nanoscale while maintaining its pellet form by investigating the impact of base concentration in the seed gel through a one-step hydrothermal method. The synthesized nano-sized zeolite NaY on bamboo wood was then examined for carbon dioxide (CO_2) adsorption. Characterization using SEM, TGA, and N_2 adsorption-desorption measurements confirmed the successful preparation of nano-sized zeolite NaY on the wood surface by adjusting the water content in the seed gel. The SEM analysis showed the non-agglomeration of zeolite and the presence of a mesoporous structure, while the N_2-sorption isotherm indicated a mixed microporous and mesoporous character. The zeolite composites with smaller particle sizes and a mixed porous structure exhibited significantly higher CO_2 adsorption capacity than previous samples. The Nano/RWZ-C pellets substantially increased CO_2 adsorption capacity, outperforming the Nano/ZY-C sample. This improvement can be attributed to the small particle size of zeolite NaY, interconnected micro-meso channels, and the effective dispersion of zeolite under temperature and pressure conditions. Increasing the alkalinity resulted in a reduction in the particle size of zeolite on the wood. The zeolite-bamboo wood composite pellet shows promise as an alternative adsorbent for gas adsorption. Future work aims to quantify the percentage of zeolite on the wood based on the volume and type of pores in the wood substrate.

4.2   Introduction

Zeolite, a highly significant class of microporous materials known for its regular and uniform pore structures, has garnered significant attention across diverse industries due to its exceptional molecular sieving properties. Its applications span various fields, including catalysis, adsorption, separation processes, and emerging areas like electronics, magnetism, chemical sensors, and medicine (Auerbach et al., 2003; Pang et al., 2009). The hydrothermal method, involving aging and crystallization stages in an alkaline environment, remains the predominant technique for zeolite synthesis (Pang et al., 2009).

Numerous efforts have been made to modify zeolite properties and enhance its performance. These modifications include cation exchange, dealumination, surface treatments with cationic metal ions or ammonium ions, and acid treatments (Pang et al., 2009). It is widely acknowledged that introducing additional components into the zeolite structure can change its physical properties and adsorption capacity. One common method used for this purpose is the incorporation of carbon atoms into the zeolite structure. Various techniques have been documented in the literature to achieve this objective.

For example, Purnomo (2013) discussed the preparation of carbon-zeolite composites using bagasse fly ash as a raw material. Furthermore, Ma et al. (2012) investigated a carbon-zeolite composite derived from elutrilithe, which contained silica, alumina, and carbon, along with pitch, for efficient CO_2 adsorption. Another study by Gao et al. (2005) focused on the hydrothermal preparation of carbon-zeolite composites using industrial wastes such as coal fly ash and sawdust mixtures, with an emphasis on understanding the influential parameters during the preparation process. Additionally, researchers have explored the utilization of rice husk waste for the production of carbon-zeolite composites, as examined by Katsuki et al. (2005) through conventional and microwave hydrothermal methods. An alternative approach involved the preparation of ZSM-5 particles supported on various types of treated carbon, as conducted by Ozaki et al. (2006). Furthermore, Martinez et al. (2001) synthesized MFI-type zeolites supported on different carbon materials to investigate the influence of carbon surface chemistry on zeolite preparation. Recently, Lakhera et al. (2015) explored the preparation and characterization of carbon-zeolite composites with varying weight percentages of carbon and zeolite using the sol-gel method. In a separate study, Lee et al. (2002) examined multiple adsorbents, including a commercial zeolite-activated carbon composite, for CO_2 adsorption and compared their performance with that of zeolite 13X alone. The zeolite-carbon composite

exhibited high performance for CO_2 adsorption (Rostami et al., 2016). However, the preparation of the composite involved complex steps and took more time, including pretreatment and activation of the carbon source before composite preparation. Additionally, the resulting products were in powder form, which was not convenient and posed difficulties for large-scale or column setup applications, requiring binders to form pellets and leading to increased material costs and energy consumption (Lee et al., 2002; Rostami et al., 2016; Gleichmann et al., 2016).

To overcome these issues, this study aims to prepare pellets of zeolite-carbon composites following the optimal conditions from the previous chapter. However, the particle size of zeolite NaY on treated wood remained relatively large, around 3-4 μm. In the literature, Anbia et al. (2016) proposed that the particle size of zeolite affects CO_2 adsorption. They suggested that nano-sized zeolite particles exhibit higher CO_2 adsorption capacity compared to micron-sized zeolite particles due to enhanced gas diffusion. Thus, to achieve a high adsorption capacity for CO_2, nano-sized zeolite particles are required. However, nano-sized zeolites in the literature are typically in powder form, which poses challenges for handling as adsorbents. Therefore, the goal of our study is to reduce the size of zeolite particles dispersed on treated-wood pellets to address this issue. Recently, Zhao et al. (2021) investigated the effect of alkalinity and water content on the particle size of zeolite FAU. They found that low water content or high alkalinity in the prepared gel of FAU zeolite resulted in nano-sized zeolite particles due to fast crystallization rates. Therefore, in this work, the water content between the seed and feedstock gels of the composites was adjusted to achieve nano-sized zeolite Y particles on the wood pellets. The volume of water in the seed gel was transferred to the feed gel as much as possible to increase the alkalinity in the seed gel. The resulting product from this work will be applied for gas adsorption, particularly for CO_2.

The increasing levels of CO_2 and its significant contribution to global warming have intensified the urgency of its removal (Ma et al., 2012). Adsorption is widely recognized as an effective approach to address this issue (Siriwardane et al., 2003). While various adsorbents have been proposed as suitable candidates for CO_2 capture, continuous efforts are underway to enhance their performance, leading to rapid advancements in composite adsorbents as a promising research field. In this research, pellets of zeolite-activated carbon composites were prepared and applied for CO_2 adsorption studies.

4.3 Experimental

4.3.1 Preparation of treated wood-zeolite composite, zeolite NaY, and treated wood with hydrothermal

In this study, treated wood-zeolite composites were prepared and modified according to the procedures outlined in Chapter III. Bamboo wood was refluxed with a HCl solution to reduce lignin content and eliminate impurities. Regarding the synthesis of the composites, the process closely resembled the methodology described in Chapter III. However, adjustments were made to the water volumes in the seed gel and feedstock gel, as indicated in Table 4.1. These adjustments were made with the aim of achieving a smaller particle size of zeolite NaY within the treated wood, in contrast to the zeolite size reported in Chapter III. The treated wood-zeolite NaY composites were categorized based on the water volume in the seed gel. The composite with a low volume of water in the seed gel was referred to as the nano-size treated wood-zeolite NaY composite (Nano-RWZ). Conversely, the composite prepared under the same conditions as Chapter III, resulting in a zeolite size of approximately 3-4 μm, was termed the micron-size treated wood-zeolite NaY composite (Micron-RWZ).

To confirm the particle size of zeolite within the wood matrix, scanning electron microscopy (SEM) was employed. Additionally, a control carbon sample (refluxed wood, RW) was prepared following a similar composite synthesis procedure, with the exception that no silicon (Si) and aluminum (Al) sources were introduced. After hydrothermal, treated woods were named Micron/RW-HYD and Nano/RW-HYD. The zeolite NaY control samples were synthesized using the methods outlined in Chapter III, but without the presence of wood.

Table 4.1 Gel composite for preparation of RWZ composite.

Composition	Micron condition (Chapter III)	Nano condition
Seed gel	$10.6SiO_2:Al_2O_3:10.3Na_2O:332.2H_2O$	$10.6SiO_2:Al_2O_3:10.3Na_2O:184.7H_2O$
Feedstock gel	$10.0SiO_2:Al_2O_3:4.4Na_2O:158.2H_2O$	$10.1SiO_2:Al_2O_3:4.4Na_2O:179.9H_2O$
Overall gel	$10.1SiO_2:Al_2O_3:5.1Na_2O:180.9H_2O$	$10.2SiO_2:Al_2O_3:5.2Na_2O:180.6H_2O$

Table 4.2 List of sample name before and after carbonization.

The sample before carbonization	Micron condition	Nano condition
Refluxed wood and hydrothermal (RW-HYD)	Micron-RW-HYD	Nano-RW-HYD
Refluxed wood-zeolite composite (RWZ)	Micron-RWZ	Nano-RWZ
Zeolite NaY (ZY)	Micron-ZY	Nano-ZY
The sample after carbonization	Micron condition	Nano condition
Refluxed wood and hydrothermal (RW-HYD)	Micron/RW-HYD-C	Nano/RW-HYD-C
Refluxed wood-zeolite composite (RWZ)	Micron/RWZ-C	Nano/RWZ-C
Zeolite NaY (ZY)	Micron-ZY-C	Nano-ZY-C

4.3.2 The carbonization of wood-zeolite carbon composite

The activation of the RWZ samples was performed through carbonization under an inert atmosphere using a TGA furnace (Netzsch model STA 409 PC Luxx instrument). Initially, 0.2 g of the composite wood, zeolite Y, or RW-HYD wood was placed into the TGA crucible. The samples were then subjected to heating at 120°C for 30 min under a nitrogen (N_2) flow rate of 40 ml/min. Following this step, the composites were carbonized at 700°C for a duration of 2 h. The samples were subsequently allowed to cool down under a nitrogen atmosphere until reaching room temperature.

The carbonization process aimed to avoid the complication between CO_2 desorption and carbon decompose and clean surface of composite. The resulting samples were denoted as the carbonized Nano-RWZ (Nano/RWZ-C) and the carbonized Micron-RWZ (Micron/RWZ-C). Additionally, a control carbon sample that underwent hydrothermal activation following the same procedure as the composites was labeled as carbonized carbon (Micron/RW-C and Nano/RW-C). The parent zeolite NaY was named as Micron/ZY and Nano/ZY.

4.3.3 Characterization methods

For the analysis of sample morphology, a field emission scanning electron microscope (FE-SEM, JEOL JSM 7800F) was utilized. The experimental procedure involved applying a layer of silver paint to a metal stub, onto which the composite pellet was carefully positioned. Subsequently, a thin carbon coating was applied to the sample under an argon atmosphere.

The phases of the zeolite-activated carbon composite were investigated using X-ray diffraction (XRD) on a Philips X'Pert PRO diffractometer. The XRD measurements employed Cu Kα radiation with a wavelength (λ) of 1.5406 Å, operated

at a voltage of 45 kV and a current of 40 mA. The analysis was carried out with a step size of 0.01° and a scanning speed of 0.02 s/step.

Thermal degradation characteristics of both wood and the wood-zeolite composite were evaluated using thermogravimetric analysis (TGA) performed on a Netzsch model STA 409 PC Luxx instrument. Approximately 120-150 mg of each sample was placed in an alumina crucible and subjected to heating at a rate of 10°C/min, starting from room temperature up to 120°C to eliminate moisture. The temperature was then further increased to 700°C. The TGA analysis was conducted under a N_2 atmosphere with a flow rate of 50 mL/min.

The N_2-sorption technique at -196°C on a Belsorp mini II instrument was used to assess the textural properties of the samples before carbonization. Prior to analysis, all samples were subjected to 24 h of vacuum degassing at 70°C. The surface area was determined using the Brunauer-Emmett-Teller (BET) method.

To determine the textural properties of the carbonized samples, N_2-sorption measurements were carried out at -196°C using a Micromeritics ASAP 2020 instrument. Before the analysis, the samples were subjected to degassing at 300°C and <13 μbar for 1 h. The surface area of the samples was calculated using the BET method.

4.3.4 Adsorption experiment

The CO_2 adsorption process was conducted using the CO_2-temperature programmed desorption (CO_2-TPD) technique. The samples underwent pretreatment at 250°C for 1 h under vacuum conditions. Subsequently, the adsorbents were exposed to CO_2 gas at a pressure of 1 bar and a temperature of 150°C for 1 h to facilitate adsorption. After the adsorption step, the sample was purged in a vacuum system under the same temperature and time as the adsorption phase to remove any physic-sorbed CO_2. The desorption process was initiated by heating the sample to 250°C and holding it at that temperature for 2 h. To detect the desorbing species, a quadrupole mass spectrometer (Balzers QMG) was employed. The desorbed gases were analyzed using the mass spectrometer to identify and quantify their composition.

The adsorption capacity of the samples was calculated in terms of $mmol·g^{-1}$. This calculation involved utilizing a linear calibration curve of CO_2 concentration divided by the mass of zeolite Y within the composite (Q, $mmol/g_{sample}$.). To compare the adsorption capacity between zeolite in composite and zeolite without carbon, the adsorption capacity per gram zeolite was calculated by equation (1).

$$\text{Adsorption capacity (mmol/g}_{\text{zeolite}}) = \frac{Q_{\text{cps}} - \left(\frac{Q_{\text{wood}} \times 100g}{W_{\text{wood}}}\right)}{W_{\text{zeolite}}} \times 100g \qquad (1)$$

Where, Q_{cps} and Q_{wood} (mmol/g) are adsorption capacity per gram of composite and wood under hydrothermal without zeolite, and W_{wood} (g) and W_{zeollite} are weight percent of wood or zeolite in the adsorbent.

4.4 Results and Discussion

4.4.1 Distribution and textural properties of zeolite NaY on treated wood

SEM technique was utilized to confirm the particle size of zeolite in both conditions. The images and particle size of Micron- and Nano-RWZ composites in Figure 4.1. Figure 4.1 reveal an octahedral shape of zeolite Y for both conditions. The images indicated that zeolite-carbon composite can be synthesized under both conditions. However, the particle size of zeolite Y in nano condition was smaller than that of zeolite Y in micron condition. The particle size of the micron-RWZ sample (shown in Figure 4.1a) is around 2.5-4.0 μm. While the nano-RWZ sample displayed the size of zeolite around 150-250 nm or ~0.2 μm. The gel composition of seed in nano condition has high alkalinity, resulting in a fast crystallization rate which gives a small particle size of zeolite. Zhao et al. (2021) studied the effect of base concentration on the size. They explained that during crystal growth in the micron sample, the ingress of sodium at a low concentration occurs at a comparatively slower rate within the amorphous precursor particles. Consequently, a substantial number of nuclei are generated, which subsequently undergo growth through aggregation owing to the constrained availability of sodium within the system. From the literature and our result, it can be investigated that alkalinity and water content of seed gel strongly affects the particle size of zeolite or zeolite formation (Zhao et al., 2021; Ryu et al., 2020).
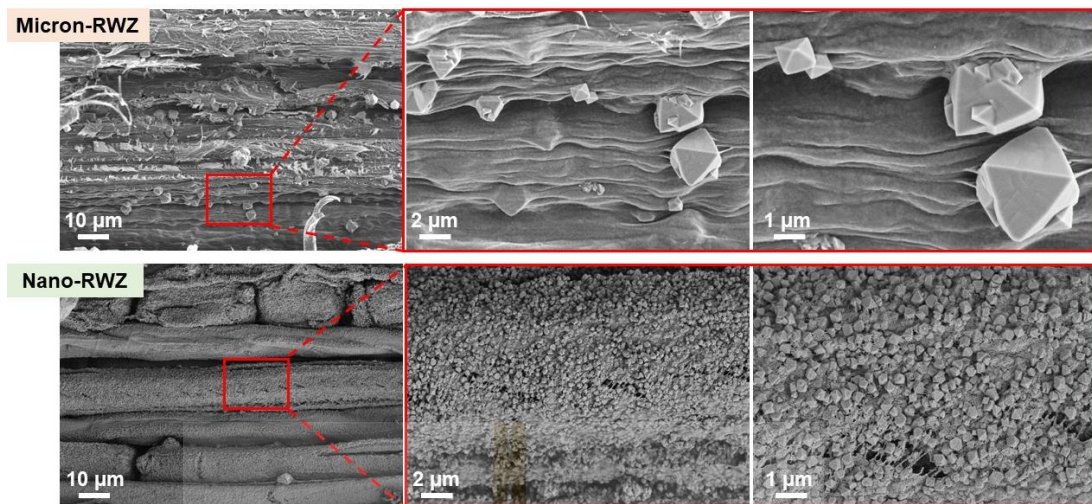
Figure 4.1 SEM images of Micron-RWZ and Nano-RWZ composites.

The SEM images of Nano-RWZ composite (Figure 4.1) display an excellent dispersion of zeolite Y on the wood surface without aggregation. It can be elucidated that zeolite could grow on any wood by hydrothermal method depending on the wall, area, or size of the carbon source. For example, in comparison between Krukkratoke et al. (2022) and our works, the zeolite loading on Lead tree wood is higher than on bamboo wood since the empty pore and pore diameter of Lead tree wood is smaller than that of bamboo wood.

In addition, TGA technique was used to study the degradation of samples in this work. The changes during carbonization include the loss of absorbed water (40-200°C) and carbon decomposition (200-700°C) (Zakikhani et al., 2016; Ribeiro et al., 2020). The zeolite loading in treated wood (RW) was calculated by subtracting the residual weight of the composite with residual carbon (represented in Figure 4.2). In Figure 4.2a-b, the weight percents of zeolite Y on both sizes of carbon were similar (~11%).
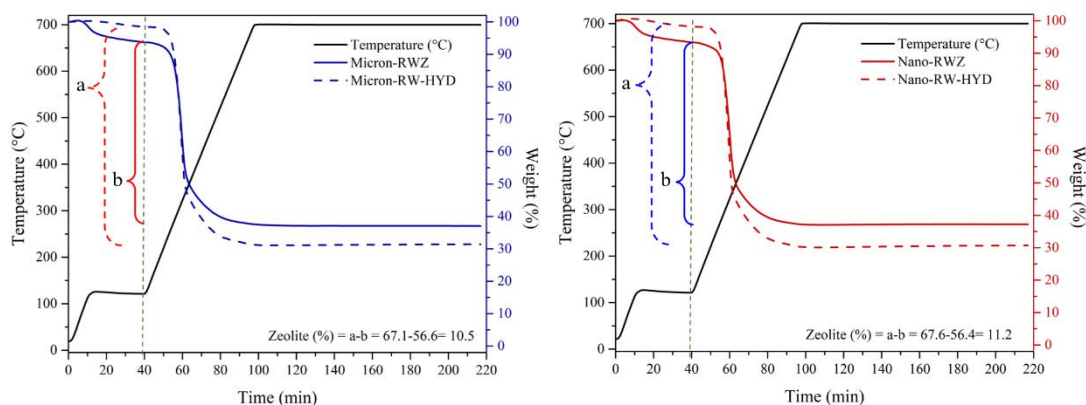
Figure 4.2 TGA profiles of Micron- and Nano-zeolite composites and carbon samples.

Figure 4.3 displays the N_2 sorption isotherms of Micron- and Nano-RWZ composites before the carbonization step. The Micron-RWZ sample exhibits a type I adsorption isotherm, the characteristic of microporous materials (ALOthman, 2012; Vu et al., 2018). The Nano-RWZ sample also displayed type I isotherm with H4-type hysteresis loops, which are characteristic of agglomerated particles with distinct edges, such as cubes and tetrahedra (Liu et al., 2020; Pala-Rosas et al., 2023). This agglomeration leads to the formation of pores with slit shapes that are uniform in size. Besides, surface area of Nano-RWZ and Micron-RWZ composites was 41 and 31 $m^2 \cdot g^{-1}$, respectively. The areas of both samples were not significantly different, probably due to the small amount of zeolite. The different kinds of porous structures in the Nano-RWZ sample may promote composite performance in CO_2 adsorption study.
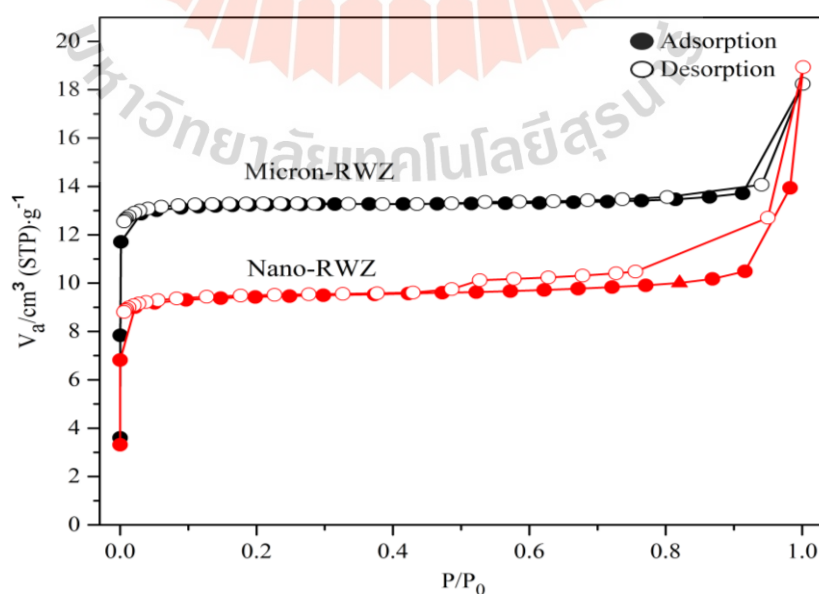
Figure 4.3 Isotherm of Micron-RWZ and Nano-RWZ composites.

The samples were carbonized under N_2 system to remove some carbon and clean the surface. The treated products were characterized to confirm the physical properties and applied for CO_2 adsorption to elucidate the particle size effect of zeolite.

4.4.2 Physical properties of carbonized carbon-zeolite composite

XRD, SEM, and N_2-sorption were performed to check phase, morphology, and textural properties of zeolite in the composite after carbonization.

The XRD patterns of zeolite Y and RWZ carbonized composites are displayed in Figure 4.4. All samples exhibited only the characteristic peaks of NaY following the standard in the JCPDS standard No. 39-1380. The XRD patterns confirm that only zeolite Y was present in the sample after carbonization. Besides, Nano/ZY-C and Nano-RWZ-C have boarder peaks and lower intensities than Micro/ZY-C and Micro-RWZ-C.
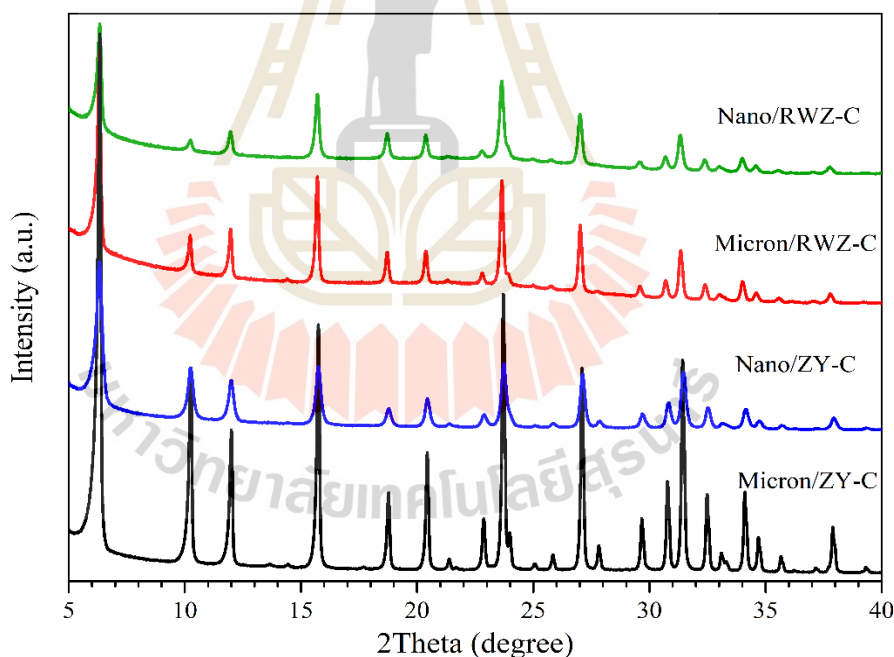
Figure 4.4 XRD patterns of composites after carbonization: composite Micron-RWZ-C, Nano-RWZ-C and zeolite Micron-ZY-C, Nano-ZY-C.

Figure 4.5 exhibits the SEM images of the Y-type zeolites on the carbon materials. The octahedral shape of zeolite NaY was observed in all samples after the composites were carbonized. Additionally, the average grain size of the zeolites on Nano/RWZ-C and Micron/RWZ-C samples remained the same, approximately 200 nm

and 3 μm, respectively. It can confirm that zeolite Y has high thermal stability, and the presence of carbon material improves the zeolite agglomeration problem. Generally, the zeolite agglomeration occurs easily on the calcination at high temperatures (more than 600°C), leading to large particle size and low active surface for adsorption.
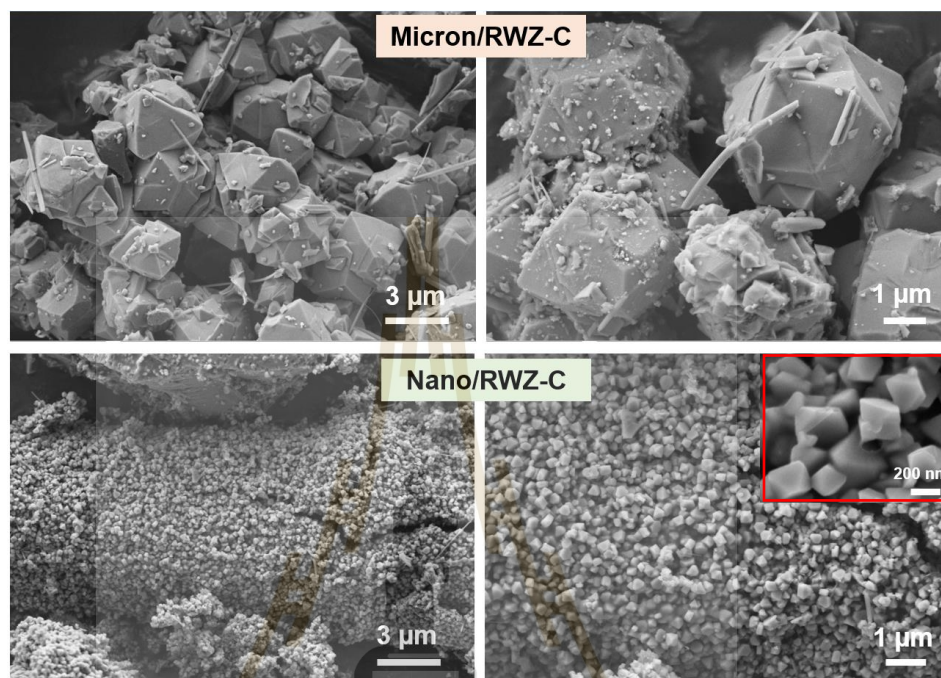
Figure 4.5 SEM images of carbonized Micron-RWZ and Nano-RWZ composites.

After the carbonization process, the surface areas of the composites increased to 96 and 93 $m^2 \cdot g^{-1}$, respectively. The small increase from the samples before carbonization indicated no significant changes in textual properties.

4.4.3 Testing of CO_2 adsorption on zeolite-carbon composites

Figure 4.6 displays the bar chart of CO_2 adsorption capacity per gram of carbonized samples, including refluxed and hydrothermal woods (Micron/RW-HYD-C and Nano/RW-HYD-C), zeolite-carbon composites (Micron/RWZ-C and Nano/RWZ-C), and zeolites (Micron/ZY-C and Nano/ZY-C). The results show that all samples could adsorb CO_2. For the micron group, the adsorption per gram of adsorbent was in the order: Micron/RW-HYD-C < Micron/RWZ-C < Micron/ZY-C. A similar trend was observed in the nano group; the adsorption per gram of adsorbent was in the order: Nano/RW-HYD-C < Nano/RWZ-C < Nano/ZY-C. These results highlight the superior CO_2 adsorption capability of zeolite Y compared to carbon from bamboo wood. The results indicate that zeolite content of 11% in Micron/RWZ-C and Nano/RWZ-C significantly improved the adsorption of the wood. Both composites (Micron/RWZ-C and Nano/RWZ-C)

showed lower adsorption than their parent zeolites (Micron/ZY-C and Nano/ZY-C) due to the low zeolite loading in the wood.

For the effect of zeolite sizes, the Nano/RWZ-C composite and Nano/ZY-C have a higher adsorption capacity than Micron/RWZ-C composite and Micron/ZY-C, respectively. The results could be attributed to better diffusion into the zeolite cavities on well-dispersed, smaller crystal sizes and hierarchical pore characters (seen in Figure 4.3).
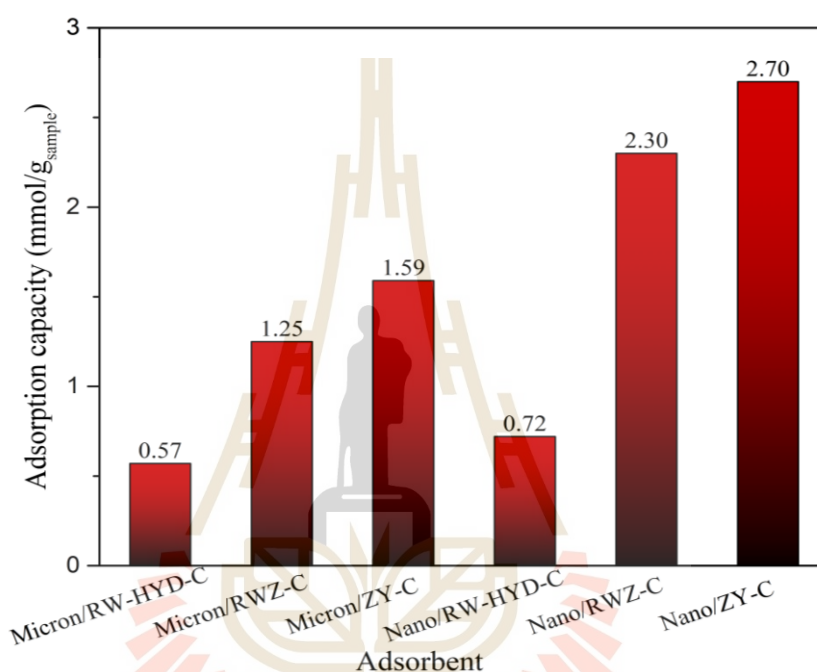
Figure 4.6 CO_2 adsorption capacity per gram sample of carbon materials (Micron/RW-HYD-C, Nano/RW-HYD-C), zeolite (Micron/ZY-C, Nano/ZY-C), and zeolite-carbon composites (Micron/RWZ-C, Nano/RWZ-C).

The CO_2 adsorption sites are on both wood and zeolite. Boer et al. (2023) reviewed that the active site for CO_2 adsorption on zeolite is cationic ion such as Na^+ ion by electrostatic interaction. The low adsorption of wood is possible (seen in the first and fourth bars) because it has the absorbed Na^+ ion on the wood surface in hydrothermal step.

Moreover, the adsorption capacity per gram of zeolite was calculated by equation (1) based on the capacity from both carbons, both composites, and both zeolites. Figure 4.7 presents a bar graph illustrating the CO_2 adsorption capacity per gram of zeolite, including zeolite-carbon composites (Micron/RWZ-C and Nano/RWZ-C) and zeolites (Micron/ZY-C and Nano/ZY). Micron/ZY-C showed nearly half the adsorption capacity of Nano/ZY-C, confirming the effect of crystal size. From the

composites, The composites demonstrated larger adsorption capacity than both sizes of the parent zeolite Y, attributed to zeolite agglomeration during carbonization, pretreatment, and adsorption steps. The Micron/RWZ-C also provided approximately half the adsorption capacity of the Nano/RWZ-C. The results confirmed that the dispersion of zeolite NaY in refluxed wood significantly enhanced CO_2 adsorption.
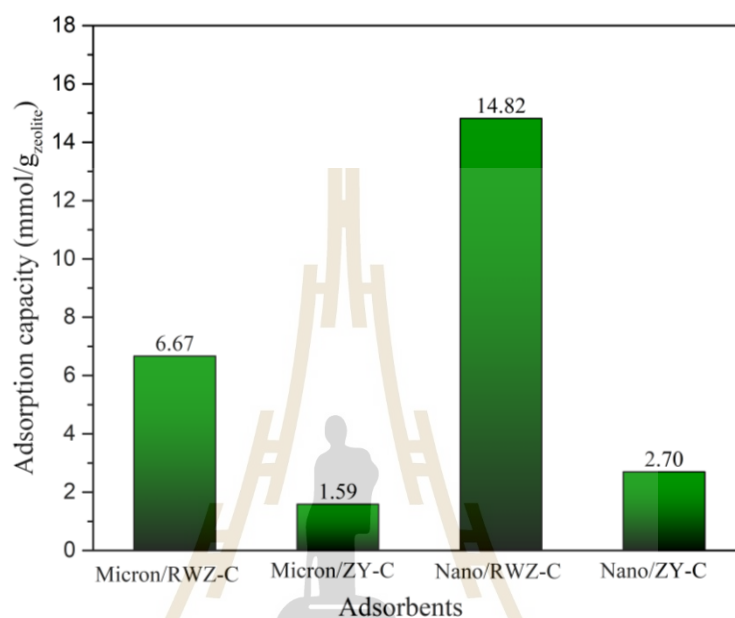
Figure 4.7 CO_2 adsorption capacity per gram zeolite of zeolite (Micron/ZY-C, Nano/ZY-C) and zeolite-carbon composites (Micron/RWZ-C, Nano/RWZ-C).

Furthermore, a smaller crystal size of zeolite promotes the diffusion of guest species into the absorbent. This outcome reflects the characteristics of the wood-zeolite composite and validates the objective of achieving a small zeolite size in bamboo wood by adjusting the water amount between the seed gel and feedstock gel. Notably, the Nano/RWZ-C composite exhibited the highest adsorption capacity due to its small particle size of zeolite and effective dispersion on treated wood, facilitating mass transfer of guest species (Malamis and Katsou, 2013). In conclusion, the adsorption capacity of gas increases with a decrease in zeolite particle size. Nano zeolite on bamboo wood from this work has many advantages, including facile preparation of composite pellet, easy to handle than powder form, and good performance for adsorption application.

4.5   Conclusions

The present study highlights the successful preparation of nano-zeolite Y on treated wood through the manipulation of water volume between the seed and feedstock gel and explores its potential application as an adsorbent for CO_2 capture. A facile hydrothermal method was employed to produce pellets of zeolite composites with nano-sized zeolite particles. The characterization of the synthesized composites determine the phase and particle size of the zeolite, followed by carbonization. The results demonstrate a significant reduction in zeolite particle size from 3-4 µm to 150-250 nm. However, the zeolite loading did not increase substantially in this study due to the presence of larger macropores. Based on the physical properties observed, it can be concluded that the alkalinity of the seed gel strongly influences the particle size of the zeolite, while the volume of macropores in the wood restricts the dispersion of zeolite on the substrate.

The carbonized composites were evaluated for CO_2 capture. The particle size and porous structure of the zeolites within the composite pellets play a significant role in determining their CO_2 adsorption capacity. Notably, nano-sized zeolite particles exhibited superior adsorption capacity than micron-sized particles when incorporated into the wood. This discovery provides valuable insights for selecting the appropriate zeolite size for incorporation into wood pellets intended for adsorption applications. Additionally, it is recommended to utilize carbon substrates with smaller pore sizes than bamboo wood to prepare zeolite-carbon composites, as this can further enhance their performance.

4.6   References

ALOthman, Z. A. (2012). A review: fundamental aspects of silicate mesoporous materials. *Materials, 5*(12), 2874-2902.

Anbia, M., Eskandari, A., and Jahangiri, M. (2016). Effect of particle size of NaX zeolite on adsorption of CO_2/CH_4. *International Journal of Engineering, 29*(1), 1-7.

Auerbach, S. M., Carrado, K. A., and Dutta, P. K. (2003). *Handbook of zeolite science and technology*: CRC press.

Gao, N. F., Kume, S., and Watari, K. (2005). Zeolite–carbon composites prepared from industrial wastes:(I) Effects of processing parameters. *Materials science and engineering: A, 399*(1-2), 216-221.

Garcıa-Martınez, J., Cazorla-Amorós, D., Linares-Solano, A., and Lin, Y. S. (2001). Synthesis and characterisation of MFI-type zeolites supported on carbon materials. *Microporous and Mesoporous Materials, 42*(2-3), 255-268.

Gleichmann, K., Unger, B., and Brandt, A. (2016). *Industrial zeolite molecular sieves*: IntechOpen.

Gunawan, T., Wijiyanti, R., and Widiastuti, N. (2018). Adsorption–desorption of CO_2 on zeolite-Y-templated carbon at various temperatures. *RSC Advances, 8*(72), 41594-41602.

Katsuki, H., Furuta, S., Watari, T., and Komarneni, S. (2005). ZSM-5 zeolite/porous carbon composite: conventional-and microwave-hydrothermal synthesis from carbonized rice husk. *Microporous and Mesoporous Materials, 86*(1-3), 145-151.

Lakhera, S. K., Harsha, S., and Suman, A. S. (2015). Synthesis and characterization of 13X zeolite/activated carbon composite. *Int. J. ChemTech Res, 7*, 1364-1368.

Lee, J. S., Kim, J. H., Kim, J. T., Suh, J. K., Lee, J. M., and Lee, C. H. (2002). Adsorption equilibria of CO_2 on zeolite 13X and zeolite X/activated carbon composite. *Journal of Chemical & Engineering Data, 47*(5), 1237-1242.

Liu, M., Ren, Y., Wu, J., Wang, Y., Chen, J., Lei, X., and Zhu, X. (2020). Effect of cations on the structure, physico-chemical properties and photocatalytic behaviors of silver-doped zeolite Y. *Microporous and Mesoporous Materials, 293*, 109800.

Ma, J., Si, C., Li, Y., and Li, R. (2012). CO_2 adsorption on zeolite X/activated carbon composites. *Adsorption, 18*, 503-510.

Malamis, S., and Katsou, E. (2013). A review on zinc and nickel adsorption on natural and modified zeolite, bentonite and vermiculite: examination of process parameters, kinetics and isotherms. *Journal of Hazardous Materials, 252*, 428-461.

Ozaki, J. I., Takahashi, K., Sato, M., and Oya, A. (2006). Preparation of ZSM-5 nanoparticles supported on carbon substrate. *Carbon, 44*(7), 1243-1249.

Pala-Rosas, I., Contreras, J. L., Salmones, J., López-Medina, R., Angeles-Beltrán, D., Zeifert, B., ..., and González-Hernández, N. N. (2023). Effects of the acidic and textural properties of Y-type zeolites on the synthesis of pyridine and 3-picoline from acrolein and ammonia. *Catalysts, 13*(4), 652.

Xu, R., Pang, W., Yu, J., Huo, Q., and Chen, J. *Chemistry of zeolites and related porous materials: synthesis and structure*: John Wiley and Sons.

Purnomo, C. W. (2013). Utilization of bagasse fly ash for carbon–zeolite composite preparation. *Journal of Porous Materials, 20*, 1305-1313.

Ribeiro, S. P. D. S., Martins, R. C., Barbosa, G. M., Rocha, M. A. D. F., Landesmann, A., Nascimento, M. A. C., and Nascimento, R. S. V. (2020). Influence of the zeolite acidity on its synergistic action with a flame-retarding polymeric intumescent formulation. *Journal of Materials Science, 55*(2), 619-630.

Rostami, M., Mofarahi, M., Karimzadeh, R., and Abedi, D. (2016). Preparation and characterization of activated carbon–zeolite composite for gas adsorption separation of CO_2/N_2 system. *Journal of Chemical & Engineering Data, 61*(7), 2638-2646.

Ryu, G. U., Khalid, H. R., Lee, N., Wang, Z. and Lee, H. K. (2020). The effects of NaOH concentration on the hydrothermal synthesis of a hydroxyapatite–zeolite composite using blast furnace slag. *Minerals, 11*(1), 21.

Siriwardane, R. V., Shen, M. S., and Fisher, E. P. (2003). Adsorption of CO_2, N_2, and O_2 on natural zeolites. *Energy & Fuels, 17*(3), 571-576.

Vu, H. T., Harth, F. M., and Wilde, N. (2018). Silylated zeolites with enhanced hydrothermal stability for the aqueous-phase hydrogenation of levulinic acid to γ-valerolactone. *Frontiers in Chemistry, 6*, 143.

Zakikhani, P., Zahari, R., Sultan, M. T. H., and Majid, D. L. A. A (2016). Thermal degradation of four bamboo species. *BioResources, 11*(1), 414-425.

Zhao, L., Yang, G., Guo, H., Wang, C., Wang, L., and Mintova, S. (2021). Effect of sodium concentration on the synthesis of faujasite by two-step synthesis procedure. *Chemical Research in Chinese Universities, 37*, 1137-1142.

CHAPTER V

OPERANDO STUDY OF ETHANOL-STEAM REFORMING ON CU-BASED ZEOLITE Y CATALYSTS BY X-RAY ABSORPTION SPECTROSCOPY: EFFECT OF ZEOLITE FORMS

5.1 Abstract

Ethanol steam reforming (ESR) has emerged as a crucial method for generating hydrogen, attracting considerable interest due to its effectiveness and positive environmental impact. The intricate sequence of reactions involved in ESR yields a range of products, including hydrogen, acetaldehyde, ethylene, and coke. Among the catalysts utilized, copper (Cu) stands out as the most desirable choice, renowned for its high selectivity in producing H_2. Typically, Cu catalyst is employed in conjunction with a supporting material possessing a substantial surface area, which promotes optimal dispersion of the catalyst. Zeolite Y, known for its advantageous properties, serves as a compelling alternative supporting material in this regard. In order to enhance the catalytic efficiency of Cu-based zeolite Y, various forms of zeolite were utilized, namely Na^+, NH_4^+, and H^+ forms (Cu/NaY, Cu/NH4Y, and Cu/HY). These zeolite-supported Cu catalysts were prepared by impregnation method and employed for the conversion of ethanol. To gain a deeper understanding of the structural transformations of copper during both pretreatment and the ESR process, a cutting-edge operando time-resolved X-ray absorption spectroscopy (TR-XAS) setup, in combination with gas chromatography (GC) and mass spectrometry (MS) techniques, was utilized. This innovative approach allowed for the identification of the specific pathway within the intricate reaction network and the examination of the reduction behavior exhibited by Cu-based catalysts. In the pretreatment stage, Cu^{II} in Cu/NaY was easy to reduce to Cu^0 compared to Cu/NH4Y and Cu/HY. The catalysts were selective towards acetaldehyde, hydrogen, and ethylene as ESR products. Cu/NaY showed a higher selectivity towards acetaldehyde and hydrogen products, attributed to the elevated $Cu^0/(Cu^I+Cu^{II})$ ratio. Conversely, Cu/NH4Y and Cu/HY was more selective for ethylene production due to their lower $Cu^0/(Cu^I+Cu^{II})$ ratio. Consequently, the specific forms of zeolite employed played a crucial role in determining the reducibility of the metal, ultimately influencing the ESR reaction

pathway. The results reveal the influence of zeolite forms on the catalytic performance, shedding light on the role of zeolite structure in ethanol-steam reforming on Cu-based catalysts. These findings contribute to understanding the reaction mechanism and provide valuable insights for designing and optimizing Cu-based catalysts for ethanol steam reforming applications.
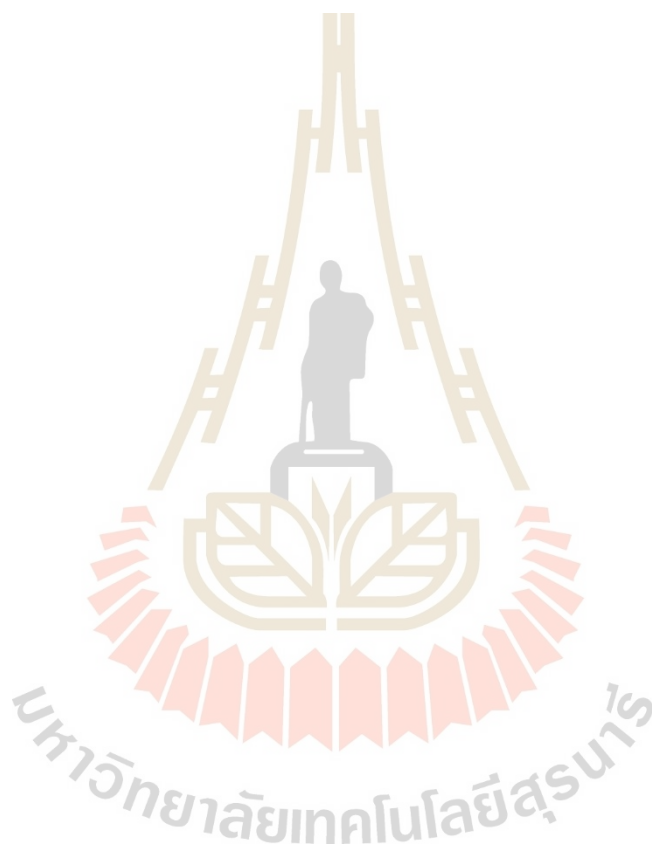
5.2   Introduction

Hydrogen (H_2) is recognized as a clean and versatile energy carrier with numerous applications, encompassing fuel cells, power generation, and transportation (Hou et al., 2015; Escalante et al., 2020). In recent years, ethanol steam reforming (ESR) has emerged as a promising pathway for sustainable H_2 production, utilizing ethanol as a renewable feedstock. Ethanol can be efficiently converted into H_2 through a series of reactions (represented in Scheme 5.1). The process starts with a dehydrogenation or dehydration reaction, which produces acetaldehyde. Acetaldehyde is then transformed into carbon monoxide and methane by breaking the carbon-carbon (C-C) bonds (Liu et al., 2022; Ogo and Sekine, 2022). However, the formation of carbon deposits during the production of ethylene from ethanol poses a significant challenge. The methane generated can react with steam through steam reforming to produce H_2 and carbon monoxide (CO). Additionally, carbon monoxide can be converted to carbon dioxide (CO_2) through a water-gas shift (WGS) reaction (Özkan et al., 2019; Chen et al., 2022).
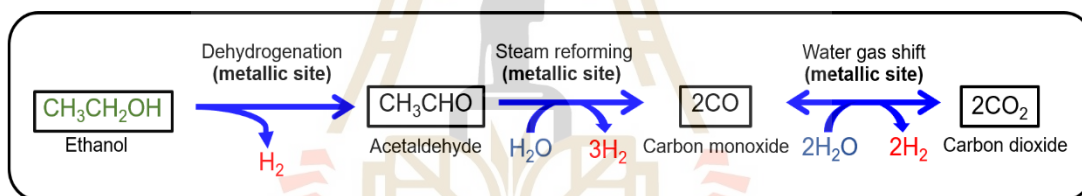
Scheme 5.1 Hydrogen production via ethanol steam reforming pathway.

The unique properties and catalytic performance of Cu-based zeolite catalysts have garnered significant attention as researchers strive to enhance the efficiency and selectivity of the ESR process (Sharma et al., 2017; Vizcaíno et al., 2007; Liu et al., 2022).

Cu-based zeolite catalysts offer significant advantages for ethanol steam reforming due to their unique properties and interactions. Zeolites provide a well-defined and porous structure with high surface areas, facilitating the dispersion and interaction of Cu species, which act as active sites for catalytic reactions (Martini et al., 2017). Copper (Cu) exhibits favorable redox properties and moderate cost, making it an attractive catalyst for ethanol activation and subsequent hydrogen (H_2) generation (Martini et al., 2017; Jones et al., 2009; Khanchi et al., 2022). On the other hand, not only the effect of metal on the catalytic activity, but also support properties including cationic ion surface. Generally, various forms of zeolite have different cationic species including Na^+, NH_4^+, and H^+ forms. Yao et al. (2022)

introduced the NH$_4$Z (Z= zeolite) as a supporting catalyst that improved the decomposition of catalyst compared with metal-based zeolite H form. They prepared Cu-based zeolite Y by ion-exchange method. However, this method takes time to reach equilibrium concentration and cannot control the precise amount of metal when compared to the incipient wetness impregnation method. Furthermore, Mitta et al. (2018) prepared Cu-based zeolite HY by impregnation method and vary loading for catalytic testing of glycerol hydrogenolysis. They found that low Cu loading around 3-5 wt% of Cu on zeolite HY presented good dispersion of Cu on the supports leading to high catalytic activity.

From the literature, 4% of Cu on zeolite NH$_4$Y catalyst was prepared by the impregnation method to study ethanol steam reforming in this work. Inokawa et al. (2010) prepared Ni and Co-based zeolite NaY by impregnation method to investigate the catalytic activity of ethanol steam reforming. They proposed that the cationic ion or acid-base properties of support influence the selective pathway to produce hydrogen from ethanol conversion. As a result, various forms of zeolite including sodium (NaY), ammonium (NH$_4$Y), and proton (HY) forms were used as supports of Cu in this work and investigate the influence of zeolite forms on the selective pathway of hydrogen production via ethanol conversion.

In addition, to optimize the design and performance of Cu-based zeolite catalysts, understanding the catalytic mechanisms and structural changes during ethanol steam reforming is crucial. *Operando* X-ray absorption spectroscopy (XAS) has emerged as a powerful technique for investigating catalysts under realistic reaction conditions (Martini et al., 2017). Operando XAS studies of Cu-based zeolite catalysts during ethanol steam reforming provide valuable information on the evolution of Cu species, their interaction with the zeolite framework, and the role of various Cu sites in the catalytic reactions (Martini et al., 2017; Pankin et al., 2020). This technique allows real-time monitoring of changes in the XAS spectra of Cu atoms during the reaction, enabling the correlation of structural changes with catalytic performance and providing mechanistic insights into the reaction pathways and active sites involved (Martini et al., 2017; Pankin et al., 2020).

Recent *operando* XAS studies revealed dynamic changes in the Cu oxidation state, coordination environment, and interaction with the zeolite framework under reaction conditions (Doronkin et al., 2014; Martini et al., 2017). These studies contribute to a better understanding of Cu-based zeolite catalysts and aid in the development of improved catalyst designs for ethanol steam reforming. This study aimed to investigate the behavior of Cu-based zeolite Y catalysts during ethanol

steam reforming using operando XAS. The changes of Cu species, their local environments, and electronic structures under realistic reaction conditions were studied. By correlating the spectroscopic data with catalytic performance measurements, the goal is to unravel the active sites and reaction mechanisms responsible for efficient H_2 production from ethanol on Cu-based zeolite Y catalysts.

The findings from this study will contribute to the fundamental understanding of the ESR process on Cu-based zeolite catalysts and provide crucial insights into the design and optimization of efficient and sustainable H_2 production systems. By employing operando XAS, we aim to bridge the gap between catalyst structure and performance.

5.3 Experimental

5.3.1 Synthesis of zeolite NaY

The zeolite Y was synthesized with a procedure modified from that in the literature (Mintova, Verified Syntheses of Zeolitic Materials, 3rd Revised Edition, 2016). First, sodium silicate solution was prepared by introducing 28.7 g of fumed silica (SiO_2, 99.8% Sigma Aldrich) in a base solution containing 11.48 g of NaOH and 59.82 g of DI water, and stirred on the water bath for 30 min. Next, 0.60 g of $NaAlO_2$ anhydrous ($Al_2O_3 \sim$ 55-56%, Riedel de Haën) was added to the alkaline solution to consist of 1.16 g of NaOH and 5.7 g of DI water and stirred until a clear solution. The sodium silicate solution of 6.49 g was slowly dropped into the solution and stirred for 15 min. Then, the aging time of the gel was 24 h. The resultant is Seed. Furthermore, 3.74 g of $NaAlO_2$ powder was added to the base solution consisting of 0.04 g NaOH and 37.2 g of DI water and stirred until a clear solution. The silicate solution of 40.69 g was slowly dropped into the clear solution, and it was stirred for 15 min. The resultant is Feed. Finally, the overall gel was generated from 4.71 g of seed gel and all of the feed gel and stirred for 30 minutes. The aging time of the overall gel was 24 h. After that, the gel was crystallized at 100°C for 24 h. The mixture was centrifuged, washed, and dried until pH=7, and white powder was obtained and put in the oven for drying at 100°C for 12 h. It was named NaY.

5.3.2 Preparation of zeolite Y in ammonium (NH₄Y) and proton forms (HY)

Zeolite Y in ammonium form (NH₄Y) was prepared by ion-exchanging the NaY with 0.2 M NH₄NO₃ solution at room temperature for 1 h. Then, the solid product was centrifuged, washed, and dried. The NH₄Y was obtained and used for

impregnation. The amount of zeolite was 1 g and the NH_4NO_3 solution was 50 g. Zeolite Y in protonic form (HY) was received by calcination of NH_4Y at 400°C.

5.3.3 Preparation of copper-based zeolite Y different zeolite forms by impregnation method

This study used the Na-form, NH_4-form, and H-form of zeolite Y as the supporting materials. Cu/NaY, Cu/NH₄Y, and Cu/HY catalysts with 4 wt.% CuO were obtained by incipient wetness impregnation method with $Cu(NO_3)_2 \cdot 3H_2O$ as a metal precursor. Next, the copper solution was slowly dropped on the support at room temperature within 5 min and stirred for 1 h. Then, the samples were dried at 110°C for 12 h. In the last step, the prepared catalysts were calcined at 450°C for 4 h under air. The amount of zeolite was 1 g and $Cu(NO_3)_2 \cdot 3H_2O$ solution is 1.2 ml. The obtained catalysts are designated as CuO/NaY, Cu/NH₄Y, and CuO/HY.

5.3.4 Catalyst characterization

The phrase of prepared catalysts was studied by X-ray diffraction, XRD (Bruker D8 ADVANCE) with a Cu Kα radiation (λ = 1.5406 Å) operated at 40 kV of voltage and 40 mA of current with a step size of 0.02° and speed of 0.2 s/step. Functional groups of obtained catalysts were analyzed by Fourier Transform Infrared Spectroscopy, FT-IR (Bruker Tensor 27) using Attenuated Total Reflectance (ATR) mode with a resolution at 4 cm^{-1} and number scan at 128. The size and distribution of copper on zeolite were analyzed by transmission electron microscope (TEM, Talos F200X, Thermo Fisher Scientific, Branchburg, NJ, USA). The specific surface areas of all catalysts were determined using the Brunauer-Emmet-Teller (BET) method, which involved N_2 physisorption at liquid N_2 temperature using a Micromeritics ASAP 2020 apparatus. Before the analysis, the powders were subjected to outgassing at 300°C and <13 μbar for 1 hour. In addition, the catalyst's acidity was assessed using NH_3 temperature-programmed desorption (NH_3-TPD) on a BELCAT-B instrument, the impurity of powders was removed at 300°C before adsorption. The sample adsorbed NH_3 gas at 50°C. The desorption study was performed between 50-700°C. To characterize acidic sites, pyridine probe molecules was employed for adsorption, followed by infrared measurements. The sample was pretreated under vacuum treatment at 300°C for 1 h. Infrared spectra were recorded using a Bruker IFS 28 FT-IR spectrometer equipped with an MCT detector, providing a resolution of 4 cm^{-1}. The adsorption of pyridine was performed at 150°C for 60 minutes. Reducibility was investigated using a time-resolved X-ray absorption (TRXAS) measurement with 10%H_2 in a N_2 gas flow and depended on the temperature and time of the Cu species (Cu K-edge probed) on the catalysts.

5.3.5 Catalytic testing

An *operando* spectroscopic study was performed at BL.2.2, Synchrotron Light Research Institute (SLRI) utilizing Total Reflection X-ray Absorption Spectroscopy (TRXAS) conducted in conjunction with Gas Chromatography (GC) and Mass Spectrometry (MS). The purpose of this study was to investigate the ethanol steam reforming (ESR) reaction and assess the structural changes of the catalysts employed. The analysis involved the identification and quantification of ethanol and ESR products using GC and MS techniques, while the X-ray Absorption Spectroscopy (XAS) technique was employed to evaluate the catalyst's structural transformations during the reaction.

To ensure accurate measurement of H_2 generation, the MS method, renowned for its high sensitivity to trace amounts of hydrogen, was predominantly employed. A catalyst powder was consolidated by hydraulic pressing at a force of 1 ton for a duration of 1 minute to form pellets, which were subsequently loaded into a sample cell. The catalysts were initially subjected to a temperature ramp from 50°C to 700°C over a period of 30 minutes. The *operando* XAS-GC-MS approach was continuously employed to monitor and analyze the catalytic reaction during ESR. The reactant stream, comprising ethanol and water, was supplied to the sample cell using saturated bubble tubes and a helium carrier gas. The mole ratio of ethanol to water was maintained at 1:4. The temperature range for the reaction was calculated to be between 200°C and 600°C. The concentration of each gas was obtained from the calibration curve (represented in Appendix C). The ethanol conversion and H_2 productivity were calculated by equations (1) and (2), respectively.

$$\text{Ethanol conversion (\%)} = \frac{\text{mol}_{EtOH}^{in} - \text{mol}_{EtOH}^{out}}{\text{mol}_{EtOH}^{in}} \times 100 \tag{1}$$

$$H_2 \text{ productivity (mol/min} \cdot \text{kg}_{cat}) = \frac{F_{H_2}^{out}}{g_{cat}} \times 100 \tag{2}$$

where mol_{EtOH}^{in} and mol_{EtOH}^{out} are moles of ethanol at the inlet and outlet of the reactor, respectively. $F_{H_2}^{out}$ (mol/min) the flow rate of H_2 at the reactor outlet, and g_{cat} (kg) is the catalyst weight.

5.4 Results and discussion

5.4.1 Characterizations

To investigate the influence of protonation and copper loading on the crystalline structure of the catalyst, X-ray diffraction (XRD) patterns were obtained for various samples including NaY, NH$_4$Y, HY, CuO/NaY, CuO/NH$_4$Y, and CuO/HY. Figure 5.1 displays the XRD pattern of zeolite Y, a crystalline aluminosilicate material in its sodium form (according to JCPDS No. 39-1380) which was found to be present in all samples. Notably, no discernible peaks were observed at the diffraction angles of 35.5° and 38.7° corresponding to the monoclinic CuO crystallite (according to JCPDS No. 48-1548), even after subjecting the samples to high-temperature treatment at 450°C. These findings suggest that the observed results in all CuY samples can be attributed to the effective dispersion of Cu species interacting with the zeolite framework, rather than the formation of new phases.
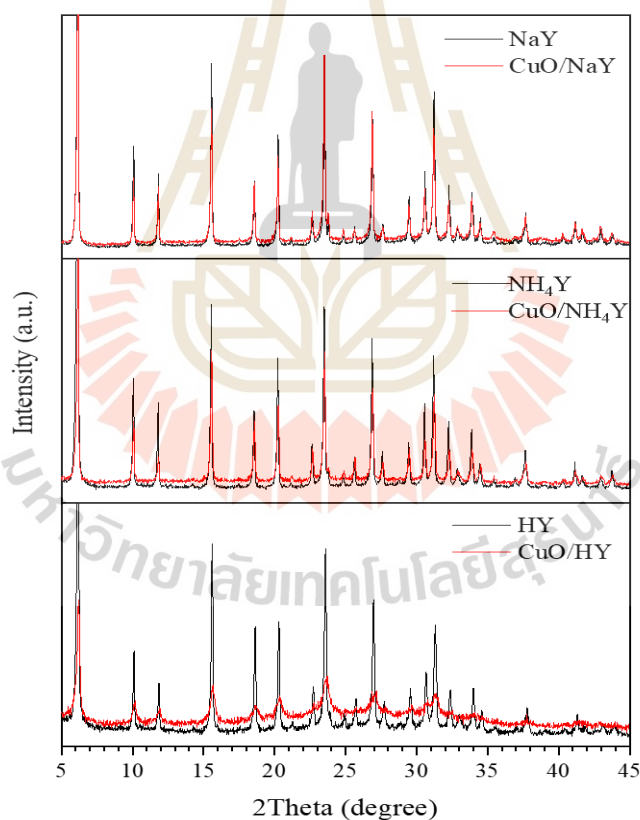

Figure 5.1 XRD patterns of zeolites (NaY, NH$_4$Y, HY) and Cu-zeolite Y catalysts (Cu/NaY, Cu/NH$_4$Y, Cu/HY).

The effects of different zeolite forms were investigated through the analysis of FTIR spectra in the range of 400-4000 cm^{-1} for copper on zeolite Y after calcination at 450°C, as illustrated in Figure 5.2. The characteristic peaks of zeolite Y were assigned and documented in Appendix C. Notably, the spectra of CuO/NH$_4$Y

and Cu/HY samples exhibited a distinct characteristic peak at 910 cm^{-1}, which corresponds to the [CuOH]$^{+}$ species (Borfecchia et al., 2015) and was absent in the CuO/NaY sample (as indicated by the black curve in Figure 5.2). The band observed at 910 cm^{-1} can tentatively be assigned to the d(O-H) mode of the same species, based on previous investigations (Borfecchia et al., 2015). It is important to note that a similar set of bands has been identified in relation to other metal-containing zeolites, and they have been attributed to the corresponding M-OH species. This suggests that the zeolite forms influence the oxide species of copper.
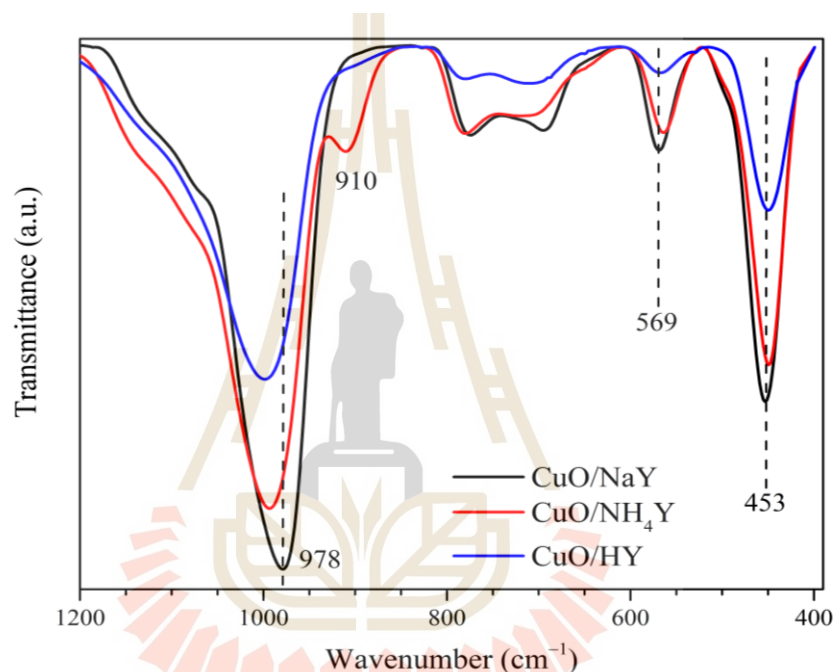

Figure 5.2 FTIR (ATR mode) spectra of CuO/NaY, CuO/NH$_4$Y, and CuO/HY catalysts.

Figure 5.3 displays the morphology of various Y-zeolite-supported copper catalysts and the distribution of copper oxide particles as observed through transmission electron microscopy (TEM). The images in Figure 5.3 demonstrate a uniform distribution of small copper oxide particles on each form of the Y-zeolite framework. The sizes of the metal oxide particles were determined to be 2-5 nm for CuO/NaY, 3-6 nm for CuO/NH$_4$Y, and 4-6 nm for CuO/HY, respectively. Among all the samples, CuO/NaY exhibited the smallest average size of CuO particles.
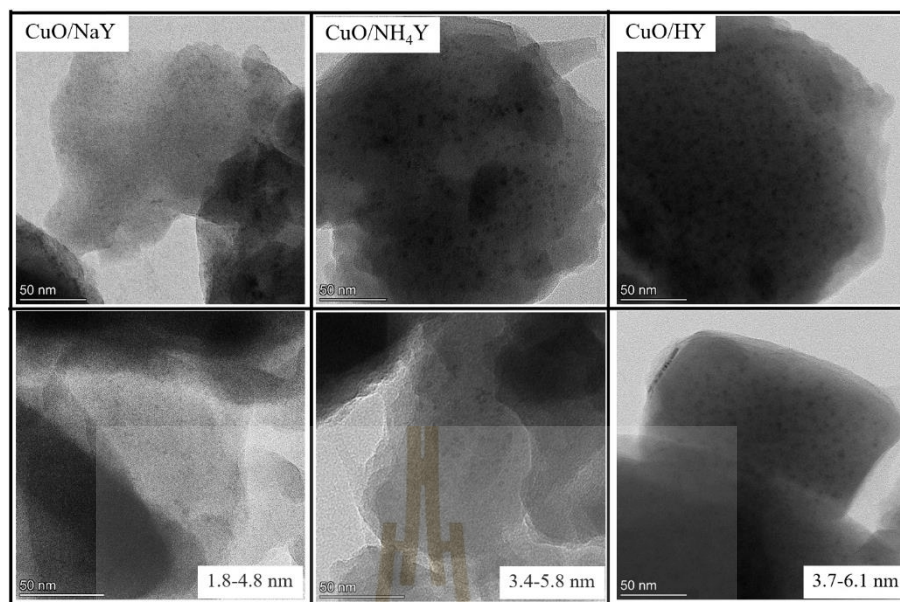
**Figure 5.3** TEM images of CuO/NaY, CuO/NH₄Y, and CuO/HY catalysts.

Table 5.1 Surface area of zeolite (NaY, NH₄Y, HY) and Cu-zeolite Y (CuO/NaY, CuO/NH₄Y, CuO/HY) catalysts.

Sample	BET surface area ($m^2 \cdot g^{-1}$)
NaY	603
NH_4Y	614
HY	586
CuO/NaY	592
CuO/NH_4Y	568
CuO/HY	399

Table 5.1 provides the textural characteristics, including the BET surface area. It is worth noting that the substance used in this study does not correspond to any specific IUPAC substance, as its properties are influenced by the synthesis process and environmental factors, which in turn affect the micro- and meso-porosity of the zeolite materials.

N_2 adsorption experiments (Figure 5.4) revealed a type I isotherm, indicating a predominantly microporous nature of the materials (based on the rapid and relatively high N_2 consumption at the initial stage of adsorption) (ALOthman, 2012; Vu et al., 2018). The surface areas of NaY, NH₄Y, and HY samples were found to

be approximately 603, 614, and 586 $m^2 \cdot g^{-1}$, respectively. Upon impregnation with the copper precursor (4 wt.%), the surface areas of CuO/NaY, CuO/NH$_4$Y, and CuO/HY catalysts were reduced to 592, 568, and 399 $m^2 \cdot g^{-1}$, respectively. These results align with the TEM findings, indicating that the well-dispersed copper oxide particles on NaY and NH$_4$Y zeolites contribute to higher surface areas of the catalysts. In the case of the CuO/HY sample, the data strongly suggested that the copper oxide species have partially blocked the zeolite network or that more zeolite structure collapse occurred after calcination at 450℃.
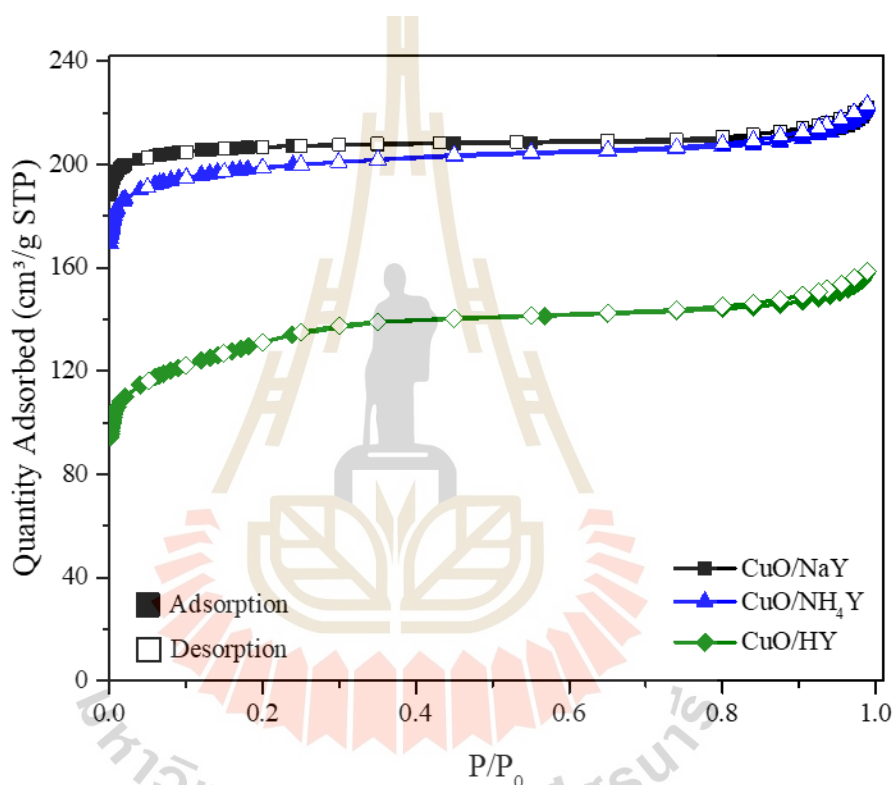
Figure 5.4 Isotherm of Cu-based zeolite Y catalysts.

Pure Y-zeolites and various CuO-supported Y-zeolite catalysts underwent NH$_3$-TPD analysis. Generally, weak acid sites are responsible for the desorption of ammonia in the first region, moderately strong acid sites contribute to the desorption in the second region, and strong acid sites lead to desorption in the third region.

All samples exhibited two distinct desorption peaks that were clearly distinguishable. In Figure 5.5, the first desorption peak, between 100 and 200℃, is attributed to weak acid sites. The second desorption peak was observed in the temperature range of 350-500℃, which corresponds to the desorption of ammonia

from strong acid sites (Milato et al., 2021; Mozgawa et al., 2021; Luo et al., 2018). The acidity of CuO/NaY sample was exhibited at the low range of temperature. From the TPD profile, CuO/NH₄Y sample had the highest total acidity. It showed the clearly peak at high temperature that represented a strong acid site. For the CuO/HY sample, a broad peak of strong acid was observed. As a result, CuO on zeolite NH₄Y and HY materials has high acidity which might serve selective pathway in dehydration route (Inokawa et al., 2010).
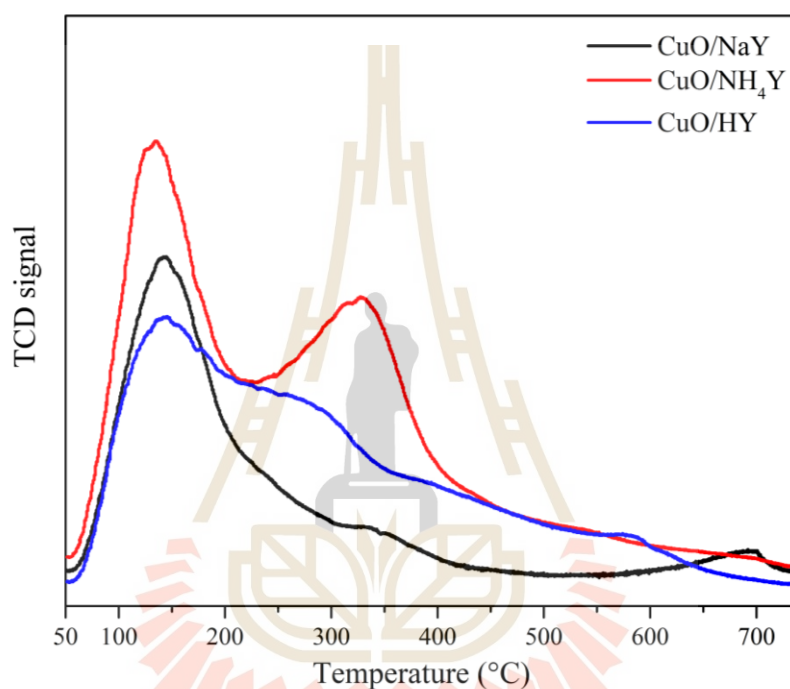

Figure 5.5 NH₃-TPD profile of of Cu/NaY, Cu/NH₄Y, and Cu/HY catalysts.

The NH₃-TPD method is unable to distinguish between Brønsted and Lewis acid sites. However, by employing pyridine adsorption followed by FTIR analysis, both types of sites can be observed. Figure 5.6 illustrates the absorption bands observed in all samples, namely 1540–1548 cm^{-1} and 1445–1460 cm^{-1}, which are characteristic of Brønsted acidic sites (protonated pyridine) and Lewis acid sites (coordinated pyridine), respectively. Furthermore, an additional IR absorption band was detected at 1490–1500 cm^{-1}, corresponding to both Brønsted and Lewis acid sites (Kung and Kung, 1985). Brønsted and Lewis acid sites were quantified by analyzing the absorbance intensities using molar extinction coefficients.

Table 5.2 Amount of acidic site of Cu-based catalyst.

Samples	Relative peak area/ $mg_{catayst}$	
	Lewis	Brønsted
CuO/NaY	0.125435	0.021767
CuO/NH$_4$Y	0.12967	0.077037
CuO/HY	0.196603	0.017234

       As summarized in Table 5.2, the results reveal an intriguing phenomenon observed in this study. When comparing the ammonium form of zeolite Y for supported copper catalysts, it was found that this form led to an increase in both Bronsted acid sites and Lewis acid sites. Notably, the CuO/HY sample exhibited the highest amount of Lewis acid sites. This result can be attributed to the larger presence of dispersed copper oxide particles on the external surface of the zeolite, which effectively blocked the H^+ sites of the support. On the other hand, the CuO/NH$_4$Y sample demonstrated the highest Bronsted acid site concentration. This outcome is likely due to the favorable distribution of copper oxide throughout the zeolite structure, allowing for a greater number of H^+ sites to be available.

       The presence of high Bronsted or Lewis acid sites has the potential to impact the reducibility and selective pathways for H$_2$ production from ethanol. The acidity of the catalysts can influence the adsorption and activation of reactant molecules, as well as the formation and stability of reaction intermediates. Therefore, the observed differences in acidity among the catalysts could result in variations in catalytic performance, selectivity, and efficiency. Further investigations are warranted into the specific effects of Bronsted and Lewis acid sites on the catalytic process of H2 production from ethanol. Understanding the role of acidity in this reaction can provide valuable insights for optimizing the catalyst design and enhancing the desired catalytic performance.
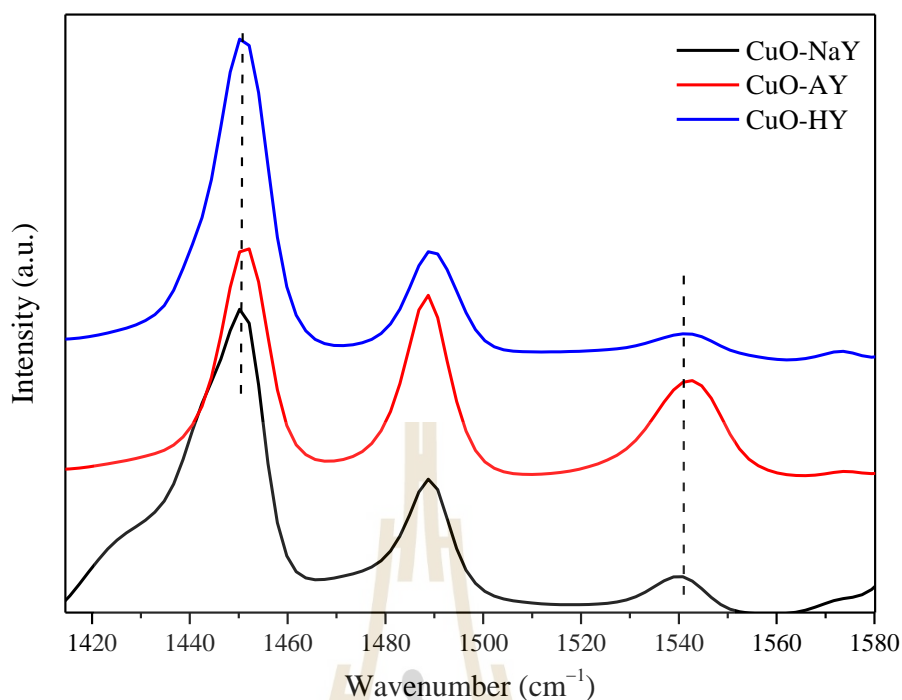
Figure 5.6 Pyridine-IR spectra of Cu/NaY, Cu/NH₄Y, and Cu/HY catalyst.

5.4.2 Reducibility of zeolite Y-supported Cu catalysts

In this section, Figures 5.7 depicts the comprehensive collection of in-situ temperature-dependent Cu K-edge XANES spectra obtained from the Cu catalyst supported on various forms of zeolite, namely Na-form, NH_4-form, and H-form. These spectra were acquired at various stages throughout the experiment under reduction conditions using a mixture of H_2 and N_2 gases.

In Figure 5.7a, CuO/NaY sample, the reduction starts at 180°C. More copper metal (around 85%) was received after reduction at 300°C. In addition, copper oxide as a major copper phase of CuO/NaY was directly changed to Cu (0) metal under H_2 reduction. No Cu (I) oxide phase was found during heating under H_2 atmosphere.

In Figure 5.7b, the reduction of Cu/NH4Y is different with Cu on NaY zeolite. From linear combination fitting (LCF), the starting phase of Cu on NH₄Y zeolite is mixing between CuO and $Cu(OH)_2$ that related IR result. The copper (II) oxide was reduced to more copper (I) oxide at 240°C. At 300°C, the percentage of copper (0) metal increased. After that, more copper metal (70%) was observed after reduction at 400°C.

For CuO/HY catalyst (shown in Figure 5.7c), the mixture ratio of $Cu(OH)_2$ and CuO is lower than Cu/NH₄Y sample. The result showed that the reduction starts at 280°C, and the copper (II) oxide was transformed to more copper

(0) metal and less copper (I) oxide. The reduction behavior of this sample was different with CuO/NH₄Y. More metal phase of Cu was obtained after 400°C. After 400°C, the species of copper still changed. The maximum percent of metal phase was 83% after 500°C.
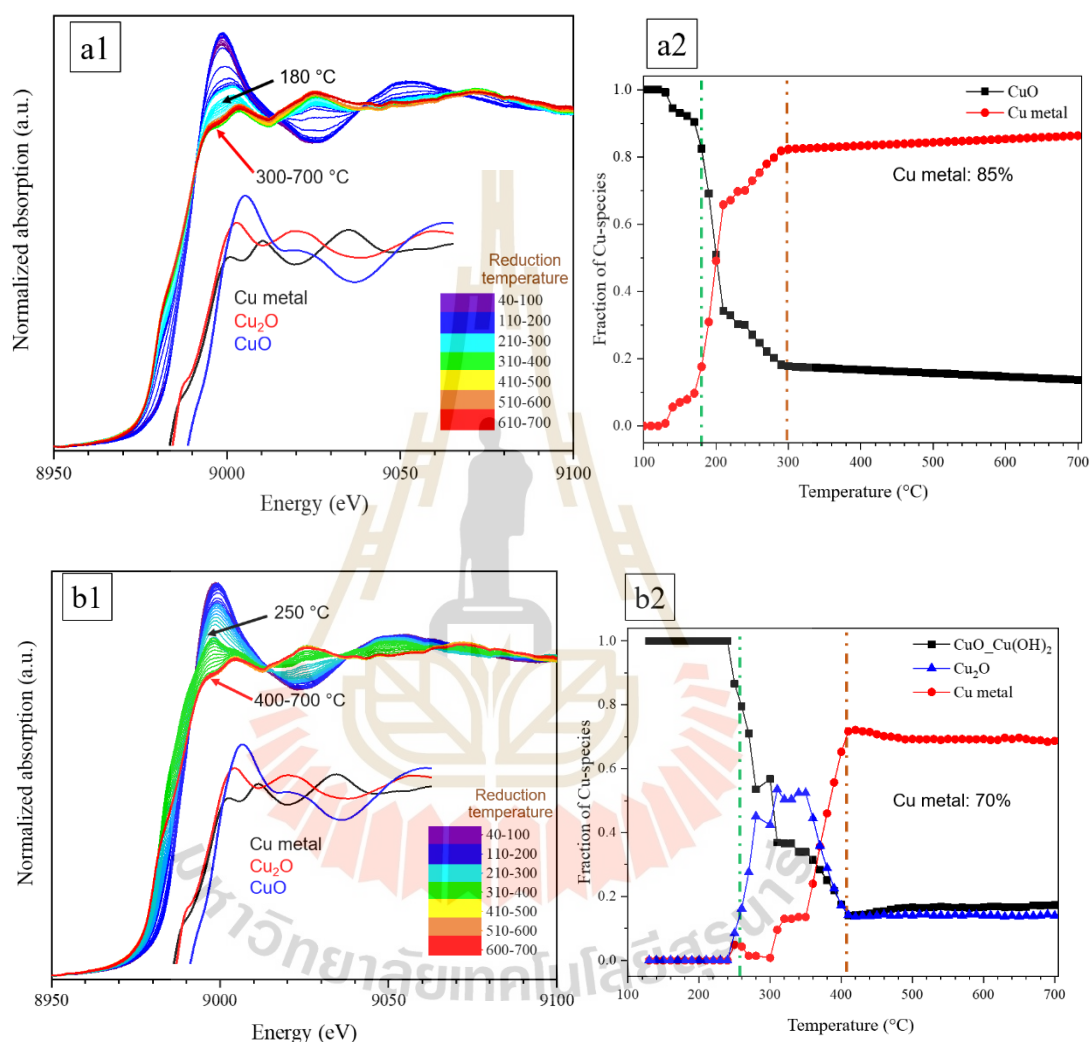

Figure 5.7 In situ XANES (1) and relative fraction of Cu species from LCF (2) of Cu-Zeolite Y catalysts with different zeolite forms (a=CuO/NaY, b=CuO/NH₄Y, c=CuO/HY) during reduction in H₂/N₂ flow from 25°C to 700°C, heating rate 5°C/min.
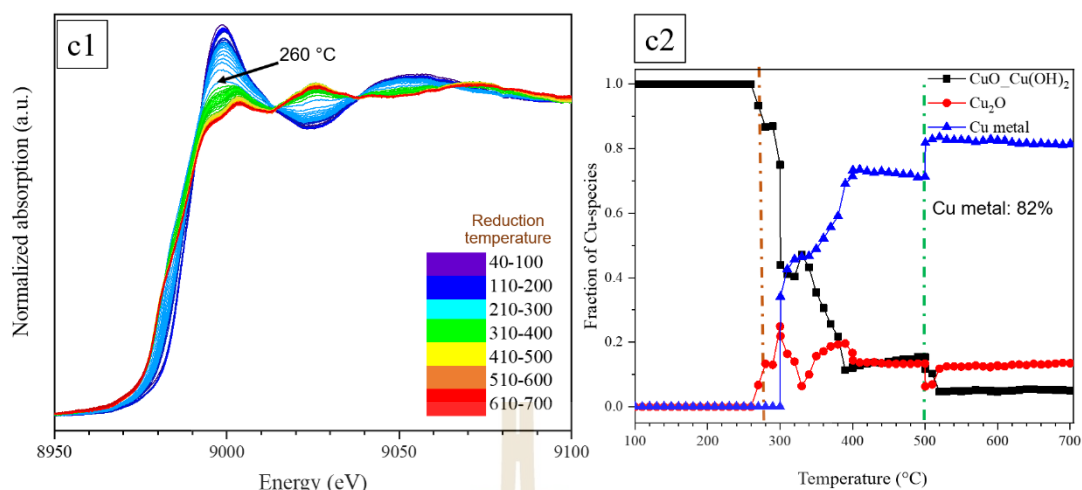
Figure 5.7 (Continued) In situ XANES (1) and relative fraction of Cu species from LCF (2) of Cu-Zeolite Y catalysts with different zeolite forms (a=CuO/NaY, b=CuO/NH$_4$Y, c=CuO/HY) during reduction in H$_2$/N$_2$ flow from 25°C to 700°C, heating rate 5°C/min.

On the other hand, Cu on NH$_4$Y zeolite that transformed to HY during calcination of copper precursor exhibits higher stability than Cu on HY zeolite. HY zeolite possesses a higher acidity due to the presence of more protons associated with the framework structure. The increased acidity of HY zeolite hinders the activation of hydrogen during the reduction process, making it more challenging for Cu species to undergo reduction to form metallic copper. In the case of good Cu dispersion on zeolite HY that transformed NH$_4$Y, the stronger acid sites in HY zeolite can act as Lewis acid sites, which tend to form stronger interactions with Cu species, resulting in reduced reactivity towards hydrogen activation and subsequent reduction. Therefore, the combination of the basicity of NaY and the acidity of NH$_4$Y and HY zeolite plays a crucial role in determining the ease of reduction of Cu species to Cu metal.

In addition, the possible reason of different routes of reduction to Cu metal of the copper (II) species might be the shape and location of the copper inside zeolite structure as Wang and coworkers reveal in their work. They prepared copper-based various kinds of zeolite. They investigated that the reduction of isolated Cu(II) occurs in two sequential stages, where Cu(II) is first reduced to Cu(I) and then further reduced to Cu(0). On the other hand, CuO$_x$ clusters and particles undergo a single-step reduction from Cu(II) to Cu(0). These reduction processes can be distinguished by their difference in temperatures. Similarly, the reduction of [Cu-O-Cu]$^{2+}$ in the form of isolated monomeric Cu(II) ions also occurs in two stages (Deka et al., 2013;

Wang et al., 2019). It could be implied that it might have more $[Cu\text{-}O\text{-}Cu]^{2+}$ in the form of isolated monomeric Cu(II) ions in zeolite NH_4Y by ion-exchanging between NH_4^+ ion and copper (II) ion precursor leading to observation of Cu(I) oxide during reduction study.

Besides, from the reducibility result, it could be implied that the higher basicity of NaY promotes hydrogen activation and facilitates the reduction process, making Cu on NaY more readily reduced compared to Cu on HY, where the stronger acidity hampers hydrogen activation and thus reduces the ease of Cu reduction.

The reduction of CuO and $Cu(OH)_2$ involves the conversion of these compounds into metallic copper (Cu) through the removal of oxygen atoms. However, the reduction mechanisms and conditions may differ for each compound. CuO (copper oxide) is typically more easily reducible compared to $Cu(OH)_2$ (copper hydroxide). This is primarily due to the difference in the strength of the Cu-O bonds and the thermodynamic stability of the compounds.

In the case of CuO, the Cu-O bond is relatively weaker, making it more susceptible to reduction. Reduction of CuO can occur through various mechanisms, including direct reduction by hydrogen gas (H_2) or other reducing agents. The reduction reaction involves the transfer of electrons to the CuO, leading to the removal of oxygen atoms and the formation of metallic Cu. The reaction can be represented as follows (Kim et al., 2003):

$$CuO + H_2 \longrightarrow Cu + H_2O$$

$Cu(OH)_2$, on the other hand, is more stable and less readily reducible compared to CuO. The stronger Cu-OH bonds in $Cu(OH)_2$ require more energy to break and more mole of H2 , making the reduction process more challenging. Generally, higher temperatures or stronger reducing agents are needed to facilitate the reduction of $Cu(OH)_2$. The reduction reaction of $Cu(OH)_2$ can be represented as (Giziński et al., 2020) :

$$Cu(OH)_2 + H_2 \longrightarrow Cu_2O + 2H_2O$$
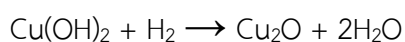
In conclusion, zeolite forms influence the dispersion, copper species, and interaction between zeolite and metal precursor leading to various behavior of reduction and metal species.

5.4.3 Catalytic activity of Cu-based zeolite Y catalysts in ESR reaction

The catalytic performance of Cu-based zeolite catalysts (Cu/NaY, Cu/NH_4Y, and Cu/HY) was evaluated for hydrogen production from ethanol in the

temperature range of 200 to 600°C, maintaining a molar H_2O/ethanol ratio of 4.0. The catalytic activity was monitored by GC couple with MS technique. The change of copper species was followed by in-situ TR-XAS. Figure 5.8 presents a comparison of ethanol conversion and product concentration, including H_2, CH_3CHO (Acetaldehyde), C_2H_4, and CH_4, over the catalysts. The result showed that the catalytic activity of three catalysts significantly changed when increasing the temperature after 300°C.

At 300-400°C, over the CuO/NH_4Y and CuO/HY catalysts, the ethanol conversion was higher than CuO/NaY catalyst because ethanol was converted to not only H_2 product by ESR route, but also more C_2H_4 product via dehydration pathway. However, these catalysts don't have high activity at low range of temperature (300-400°C). In this range of temperature, Cu/NaY catalyst showed selective to H_2 product via ESR pathway and less C_2H_4 production because it has high metallic site of copper that promote the ESR reaction. The result was relatively with reducibility testing in previous section. It can be correlated with an easy increase of Cu metal phase in Cu species plot from LCF fitting (Figure 5.9a). In this range of temperature, the active site of CuO/NH_4Y and CuO/HY catalysts provided a higher selectivity of C_2H_4 more than H_2 due to high acidity (Cu (I), Cu (II), and zeolite) and low metallic copper (displayed in Figure 5.9b-c). In addition, the copper (II) oxide phase in CuO/NH_4Y is still difficult reduce to copper (0) metal. It can be confirmed that the presence of copper (II) hydroxide phases ($[CuOH]^+$, $Cu(OH)_2$) of catalyst affects the reducibility of metal (Wang et al., 2019).

At 500°C, the trend of ethanol conversion from high to low was CuO/NH_4Y, CuO/HY, and CuO/NaY catalysts, respectively. The highest conversion on CuO/NH_4Y catalyst was observed due to high acidic site of catalyst coupled with a haft of metallic site leading to many routes of ethanol conversion including ESR, dehydration, or ethylene steam reforming. The pathway of H_2 production of Cu/NaY catalysts consists of ESR and dehydrogenation which can be seen in the acetaldehyde product H_2 formation. Besides, the catalyst showed low concentration of C_2H_4 product because of low acidity of the catalyst. For CuO/NH_4Y catalyst, there are two ways to convert the ethanol including ESR and dehydration. However, Cu-based zeolite NH_4Y showed high H_2 production like Cu-based NaY catalyst. Even though, it has low metallic site. From the XAS and catalytic results, it could be implied that the mixing species of copper promoted the H_2 production via ESR route as a main pathway coupled with ethylene steam reforming, which C_2H_4 was produced by ethanol dehydration on acidic site. On the other hand, in case of CuO/HY catalyst, the behavior of catalytic activity is similar with CuO/NaY and

CuO/NH$_4$Y catalysts. This copper catalyst showed many products including H$_2$, C$_2$H$_4$, and acetaldehyde. The main route of H$_2$ production consists of ESR, dehydrogenation, or ethylene steam reforming. Although the catalysts have a more metallic site (shown in Figure 5.9c) and higher ethanol conversion than CuO/NaY, the hydrogen production is lower than CuO/NaY catalyst. It can be indicated that the exact main part of hydrogen production for CuO/HY sample was obtained via ethanol dehydrogenation because the mole of H$_2$ from ESR route is lower than that of H$_2$ from ethanol dehydrogenation route (ED). While at 600°C, the CuO/NH$_4$Y catalyst still exhibited the highest ethanol conversion. It can confirm the result in the part of characterization that copper well dispersed on zeolite NH$_4$Y leading to high active site to convert ethanol. Besides, CuO/NaY catalyst displayed larger the conversion than CuO/HY catalyst. It means that the temperature that is suitable for ESR reaction to produce H$_2$ of CuO/NaY catalyst is 600°C. The Cu/NaY catalysts presented H$_2$ production from ESR and ED pathway as main routes. It can be observed by more acetaldehyde formation. In the case of CuO on NH$_4$Y catalyst, H$_2$ was produced based on ESR, Ethylene steam reforming, or Ethylene decomposition that confirmed by the increase of CH$_4$ and a decrease of C$_2$H$_4$. For CuO/HY catalyst, there are the lowest conversion and H$_2$ production due to more copper agglomeration or more collapse of zeolite structure. However, the selective pathway of H$_2$ production is like CuO/NH$_4$Y catalyst, but it has lower catalytic activity than CuO/NH$_4$Y sample. This observation suggests that higher Bronsted and Lewis acid site adversely affects the selective pathway of ethanol conversion to H$_2$ at the investigated temperatures. This observation suggests that higher Cu (0) concentrations adversely affect the rates of the ethanol steam reforming reaction (C$_2$H$_5$OH + 3H$_2$O $\longrightarrow$ 6H$_2$ + 2CO$_2$) and the Water-Gas Shift (WGS) reaction (CO + H$_2$O $\longrightarrow$ CO$_2$ + H$_2$) at the investigated temperatures.
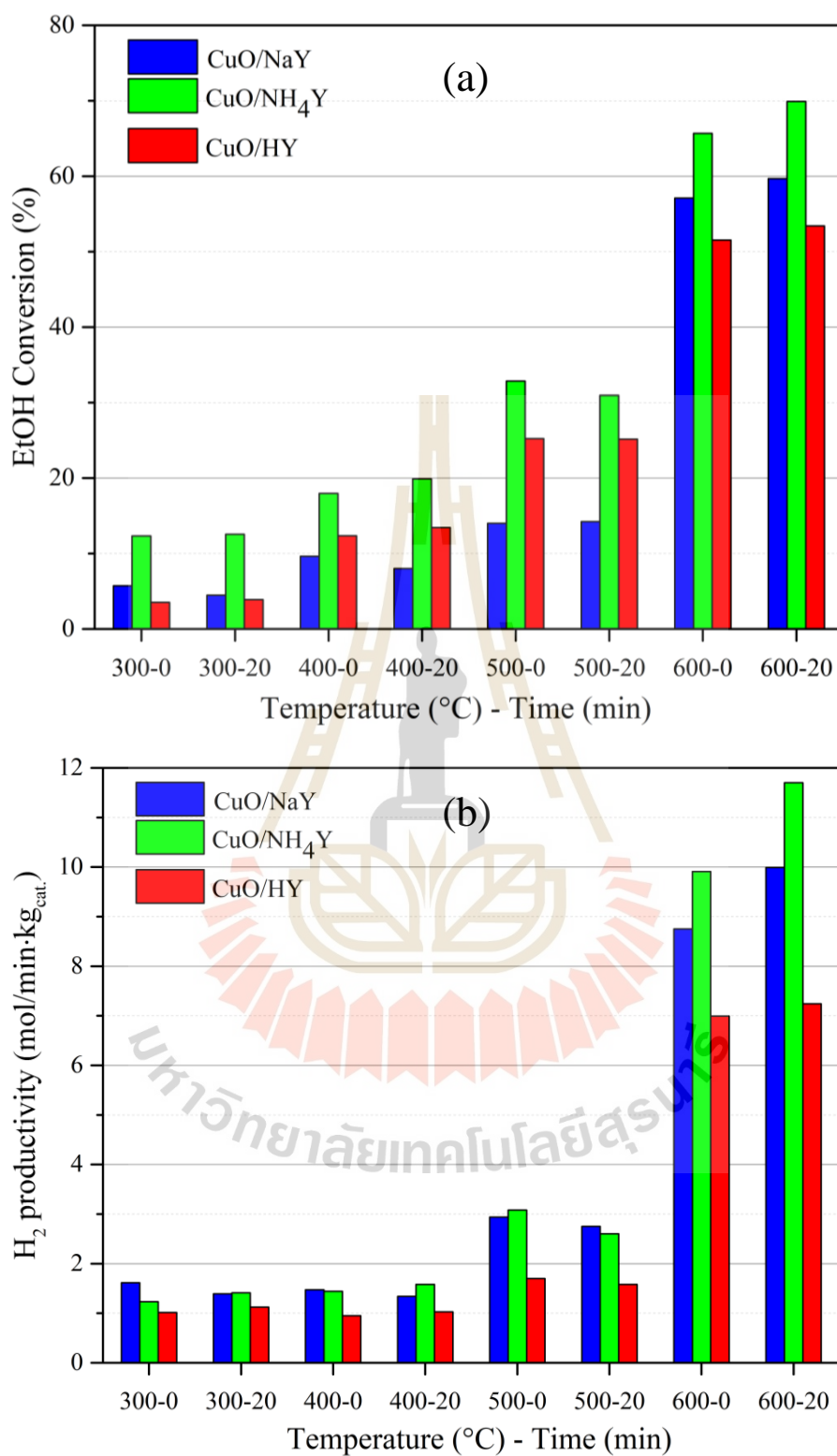
Figure 5.8 Ethanol conversion (a), H_2 productivity (b), and minor product concentration (c-e) of Cu-zeolite Y samples that different zeolite form including CuO/NaY, CuO/NH₄Y, and CuO/HY in the range of reaction temperature between 300-600℃.
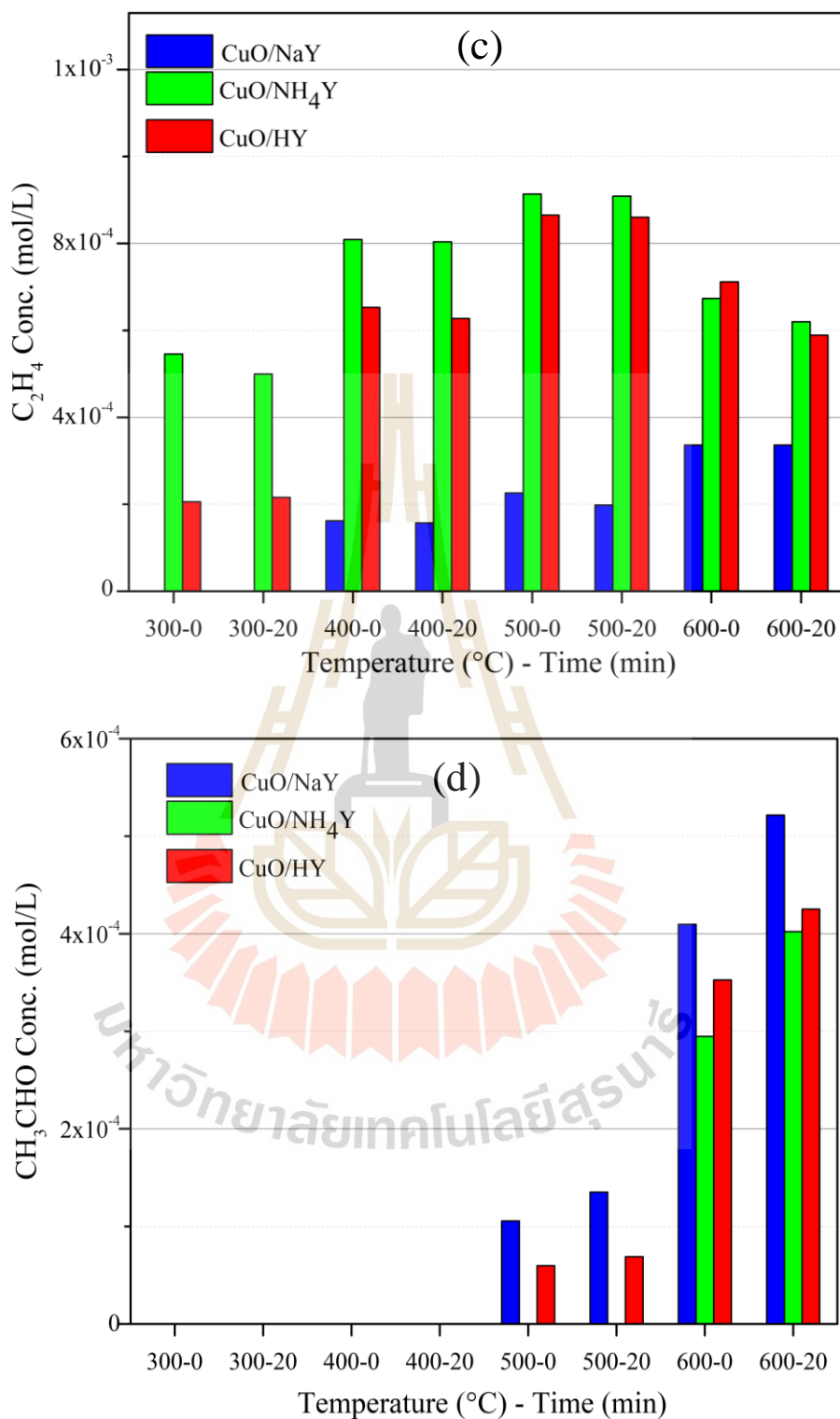
Figure 5.8 (Continued) Ethanol conversion (a), H_2 productivity (b), and minor product concentration (c-e) of Cu-zeolite Y samples that different zeolite form including CuO/NaY, CuO/NH₄Y, and CuO/HY in the range of reaction temperature between 300-600°C.
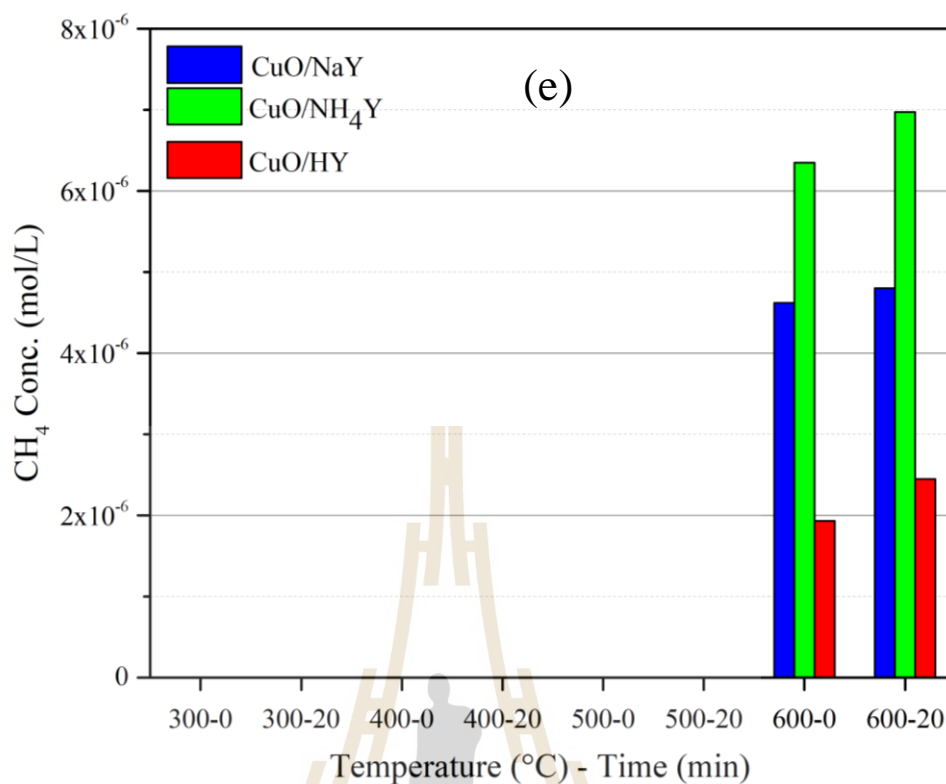
Figure 5.8 (Continued) Ethanol conversion (a), H_2 productivity (b), and minor product concentration (c-e) of Cu-zeolite Y samples that different zeolite form including CuO/NaY, CuO/NH₄Y, and CuO/HY in the range of reaction temperature between 300-600°C.
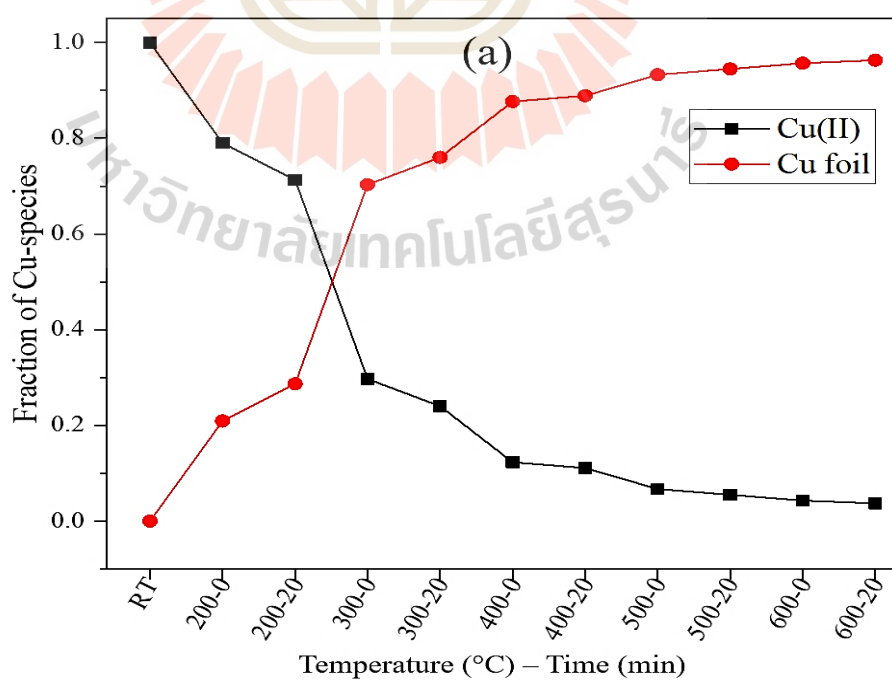

Figure 5.9 Relative fraction of Cu-species during ESR testing of CuO/NaY (a), CuO/NH₄Y (b), and CuO/HY (c) catalysts.
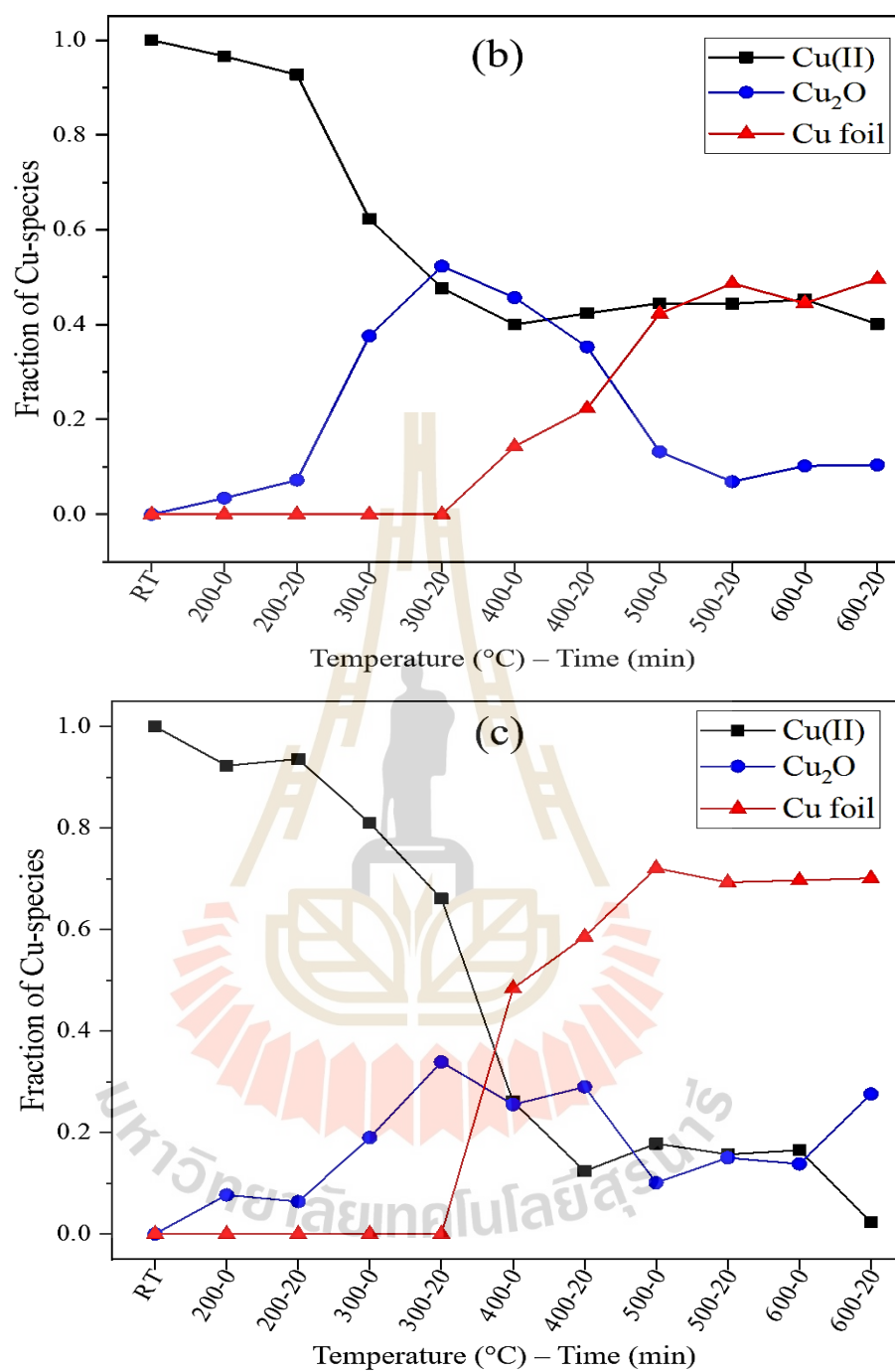
Figure 5.9 (Continued) Relative fraction of Cu-species during ESR testing of CuO/NaY (a), CuO/NH$_4$Y (b), and CuO/HY (c) catalysts.

5.5   Conclusions

Ethanol conversion through steam is considered an environmentally friendly method for producing clean energy carriers with high yields. In this study, Cu-based zeolite Y catalysts were prepared using the impregnation method to investigate reduction and catalytic activity.

The results revealed that different forms of zeolites with copper oxide led to variations in copper particle sizes and dispersion. The samples exhibited different reduction behaviors depending on the type of zeolite used as a supporting catalyst. The CuO/NaY sample demonstrated greater ease of reduction and higher reduction ability compared to the CuO/NH$_4$Y and CuO/HY samples. This can be attributed to the weaker interaction between zeolite and copper sites, as well as the copper species in the initial state.

Operando XAS analyses provided real-time monitoring of the catalyst structure and active sites during the reaction. The ESR study demonstrated that zeolite Y, as a supporting catalyst, promoted a selective pathway for hydrogen production with Cu catalyst. Cu catalysts on acidic supports like NH$_4$Y and HY exhibited a more selective route for hydrogen production through ESR and ethylene steam reforming or ethylene decomposition. The presence of high copper oxide species in the reaction facilitated hydrogen production through side reactions, including ethylene steam reforming or ethylene decomposition. In contrast, Cu-based catalysts on basic supports like NaY exhibited a selective pathway for H$_2$ production through ESR and ethanol dehydrogenation.

The study's outcome provided a deeper understanding of the changes in copper structure during reduction and reaction, highlighting the crucial role of zeolite form in copper reducibility and the selective pathway for ethanol conversion. In addition, combination of TR-XAS with GC and MS techniques like operando has many advantages including shorten time and decrease energy consumption of the study.

5.6   References

ALOthman, Z. A. (2012). A review: fundamental aspects of silicate mesoporous materials. *Materials, 5*(12), 2874-2902.

Borfecchia, E., Lomachenko, K. A., Giordanino, F., Falsig, H., Beato, P., Soldatov, A. V., ..., and Lamberti, C. (2015). Revisiting the nature of Cu sites in the activated Cu-SSZ-13 catalyst for SCR reaction. *Chemical science, 6*(1), 548-563.

Chen, D., Liu, C., Mao, Y., Wang, W., and Li, T. (2020). Efficient hydrogen production from ethanol steam reforming over layer-controlled graphene-encapsulated Ni catalysts. *Journal of Cleaner Production, 252*, 119907.

Cudennec, Y., and Lecerf, A. (2003). The transformation of Cu $(OH)_2$ into CuO, revisited. *Solid state sciences, 5*(11-12), 1471-1474.

Deka, U., Lezcano-Gonzalez, I., Weckhuysen, B. M., and Beale, A. M. (2013). Local environment and nature of Cu active sites in zeolite-based catalysts for the selective catalytic reduction of NO x. *ACS Catalysis, 3*(3), 413-427.

Doronkin, D. E., Casapu, M., Günter, T., Müller, O., Frahm, R., and Grunwaldt, J. D. (2014). Operando spatially-and time-resolved XAS study on zeolite catalysts for selective catalytic reduction of NO x by NH_3. *The Journal of Physical Chemistry C, 118*(19), 10204-10212.

Escalante, Y., Galetti, A. E., Gomez, M. F., Furlong, O. J., Nazzarro, M. S., Barroso, M. N., and Abello, M. C. (2020). Hydrogen production by ethanol steam reforming: A study of Co-and Ce-based catalysts over FeCrAlloy monoliths. *International Journal of Hydrogen Energy, 45*(41), 20956-20969.

Giziński, D., Brudzisz, A., Santos, J. S., Trivinho-Strixino, F., Stępniowski, W. J., and Czujko, T. (2020). Nanostructured anodic copper oxides as catalysts in electrochemical and photoelectrochemical reactions. *Catalysts, 10*(11), 1338.

Hou, T., Zhang, S., Chen, Y., Wang, D., and Cai, W. (2015). Hydrogen production from ethanol reforming: Catalysts and reaction mechanism. *Renewable and Sustainable Energy Reviews, 44*, 132-148.

Inokawa, H., Nishimoto, S., Kameshima, Y., and Miyake, M. (2010). Difference in the catalytic activity of transition metals and their cations loaded in zeolite Y for ethanol steam reforming. *International Journal of Hydrogen Energy, 35*(21), 11719-11724.

Khanchi, M., Mousavian, S. M. A., and Soltanali, S. (2022). Methanol steam reforming over Cu supported on SiO_2, amorphous SiO_2-Al_2O_3, and Al_2O_3 catalysts: Influence of support nature. *International Journal of Hydrogen Energy, 46*(3), 3057-3071.

Kim, J. Y., Rodriguez, J. A., Hanson, J. C., Frenkel, A. I., and Lee, P. L. (2003). Reduction of CuO and Cu_2O with H_2: H embedding and kinetic effects in the formation of suboxides. *Journal of the American Chemical society, 125*(35), 10684-10692.

Kung, M. C., and Kung, H. H. (1985). IR studies of NH_3, Pyridine, CO, and NO adsorbed on transition metal oxides. *Catalysis Reviews Science and Engineering, 27*(3), 425-460.

Liu, Q., Zhou, H., and Jia, Z. (2022). Hydrogen production by ethanol reforming on supported Ni–Cu catalysts. *ACS omega, 7*(5), 4577-4584.

Luo, J., Kamasamudram, K., Currier, N., and Yezerets, A. (2018). NH$_3$-TPD methodology for quantifying hydrothermal aging of Cu/SSZ-13 SCR catalysts. *Chemical Engineering Science, 190*, 60-67.

Martini, A., Borfecchia, E., Lomachenko, K. A., Pankin, I. A., Negri, C., Berlier, G., ..., and Lamberti, C. (2017). Composition-driven Cu-speciation and reducibility in Cu-CHA zeolite catalysts: a multivariate XAS/FTIR approach to complexity. *Chemical science, 8*(10), 6836-6851.

Milato, J. V., França, R. J., and Marques, M. R. (2021). Pyrolysis of oil sludge from the offshore petroleum industry: influence of different mesoporous zeolites catalysts to obtain paraffinic products. *Environmental Technology, 42*(7), 1013-1022.

Mitta, H., Seelam, P. K., Ojala, S., Keiski, R. L., and Balla, P. (2018). Tuning Y-zeolite based catalyst with copper for enhanced activity and selectivity in vapor phase hydrogenolysis of glycerol to 1, 2-propanediol. *Applied Catalysis A: General, 550*, 308-319.

Mozgawa, B., Zasada, F., Fedyna, M., Góra-Marek, K., Tabor, E., Mlekodaj, K., ..., and Sojka, Z. (2021). Analysis of NH$_3$-TPD Profiles for CuSSZ-13 SCR Catalyst of Controlled Al Distribution–Complexity Resolved by First Principles Thermodynamics of NH$_3$ Desorption, IR and EPR Insight into Cu Speciation. *Chemistry–A European Journal, 27*(68), 17159-17180.

Özkan, G., Şahbudak, B., and Özkan, G. (2019). Effect of molar ratio of water/ethanol on hydrogen selectivity in catalytic production of hydrogen using steam reforming of ethanol. *International Journal of Hydrogen Energy, 44*(20), 9823-9829.

Pankin, I. A., Martini, A., Lomachenko, K. A., Soldatov, A. V., Bordiga, S., and Borfecchia, E. (2020). Identifying Cu-oxo species in Cu-zeolites by XAS: A theoretical survey by DFT-assisted XANES simulation and EXAFS wavelet transform. *Catalysis Today, 345*, 125-135.

Passos, A. R., La Fontaine, C., Martins, L., Pulcinelli, S. H., Santilli, C. V., and Briois, V. (2018). Operando XAS/Raman/MS monitoring of ethanol steam reforming reaction–regeneration cycles. *Catalysis Science & Technology, 8*(24), 6297-6301.

Sharma, Y. C., Kumar, A., Prasad, R., and Upadhyay, S. N. (2017). Ethanol steam reforming for hydrogen production: Latest and effective catalyst modification

strategies to minimize carbonaceous deactivation. *Renewable and Sustainable Energy Reviews, 74*, 89-103.

Vizcaíno, A. J., Carrero, A., and Calles, J. A. (2007). Hydrogen production by ethanol steam reforming over Cu–Ni supported catalysts. *International Journal of Hydrogen Energy, 32*(10-11), 1450-1461.

Vu, H. T., Harth, F. M., and Wilde, N. (2018). Silylated zeolites with enhanced hydrothermal stability for the aqueous-phase hydrogenation of levulinic acid to γ-valerolactone. *Frontiers in Chemistry, 6*, 143.

Wang, H., Xu, R., Jin, Y., and Zhang, R. (2019). Zeolite structure effects on Cu active center, SCR performance and stability of Cu-zeolite catalysts. *Catalysis Today, 327*, 295-307.

Yao, J., He, Y., Zeng, Y., Feng, X., Fan, J., Komiyama, S., ..., and Tsubaki, N. (2022). Ammonia pools in zeolites for direct fabrication of catalytic centers. *Nature Communications, 13*(1), 935.

CHAPTER VI
CONCLUSIONS

Zeolite NaY crystals were successfully dispersed onto bamboo wood using hydrothermal methods. To achieve this, zeolite gel was incorporated into the wood, and then crystallization took place. The distribution of zeolite crystals was more prominent on the outer surface of the wood compared to the inner part. The zeolite content on acid-refluxed wood increased significantly (20.72 wt%) compared to untreated wood (5.46 wt%). The size of the zeolite crystals was approximately 5 μm, and they were evenly spread on the wood surface without clumping together. The interaction between zeolite NaY and the wood occurred through the carboxyl group of the wood and the sodium ions in zeolite NaY. In aqueous solutions, the zeolite-wood composite demonstrated effective adsorption of Ni (II) ions. The adsorption capacity of the acid-treated wood composite was twice that of untreated wood and similar to that of a NaY pellet. Additionally, the composite could be easily separated from the solution, making it practical for use.

In the second study, the present study successfully prepared nano-zeolite Y on treated wood by manipulating water volume during the hydrothermal process. The synthesized composites exhibited a significant reduction in zeolite particle size, highlighting the influence of alkalinity and macropore volume on particle size and dispersion. The evaluation of carbonized composites demonstrated the superior CO_2 adsorption capacity of nano-sized zeolite particles when incorporated into the wood substrate. These findings offer valuable guidance for selecting zeolite size in wood pellets for enhanced adsorption applications and suggest the use of carbon substrates with smaller pore sizes for further performance improvements.

In the third research, the utilization of steam for ethanol conversion is a recognized environmentally friendly approach to efficiently produce clean energy sources. This study specifically investigated Cu-based zeolite Y catalysts prepared using the impregnation method. The results indicated that different forms of zeolites combined with copper oxide influenced the size and dispersion of copper particles. The reduction behavior exhibited by the samples varied depending on the type of zeolite used as a supporting catalyst. The CuO/NaY sample showed superior ease of reduction and higher reduction ability compared to the CuO/NH$_4$Y and CuO/HY

samples. This can be attributed to the weaker interaction between zeolite and copper sites, as well as the initial state of the copper species.

By employing operando X-ray absorption spectroscopy (XAS) analyses, researchers monitored the catalyst structure and active sites in real-time during the reaction. The ESR study revealed that zeolite Y, acting as a supporting catalyst, facilitated a selective pathway for hydrogen (H_2) production with a Cu catalyst. Cu catalysts on acidic supports such as NH_4Y and HY exhibited a more selective route for H_2 production through ESR, involving ethylene steam reforming or ethylene decomposition. The presence of high copper oxide species in the reaction promoted hydrogen production through side reactions, including ethylene steam reforming or ethylene decomposition. Conversely, Cu-based catalysts on basic supports like NaY showed a selective pathway for H_2 production through ESR and ethanol dehydrogenation.

Overall, two sections of these research findings demonstrated economical and environmentally friendly materials like pellet of bamboo wood-carbon composite for removal of pollutants. From the last research, the study's outcome provided a deeper understanding of the changes in copper structure during reduction and reaction, highlighting the crucial role of zeolite form in copper reducibility and the selective pathway for ethanol conversion.

APPENDICES
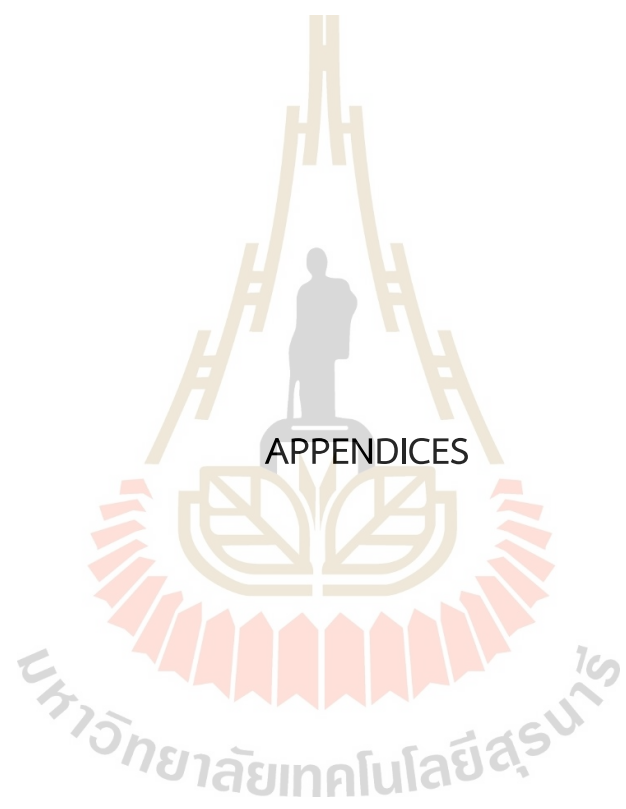
APPENDIX A
SUPPORTING INFORMATION FOR SYNTHESIS OF WELL-DISPERSED
# ZEOLITE NaY IN BAMBOO WOOD

Table A.1 Peak-fitted C1s and O1s from XPS data.

Samples	C1s			C4	O1s		
	C1	C2	C3	C4	O1	O2	O3
	(C*-C/C*=C)	(H-C*-O)	(H-C*=O/O-C*-O)	(O=C*-O)	(C=O/O-C=O)	(C-O)	(C=O)
W	49.91	30.80	11.68	7.61	19.18	59.38	21.44
RW	40.49	45.20	10.10	4.21	9.01	81.83	9.16

Table A.2 Thermal degradation of untreated wood (W) and treated wood (RW) in air zero flow.

Samples	Water evaporation		1st step		2nd step		3rd step	
	wt. lost [%]	T_d [°C]	wt. lost [%]	T_d [°C]	wt. lost [%]	T_d [°C]	wt. lost [%]	T_d [°C]
W	3	71	7	195	56	287	34	422
RW	3	70	-	-	71	320	26	502
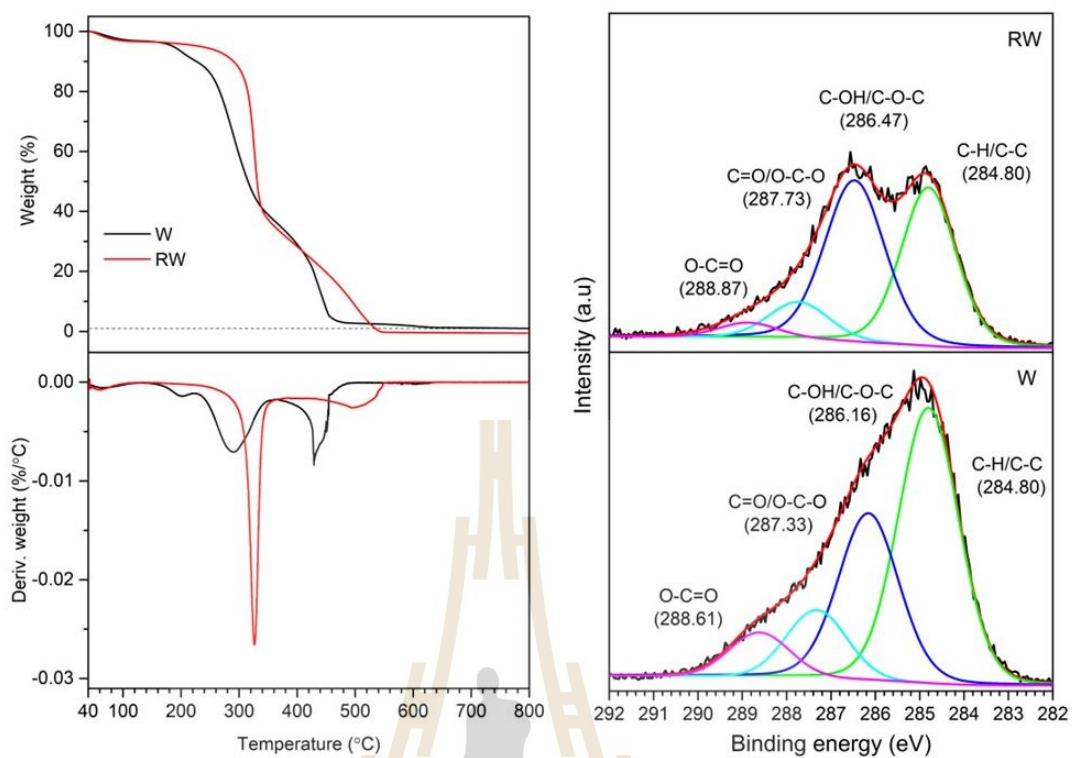
Figure A.1 TGA profile and C 1s spectra of W and RW.
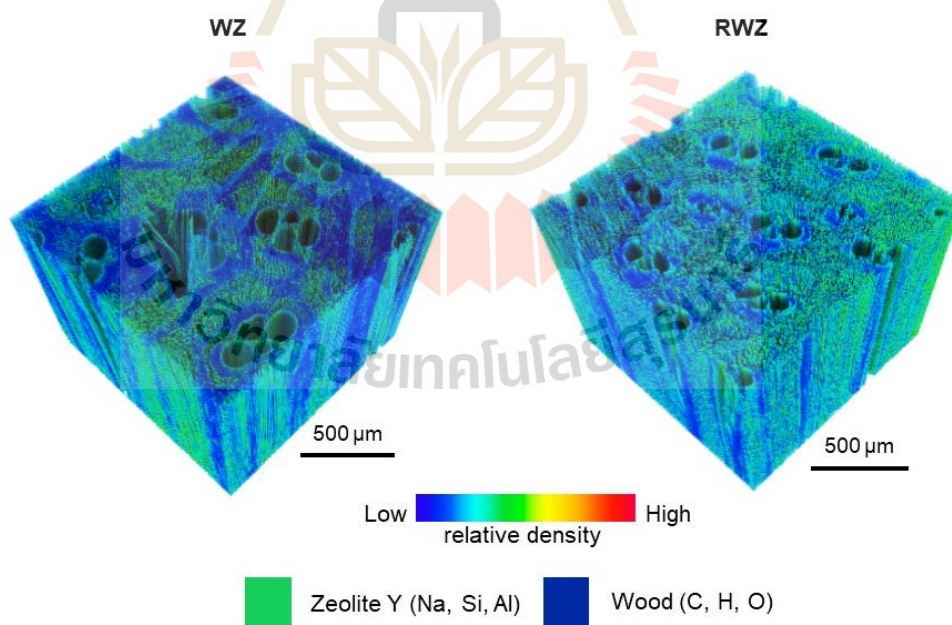
Figure A.2 3D X-ray tomography images of untreated wood-zeolite composite (WZ) and refluxed wood-zeolite composite (RWZ).
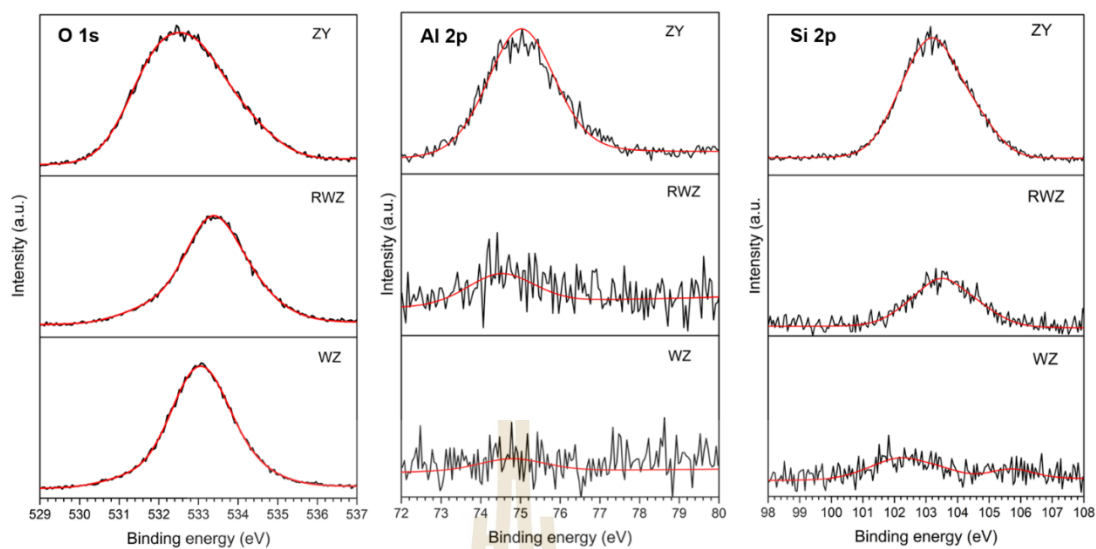
**Figure A.3** O1s, Al2p and Si2p spectra of WZ, RWZ, and ZY
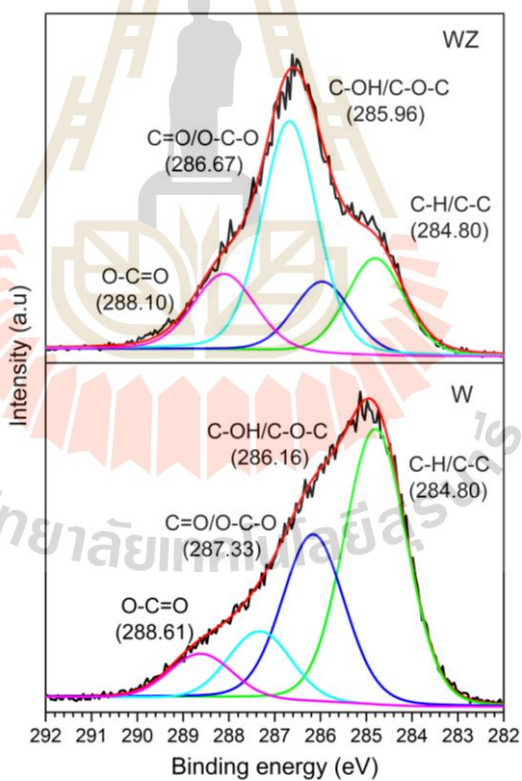
Figure A.4 XPS spectra of C1s of untreated wood (W) and wood-zeolite composite (WZ).

APPENDIX B

OPERANDO XAS STUDY OF ETHANOL-STEAM REFORMING ON COPPER-BASED ZEOLITE Y CATALYSTS: EFFECT OF ZEOLITE FORMS
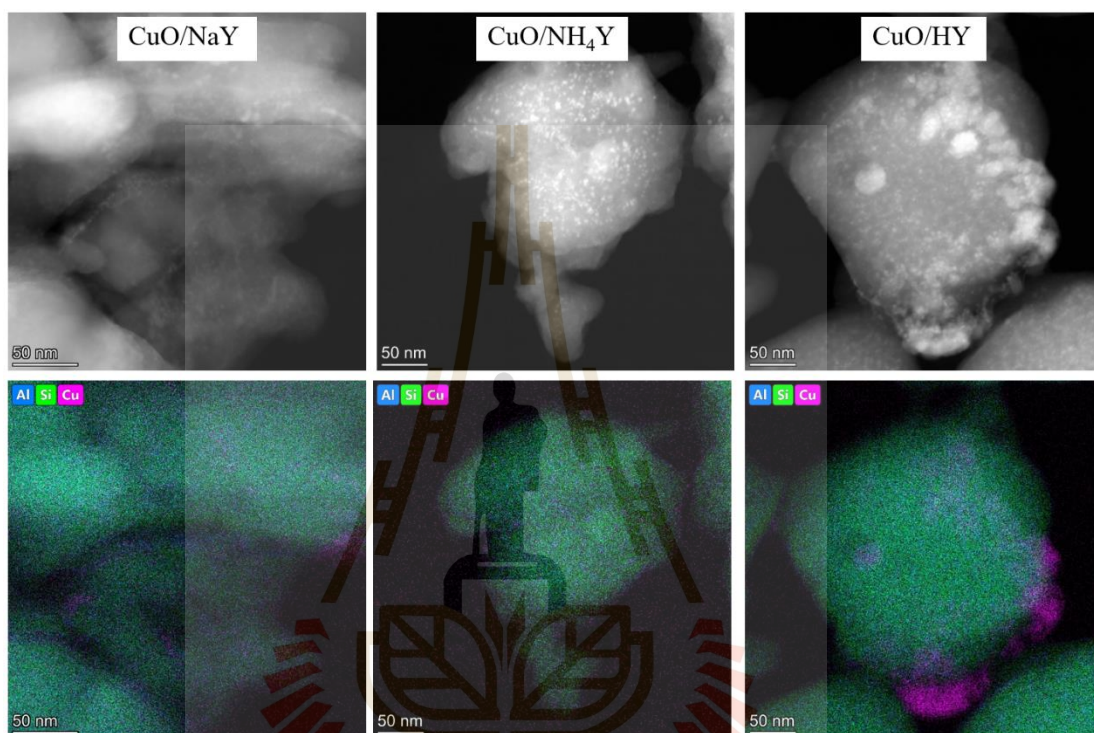

Figure B.1 TEM images and mappings of spent catalysts after ESR testing.

Table B.1 Percent of each element from ICP technique.

Samples	Si %wt.	Al %wt.	O %wt.	Na %wt.	Cu Theory	Cu %wt.	Si/Al
NaY	22.07	10.64	58.22	9.07	-	-	2.08
AY	25.10	11.54	58.84	4.53	-	-	2.17
HY	25.77	12.44	57.03	4.76	-	-	2.07
CuO/NaY	21.54	10.08	55.29	8.77	4	4.32	2.14
CuO/NH$_4$Y	23.48	10.24	57.91	3.91	4	4.46	2.29
CuO/HY	22.43	10.71	58.23	4.20	4	4.43	2..09

Table B.2 Vibration and peak assignments of functional groups of samples before and after calcination. (Ma et al., 2021; Mozgawa, 2001; Phung et al., 2014)

Peak assignments	Wavenumber (cm^{-1})
O-T-O bending vibration of S4R (T = Si or Al)	463
T-O-T bending vibrations of double rings (D6R)	573
Symmetric stretching of O-T-O	698-779
Asymmetric stretching of Si-O-T	1013-1089
Asymmetric stretching of Si-O-Si (shoulder)	1128

Table B.3 Catalytic activity of zeolite NaY and HY in ESR reaction.

Catalysts	EtOH Conversion (%)	H$_2$ productivity (mol·min^{-1}·kg^{-1})	Concentration of products (mol·mL^{-1})		
			C$_2$H$_4$ (mol/mL)	CH$_3$CHO (mol/mL)	CH$_4$ (mol/mL)
T= 300 °C					
NaY	4.51	0.16	0	0	0
HY	9.72	0.29	8.5E-04	0	0
T= 400 °C					
NaY	5.92	0.26	1.6E-04	0	0
HY	11.11	0.26	9.6E-04	0	0
T= 500 °C					
NaY	21.15	0.58	3.7E-04	1.2E-04	0
HY	29.17	0.63	1.2E-03	7.4E-05	0
T= 600 °C					
NaY	41.18	1.92	4.2E-04	3.8E-04	1.2E-06
HY	49.58	2.00	1.1E-03	3.5E-04	9.0E-07

Ethanol

$y = 137195x + 0.1419$
$R^2 = 0.9984$

H$_2$

$y = 1E\text{-}06x + 2E\text{-}10$
$R^2 = 0.9963$
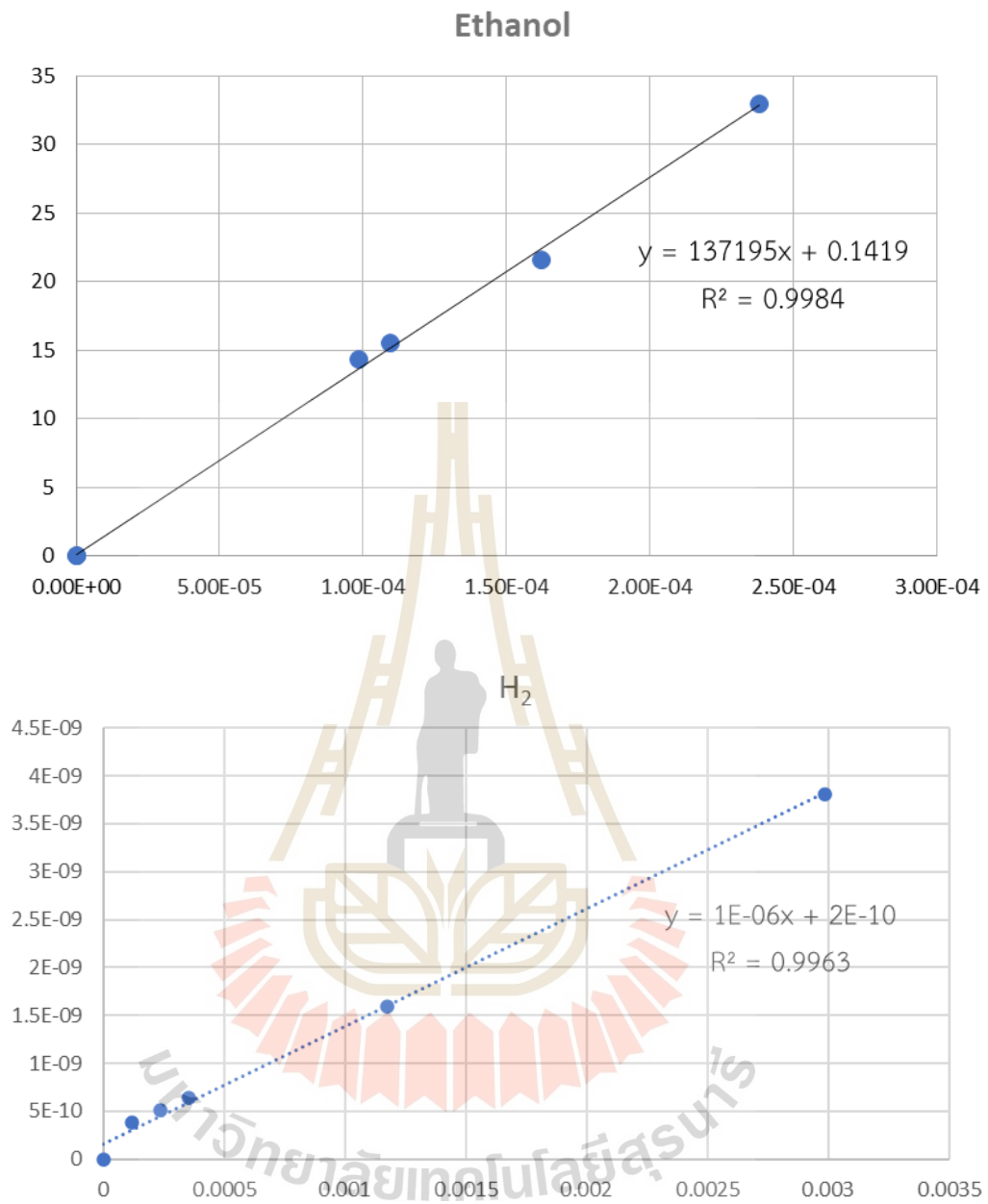
**Figure B.2** Calibration curve of Ethanol, H$_2$, C$_2$H$_4$, and CH$_4$.
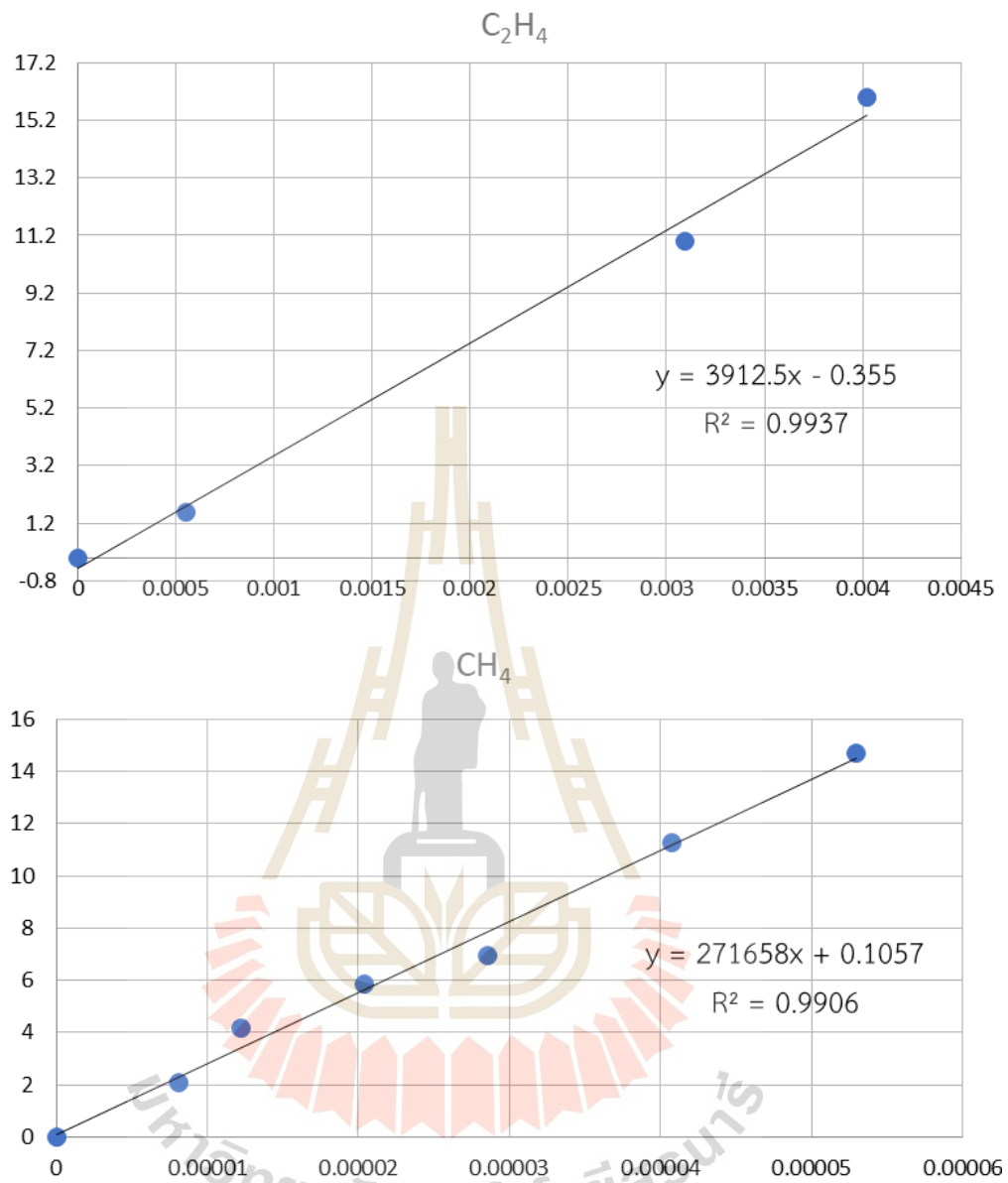
Figure B.2 (Continued) Calibration curve of Ethanol, H_2, C_2H_4, and CH_4.

References

Ma, Y.-K., Rigolet, S., Michelin, L., Paillaud, J.-L., Mintova, S., Khoerunnisa, F., Daou, T. J., and Ng, E.-P. (2021). Facile and fast determination of Si/Al ratio of zeolites using FTIR spectroscopy technique. *Microporous and Mesoporous Materials, 311*, 110683.

Mozgawa, W. (2001). The relation between structure and vibrational spectra of natural zeolites. *Journal of Molecular Structure, 596*(1), 129-137.

Phung, T. K., Carnasciali, M. M., Finocchio, E., and Busca, G. (2014). Catalytic conversion of ethyl acetate over faujasite zeolites. *Applied Catalysis A: General, 470*, 72-80.

CURRICULUM VITAE

PIMRAPUS TAWACHKULTANADIOK

Education

2018   B.Sc. in Chemistry (1st Class Honors), Khon Kaen University, Thailand

2018 – 2023 Ph.D. candidate in Chemistry, Suranaree University of Technology, Institute of Science, Thailand

Scholarship

2014 – 2022 Science Achievement Scholarship of Thailand (SAST)

Publications

1. Tawachkultanadilok, P., Osakoo, N., Keawkumay, C., Deekamwong, K., Sosa, N., Rojviriya, C., ... & Wittayakun, J. (2023). *Materials.* 16(14), 4946.

2. Osakoo, N., Tawachkultanadilok, P., Loiha, S., Roessner, F., Poo-arporn, Y., Kidkhunthod, P., ... & Wittayakun, J. (2022). *Appl. Catal. B: Environ.* 316, 121670.

3. Senamart, N., Loiha, S., Poo-arporn, Y., Tawachkultanadilok, P., Tonlublao, S., Limphirat, W., ... & Poo-arporn, R. P. (2021). *Radiat. Phys. Chem.* 185, 109492.